

Brijendra_thesis.pdf

 Delhi Technological University

Document Details

Submission ID

trn:oid:::27535:106576809

Submission Date

Jul 31, 2025, 2:43 PM GMT+5:30

Download Date

Jul 31, 2025, 2:50 PM GMT+5:30

File Name

Brijendra_thesis.pdf

File Size

35.3 MB

153 Pages

31,164 Words

173,110 Characters

8% Overall Similarity

The combined total of all matches, including overlapping sources, for each database.





Filtered from the Report

- Bibliography
- Small Matches (less than 10 words)




Exclusions

- 9 Excluded Sources
- 11 Excluded Matches

Match Groups

-  **139** Not Cited or Quoted 6%
Matches with neither in-text citation nor quotation marks
-  **37** Missing Quotations 2%
Matches that are still very similar to source material
-  **0** Missing Citation 0%
Matches that have quotation marks, but no in-text citation
-  **0** Cited and Quoted 0%
Matches with in-text citation present, but no quotation marks

Top Sources

- 3%  Internet sources
- 4%  Publications
- 5%  Submitted works (Student Papers)

Integrity Flags

0 Integrity Flags for Review

No suspicious text manipulations found.

Our system's algorithms look deeply at a document for any inconsistencies that would set it apart from a normal submission. If we notice something strange, we flag it for you to review.

A Flag is not necessarily an indicator of a problem. However, we'd recommend you focus your attention there for further review.

Match Groups

- 139** Not Cited or Quoted 6%
Matches with neither in-text citation nor quotation marks
- 37** Missing Quotations 2%
Matches that are still very similar to source material
- 0** Missing Citation 0%
Matches that have quotation marks, but no in-text citation
- 0** Cited and Quoted 0%
Matches with in-text citation present, but no quotation marks

Top Sources

- 3% Internet sources
- 4% Publications
- 5% Submitted works (Student Papers)

Top Sources

The sources with the highest number of matches within the submission. Overlapping sources will not be displayed.

- 1** Internet
komunikacie.uniza.sk <1%
- 2** Submitted works
King Fahd University for Petroleum and Minerals on 2015-03-11 <1%
- 3** Submitted works
Engineers Australia on 2018-05-16 <1%
- 4** Internet
pdfcoffee.com <1%
- 5** Publication
Shilpa Ranjan, Madhusudan Singh, Mini Sreejeth. "ANFIS-Based Resonant Control..." <1%
- 6** Submitted works
Savitribai Phule Pune University on 2015-10-26 <1%
- 7** Publication
Green Energy and Technology, 2015. <1%
- 8** Publication
"Smart Computing and Control Renewable Energy Systems", Springer Science an... <1%
- 9** Submitted works
University of Stellenbosch, South Africa on 2024-11-26 <1%
- 10** Internet
www.researchgate.net <1%

| | | | |
|----|-----------------|--|-----|
| 11 | Publication | Hai Jin. "Application of genetic algorithms in parameters identification of asynchr... | <1% |
| 12 | Publication | Kaushik Rajashekara. "Current and future trends in electrification of road and air ... | <1% |
| 13 | Internet | www.mdpi.com | <1% |
| 14 | Internet | researchspace.ukzn.ac.za | <1% |
| 15 | Submitted works | University of Malaya on 2013-05-16 | <1% |
| 16 | Submitted works | University of Sheffield on 2024-08-15 | <1% |
| 17 | Publication | Changwoo Lee, In Gwun Jang. "Topology Optimization of the IPMSMs Considering... | <1% |
| 18 | Publication | Firat Ekinci, Tugce Demirdelen, Mehmet Bilgili. "Modelling of wind turbine power ... | <1% |
| 19 | Publication | Jiong Li, Yao Sun, Hanbing Dan, Xing Li, Feng Zhou, Mei Su. "Adaptive Control for ... | <1% |
| 20 | Submitted works | University of Greenwich on 2024-12-16 | <1% |
| 21 | Submitted works | Anna University on 2025-07-04 | <1% |
| 22 | Publication | Wei Xu, Abdul Khaliq Junejo, Yi Liu, Md. Rabiul Islam. "Improved Continuous Fa... | <1% |
| 23 | Internet | www.conacyt.gov.py | <1% |
| 24 | Submitted works | Loughborough University on 2025-05-28 | <1% |

| | | | |
|----|-----------------|--|-----|
| 25 | Submitted works | Michigan Technological University on 2021-11-08 | <1% |
| 26 | Submitted works | Oxford Brookes University on 2025-03-29 | <1% |
| 27 | Internet | isda2001.softcomputing.net | <1% |
| 28 | Internet | macsphere.mcmaster.ca | <1% |
| 29 | Internet | www.peeref.com | <1% |
| 30 | Publication | Bharat Singh, Ankur Chowdhury, Vishal Mishra, Ankur Jain. "Chapter 56 Investiga... | <1% |
| 31 | Publication | Hu, Dakai. "Improvement of torque and speed control of permanent magnet sync... | <1% |
| 32 | Submitted works | University of Sheffield on 2021-11-08 | <1% |
| 33 | Publication | "Computational Intelligence in Engineering Science", Springer Science and Busin... | <1% |
| 34 | Submitted works | University of Sheffield on 2023-01-15 | <1% |
| 35 | Submitted works | Grimsby College, South Humberside on 2025-05-08 | <1% |
| 36 | Submitted works | Malta College of Arts,Science and Technology on 2025-05-24 | <1% |
| 37 | Submitted works | University Tun Hussein Onn Malaysia on 2023-01-26 | <1% |
| 38 | Submitted works | Education Partnership North East (Sunderland College) on 2025-02-20 | <1% |

| | | | |
|----|-----------------|--|-----|
| 39 | Submitted works | IIT Delhi on 2016-01-15 | <1% |
| 40 | Publication | Komma Lavanya, Alice Mary Karlapudy, Saraswathi Garimella. "Design Optimizati... | <1% |
| 41 | Submitted works | Saint Vincent College on 2009-12-07 | <1% |
| 42 | Submitted works | Cranfield University on 2021-06-04 | <1% |
| 43 | Submitted works | Kwame Nkrumah University of Science and Technology on 2025-01-14 | <1% |
| 44 | Submitted works | University of Edinburgh on 2012-08-22 | <1% |
| 45 | Publication | Yu Wang, Ting Li, Jingtao Zhang, Peng Xiao. "Sliding Mode and Deadbeat Predictiv... | <1% |
| 46 | Internet | www.afstrinity.com | <1% |
| 47 | Submitted works | King's College on 2025-04-10 | <1% |
| 48 | Submitted works | Rajiv Gandhi Institute of Technology, Kottayam on 2025-05-16 | <1% |
| 49 | Publication | Sixun Du, Liwei Chen, Yuanlin Wang, Manfeng Dou. "The Influence of Weighing F... | <1% |
| 50 | Submitted works | University of Kansas on 2007-04-06 | <1% |
| 51 | Submitted works | University of Technology, Sydney on 2023-05-25 | <1% |
| 52 | Publication | A.L. Rodriguez, D.J. Gomez, I. Villar, A. Lopez-de-Heredia, I. Etxeberria-Otadui. "Im... | <1% |

| | | | |
|----|-----------------|---|-----|
| 53 | Publication | Ashu Sharm, Poornima Suryanath Singh, Divya Lakshmi, Neha Arora, Rupesh Ma... | <1% |
| 54 | Submitted works | Khalifa University of Science Technology and Research on 2024-11-27 | <1% |
| 55 | Publication | Yingying Xu, Yiguang Chen, Zhihua Fu, Mingxia Xu, Haiyu Liu, Li Cheng. "Design a... | <1% |
| 56 | Internet | saarj.com | <1% |
| 57 | Submitted works | Glyndwr University on 2024-07-29 | <1% |
| 58 | Publication | Guohai Liu, Lingling Chen, Wenxiang Zhao, Yan Jiang, Li Qu. "Internal Model Cont... | <1% |
| 59 | Submitted works | Gyeongsang National University on 2020-12-03 | <1% |
| 60 | Submitted works | IUBH - Internationale Hochschule Bad Honnef-Bonn on 2024-03-19 | <1% |
| 61 | Publication | Khan, M. Abdes, M. Nasir Uddin, and M. Azizur Rahman. "A Novel Wavelet-Neura... | <1% |
| 62 | Submitted works | NIT Imphal on 2025-07-22 | <1% |
| 63 | Submitted works | Nazarbayev University on 2024-11-18 | <1% |
| 64 | Submitted works | Politecnico di Milano on 2017-03-27 | <1% |
| 65 | Submitted works | University of Liverpool on 2024-05-16 | <1% |
| 66 | Internet | ejournal.csol.or.id | <1% |

| | | | |
|----|-----------------|--|-----|
| 67 | Submitted works | iGroup on 2014-06-19 | <1% |
| 68 | Internet | ir.library.dc-uoit.ca | <1% |
| 69 | Internet | itegam-jetia.org | <1% |
| 70 | Internet | pastel.archives-ouvertes.fr | <1% |
| 71 | Internet | pure.tue.nl | <1% |
| 72 | Internet | repositorium.uminho.pt | <1% |
| 73 | Internet | utd-ir.tdl.org | <1% |
| 74 | Internet | www.trademarkelite.com | <1% |
| 75 | Publication | Aissam Riad Meddour, Nassim Rizoug, Patrick Leserf, Christopher Vagg, Richard ... | <1% |
| 76 | Publication | Alwadie, Hatim. "High-Performance Machine Design for Propulsion and On-Board... | <1% |
| 77 | Publication | Berker Bilgin, James Weisheng Jiang, Ali Emadi. "Switched Reluctance Motor Driv... | <1% |
| 78 | Submitted works | Brunel University on 2017-06-14 | <1% |
| 79 | Submitted works | College of the North Atlantic-Qatar on 2024-11-19 | <1% |
| 80 | Publication | Edi Sankararao, Raja Gandhi, Abanishwar Chakraborti, Rakesh Roy. "Comparative... | <1% |

| | | | |
|----|-----------------|---|-----|
| 81 | Publication | Farah, Nabil Salem Yahya. "Robust Predictive Control of Permanent Magnet Sync... | <1% |
| 82 | Publication | Fujiong Zhao, Yunxia Xie, Jianfeng Mao, Yingjie Xu, Gaosheng Li, Rongsheng Jia, ... | <1% |
| 83 | Submitted works | Glasgow Caledonian University on 2021-12-19 | <1% |
| 84 | Publication | Hadef, M., A. Djerdir, M. R. Mekideche, and A-O. N'Diaye. "Diagnosis of stator win... | <1% |
| 85 | Submitted works | Indian Institute of Technology, Kharagpure on 2015-08-10 | <1% |
| 86 | Publication | Jayakody Shreen, Kyung-min Lee. "Improving the Regenerative Efficiency of the A... | <1% |
| 87 | Publication | Liyun Feng, Xiaodong Sun, Xiang Tian, Kaikai Diao. "Direct Torque Control With V... | <1% |
| 88 | Publication | Mitja Breznik, Vanja Ambrožič, Mitja Nemec. "Detection of open circuit fault in ba... | <1% |
| 89 | Submitted works | National Institute of Technology, Patna on 2024-09-03 | <1% |
| 90 | Submitted works | Polytechnic of Turin on 2021-01-25 | <1% |
| 91 | Submitted works | Rajiv Gandhi Institute of Technology, Kottayam on 2025-05-16 | <1% |
| 92 | Submitted works | Sonora High School on 2003-05-27 | <1% |
| 93 | Submitted works | Universiti Teknikal Malaysia Melaka on 2013-05-29 | <1% |
| 94 | Submitted works | University of Nottingham on 2022-09-05 | <1% |

| | | | |
|-----|-----------------|--|-----|
| 95 | Submitted works | University of Wollongong on 2019-11-02 | <1% |
| 96 | Internet | centaur.reading.ac.uk | <1% |
| 97 | Internet | ebin.pub | <1% |
| 98 | Internet | hrcak.srce.hr | <1% |
| 99 | Internet | iris.uniroma3.it | <1% |
| 100 | Internet | livrepository.liverpool.ac.uk | <1% |
| 101 | Internet | ntnuopen.ntnu.no | <1% |
| 102 | Internet | pmarketresearch.com | <1% |
| 103 | Internet | prism.ucalgary.ca | <1% |
| 104 | Internet | publication-theses.unistra.fr | <1% |
| 105 | Internet | theses.gla.ac.uk | <1% |
| 106 | Internet | www.frontiersin.org | <1% |
| 107 | Publication | Ahmed, Abdallah. "Experimental and Numerical Heat Transfer Investigation of Re... | <1% |
| 108 | Publication | Bruno Dalla Chiara, Francesco Deflorio, Marco Eid. "Analysis of real driving data t... | <1% |

| | | | |
|-----|-----------------|---|-----|
| 109 | Submitted works | Budapest University of Technology and Economics on 2020-08-09 | <1% |
| 110 | Submitted works | Central University of Haryana on 2025-07-20 | <1% |
| 111 | Publication | Chao Wang, Ziqiang Zhu, Lei Xu, Ximeng Wu, Kejin Lu. "Optimized Feedback Type ... | <1% |
| 112 | Submitted works | Columbia Basin College on 2024-02-27 | <1% |
| 113 | Submitted works | Concordia University on 2025-05-30 | <1% |
| 114 | Publication | Hanuman Prasad, Tanmoy Maity. "FPGA-based design and implementation of DT... | <1% |
| 115 | Submitted works | Indian Institute of Technology Jodhpur on 2020-08-25 | <1% |
| 116 | Submitted works | Jawaharlal Nehru Technological University on 2024-09-13 | <1% |
| 117 | Publication | Jiajun Wu, Hui Liu, Xiaolei Ren, Shida Nie, Yechen Qin, Lijin Han. "A multi-objectiv... | <1% |
| 118 | Submitted works | Loughborough College on 2025-03-07 | <1% |
| 119 | Publication | Lourembam Ranjita Devi, Sreenu Sreekumar, Rohit Bhakar, Dileep G., Sanjeeviku... | <1% |
| 120 | Publication | Mohammed Qasim, Vinod Khadkikar. "Application of Artificial Neural Networks f... | <1% |
| 121 | Publication | Noemi Hernandez-Oliva, Maria Barbara Calva-Yanez, Gabriel Sepulveda-Cervante... | <1% |
| 122 | Submitted works | Savitribai Phule Pune University on 2015-07-24 | <1% |

| | | | |
|-----|-----------------|--|-----|
| 123 | Submitted works | The University of Manchester on 2025-04-11 | <1% |
| 124 | Publication | Tolcha Lemma Sime, Prashant Aluvada, Solomon Habtamu, Zewde Tolosa. "Model... | <1% |
| 125 | Submitted works | University of Newcastle upon Tyne on 2024-08-23 | <1% |
| 126 | Submitted works | University of Northumbria at Newcastle on 2012-03-26 | <1% |
| 127 | Submitted works | University of Sheffield on 2020-07-02 | <1% |
| 128 | Submitted works | University of Stellenbosch, South Africa on 2024-11-22 | <1% |
| 129 | Submitted works | University of Sydney on 2016-08-31 | <1% |
| 130 | Submitted works | University of Technology on 2021-06-29 | <1% |
| 131 | Submitted works | Victoria University on 2015-07-30 | <1% |
| 132 | Publication | Wei Xu, Moustafa Magdi Ismail, Md. Rabiul Islam. "Permanent Magnet Synchrono... | <1% |
| 133 | Publication | Wusen Wang, Chunhua Liu, Senyi Liu, Hang Zhao. "Model Predictive Torque Contr... | <1% |
| 134 | Internet | dspace.rpi.edu | <1% |
| 135 | Internet | fastercapital.com | <1% |
| 136 | Submitted works | iGroup on 2014-07-16 | <1% |

| | | | |
|-----|-----------------|-------------------------------------|-----|
| 137 | Internet | mafiadoc.com | <1% |
| 138 | Internet | mediatum.ub.tum.de | <1% |
| 139 | Internet | nottingham-repository.worktribe.com | <1% |
| 140 | Internet | patents.justia.com | <1% |
| 141 | Internet | scholar.uwindsor.ca | <1% |
| 142 | Submitted works | unifei on 2025-07-29 | <1% |
| 143 | Internet | www.davidson.com.au | <1% |
| 144 | Internet | www.hindawi.com | <1% |
| 145 | Internet | www.techscience.com | <1% |

PERFORMANCE ENHANCEMENT OF PERMANENT MAGNET SYNCHRONOUS MOTOR (PMSM) FOR ELECTRIC VEHICLE APPLICATIONS

**A thesis submitted
In Partial Fulfillment of the Requirements
for the Degree of**

DOCTOR OF PHILOSOPHY
by

BRIJENDRA SANGAR

(Roll No. 2K21/PHDEE/30)

**Under the Supervision of
Prof. Madhusudan Singh and Prof. Mini Sreejeth
Department of Electrical Engineering
Delhi Technological University, Delhi - 110042**



**Department of Electrical Engineering
DELHI TECHNOLOGICAL UNIVERSITY
(Formerly Delhi College of Engineering)
Shahbad Daultpur, Main Bawana Road, Delhi - 110042. INDIA**

July, 2025

**©DELHI TECHNOLOGICAL UNIVERISITY, DELHI-2025
ALL RIGHTS RESERVED**



DELHI TECHNOLOGICAL UNIVERSITY
(Formerly Delhi College of Engineering)
Shahbad Daulatpur, Main Bawana Road, Delhi-42

CANDIDATE'S DECLARATION

I hereby certify that the work which is being presented in the thesis entitled **PERFORMANCE ENHANCEMENT OF PERMANENT MAGNET SYNCHRONOUS MOTOR (PMSM) FOR ELECTRIC VEHICLE APPLICATIONS** in partial fulfillment of the requirements for the award of the Degree of Doctor of Philosophy and submitted in the **Department of Electrical Engineering** of the **Delhi Technological University** is an authentic record of my own work carried out during the period from August, 2021 to July, 2025 under the supervision of Prof. **Madhusudan Singh**, Electrical Engineering, Delhi Technological University and Prof. **Mini Sreejeth**, Professor, **Department of Electrical Engineering, Delhi Technological University**.

The matter presented in this thesis has not been submitted by me for the award of any other degree of this or any other Institute.

(Brijendra Sangar)

This is to certify that the student has incorporated at the corrections suggested by the examiners in the thesis and the statement made by the candidate is correct to the best of our knowledge.

Signature of Supervisors

Signature of External Examiner



DELHI TECHNOLOGICAL UNIVERSITY

(Formerly Delhi College of Engineering)
Shahbad Daulatpur, Main Bawana Road, Delhi-42

CERTIFICATE

Certify that **Brijendra Sangar** (2K21/PHDEE/30) has carried out their work presented in this thesis entitled "**PERFORMANCE ENHANCEMENT OF PERMANENT MAGNET SYNCHRONOUS MOTOR (PMSM) FOR ELECTRIC VEHICLE APPLICATIONS**" for the award of **Doctor of Philosophy** from **Department of Electrical Engineering, Delhi Technological University**, Delhi, under our supervision. The thesis embodies results of original work, and studies are carried out by the student himself and the content of the thesis do not form the basis for the award of any other degree to the candidate or to anybody else from this or any other University/Institute.

(**Madhusudan Singh**)
Supervisor

(**Mini Sreejeth**)
Co-Supervisor

Date:

Abstract

The electrification of transportation is accelerating globally as a response to fossil fuel depletion and environmental degradation. At the core of modern electric vehicles (EVs), Permanent Magnet Synchronous Motors (PMSMs) offer high torque density, superior efficiency, and compactness. Despite these advantages, their nonlinear dynamics, sensitivity to parameter variations, and susceptibility to torque and current ripple pose serious challenges under dynamic EV driving conditions. This thesis presents a detailed investigation into intelligent current control strategies aimed at enhancing the performance and robustness of PMSM drives for EV propulsion.

Three advanced control strategies are developed and validated: Adaptive Neuro-Fuzzy Inference System-based Hysteresis Current Control (ANFIS-HCC), Adaptive Neuro-Fuzzy Model Predictive Current Control (ANFIS-MPCC), and Adaptive Neuro-Fuzzy Sliding Mode Current Control (ANFIS-SMCC). These hybrid frameworks integrate the adaptive learning capabilities of ANFIS with classical control structures to achieve real-time performance improvements in ripple suppression, current tracking, and energy efficiency.

The ANFIS-HCC controller adaptively adjusts the hysteresis band based on motor speed and current error using a fuzzy rule base, leading to improved switching decisions and minimized torque ripple. Experimental results on a 3 kW PMSM prototype show that ANFIS-HCC reduces torque ripple from 1.8 Nm (conventional HCC) to 1.0 Nm and current ripple from 1.1 A to 0.7 A, with a 12 % improvement in energy efficiency under urban and highway drive cycles.

ANFIS-MPCC combines the model-based prediction of current trajectories with ANFIS-tuned weighting factors for the cost function. It enhances steady-state performance and switching efficiency, especially during high-speed operations. Simulation and hardware-in-loop results reveal that torque ripple is reduced to 0.68 Nm and current ripple to 0.5 A, achieving 25–30% better dynamic

vi

response than classical MPC while reducing computation time through precomputed ANFIS lookup tables.

The ANFIS-SMCC strategy merges the robustness of sliding mode control with adaptive neuro-fuzzy tuning of switching gains. It incorporates a saturation-based switching law to mitigate chattering while ensuring finite-time convergence of current tracking errors. Experimental validation on the same PMSM platform under load steps and temperature variations demonstrates torque ripple suppression to 0.5Nm and current ripple below 0.5 A, outperforming both ANFIS-HCC and ANFIS-MPCC. Under sensor noise ($\sigma = 0.05$), temperature drift ($+30\% R_s$), and inverter nonlinearities, ANFIS-SMCC showed only 10–15% performance degradation, compared to 30–70% for other methods.

All proposed controllers were implemented on a dSPACE DS1104 real-time hardware platform, interfaced with a laboratory-grade PMSM, Voltage Source Inverter, and high-precision sensors. Real-time execution met the $5\mu\text{s}$ sampling constraint, with ANFIS-SMCC operating within $120\mu\text{s}$ per cycle. Comprehensive testing using IM240 and Modified Indian Drive Cycles(MIDC) revealed that ANFIS-SMCC provided the best trade-off between ripple suppression, computational efficiency, and robustness, while ANFIS-MPCC delivered superior predictive accuracy, and ANFIS-HCC offered simplicity and rapid convergence.

In conclusion, this thesis presents a unified framework of intelligent PMSM current controllers tailored for electric vehicle propulsion, with thorough validation through simulation and real-time experimentation. The proposed ANFIS-based hybrid strategies yield substantial improvements in torque smoothness, thermal stability, control precision, and overall motor efficiency, contributing to the performance, reliability, and energy economy of EVs.

Acknowledgements

It is with profound appreciation that I acknowledge my advisors, Professor Madhusudan Singh and Professor Mini Sreejeth of the Department of Electrical Engineering, Delhi Technological University. Their expert mentorship and steadfast support were instrumental throughout the course of my doctoral research. I count myself exceptionally fortunate to have had the honor of working under their distinguished supervision.

I owe a special debt of gratitude to the members of my PhD research committee for their scholarly contributions. The insightful feedback from Professor Vivek Shrivastava (Department of Electrical Engineering, National Institute of Technology Uttarakhand) and Professor Jitendra Nath Rai, (Department of Electrical Engineering, Delhi Technological University) was crucial in refining this dissertation.

I extend my deepest gratitude to my family. Their enduring love, patience, and unwavering belief in me were a constant source of motivation. Whatever I have accomplished is a direct reflection of their unconditional support. To my friends, both within and outside the DTU Delhi community, I offer my sincere thanks. Their companionship, valuable input, and constant encouragement were essential in making this journey not only possible but also enjoyable.

Above all, I am grateful to God Almighty, for His grace provided the fortitude required at every stage of this endeavor

Date:

Brijendra Sangar

Contents

| | |
|--|-----------|
| Abstract | v |
| Acknowledgements | vii |
| Contents | viii |
| List of Figures | xiii |
| List of Tables | xvii |
| 1 Introduction | 1 |
| 1.1 Background and Motivation | 1 |
| 1.1.1 Overview of Electric Vehicles (EVs) | 2 |
| 1.1.2 Role of PMSM in EVs | 3 |
| 1.1.3 Challenges in PMSM Application for Electric Vehicles | 4 |
| 1.2 Research Objectives | 6 |
| 1.3 Organization of Thesis | 7 |
| 1.4 Conclusion | 9 |
| 2 Literature survey | 11 |
| 2.1 Overview of EVs and their growing importance. | 11 |
| 2.2 Architecture and Advanced Control of PMSM Drives for EV Applications | 13 |
| 2.2.1 Construction, Types, and Operating Modes of PMSM | 13 |
| 2.2.2 PMSM Control strategies | 16 |
| 2.2.3 Integration and Role of PMSM in EV | 18 |
| 2.2.4 Performance Enhancement through Advanced Algorithms | 20 |
| 2.3 Technical and economic challenges. | 22 |
| 2.4 Identified gaps in current research. | 24 |
| 2.5 Conclusion | 26 |
| 3 Modeling and Simulation of PMSM Drive for EV application | 27 |

x

| | | |
|----------|--|-----------|
| 3.1 | Introduction | 27 |
| 3.2 | Mathematical Modeling of EV | 27 |
| 3.3 | Mathematical Modeling of PMSMs | 30 |
| 3.3.1 | PMSM Modeling in the Stationary a-b-c Frame | 31 |
| 3.3.2 | PMSM Modeling in the d-q Rotating Frame | 35 |
| 3.3.3 | PMSM Equivalent Circuit | 37 |
| 3.4 | Field-Oriented Control (FOC) for PMSM Speed Regulation | 37 |
| 3.5 | Modeling of PMSM-drive for EV applications | 39 |
| 3.5.1 | Battery Model | 40 |
| 3.5.2 | Transmission Model | 41 |
| 3.5.3 | Simulation Results under IM240 Drive Cycle | 42 |
| 3.5.4 | Significance for EV Drivetrain Design | 43 |
| 3.6 | Conclusion | 44 |
| 4 | Design and Development of PMSM Drive Train | 45 |
| 4.1 | Introduction | 45 |
| 4.2 | PMSM Drive System Overview | 45 |
| 4.2.1 | Motor Specifications | 47 |
| 4.2.2 | Loading System | 47 |
| 4.3 | Controller Design | 47 |
| 4.3.1 | Hardware Configuration | 47 |
| 4.3.2 | Software Integration | 49 |
| 4.3.3 | System Integration | 50 |
| 4.4 | Power Supply and Inverter System | 50 |
| 4.4.1 | Bidirectional Power Supply | 51 |
| 4.4.2 | Inverter and Driver Circuit | 51 |
| | IGBT Switch Ratings | 52 |
| | Gate Driver Circuit | 53 |
| 4.5 | Measurement System | 53 |
| 4.5.1 | Voltage Measurement | 54 |
| 4.5.2 | Current Measurement | 55 |
| 4.5.3 | Torque Measurement | 55 |
| 4.5.4 | Speed and Position Measurement | 57 |
| 4.6 | Conclusion | 59 |

| | | |
|----------|---|-----------|
| 5 | Enhancing PMSM Drive Performance for Electric Vehicles through ANFIS-HCC Integration | 61 |
| 5.1 | Introduction | 61 |
| 5.2 | Design of ANFIS-HCC Control Strategy for PMSM Drives | 62 |
| 5.2.1 | Overview of Adaptive Neuro-Fuzzy Inference(ANFIS) System | 62 |
| 5.2.2 | Training and Structure Identification of ANFIS | 64 |
| 5.2.3 | Hysteresis Current Controller | 66 |
| 5.2.4 | Proposed ANFIS-HCC PMSM Drive | 67 |
| 5.3 | Simulation studies and Discussion | 68 |
| 5.4 | Experimental Validation and Comparison of proposed ANFIS-HCC with PI-HCC | 70 |
| 5.4.1 | Starting Performance of PMSM drive | 70 |
| 5.4.2 | Steady-state performance of PMSM drive | 70 |
| 5.4.3 | Dynamic Response of PMSM drive under variable conditions | 73 |
| 5.4.4 | Performance Validation using IM240 Drive Cycle | 75 |
| 5.5 | Conclusion | 79 |
| 6 | Ripple and Current Minimization in PMSM Drives Using ANFIS-MPCC for EV Applications | 81 |
| 6.1 | Introduction | 81 |
| 6.2 | Adaptive Neuro-Fuzzy Inference System (ANFIS) | 82 |
| 6.3 | Model Predictive Current Control | 83 |
| 6.4 | Proposed ANFIS-MPCC PMSM Drive | 84 |
| 6.5 | Simulaton Results and Discussion | 86 |
| 6.6 | Experimental Results and Analysis | 88 |
| 6.6.1 | Dynamic performance of PMSM drive | 89 |
| 6.6.2 | Performance validation using vehicular condition | 92 |
| 6.7 | Conclusion | 95 |
| 7 | Intelligent control of PMSM Drive using ANFIS-SMCC for EVs | 97 |
| 7.1 | Introduction | 97 |
| 7.2 | Adaptive Neuro-Fuzzy Inference System (ANFIS) | 98 |
| 7.3 | Sliding Mode Current Control (SMCC) | 98 |

xii

| | | |
|----------|--|------------|
| 7.4 | Integration of ANFIS-SMCC for Torque and Current Ripple Minimization | 100 |
| 7.4.1 | ANFIS Integration for Adaptive Tuning | 102 |
| 7.4.2 | Chattering Mitigation Strategies | 103 |
| 7.4.3 | Computational Complexity | 104 |
| 7.5 | Validation of ANFIS-SMCC for EV Propulsion | 106 |
| 7.5.1 | Simulaton Results and Discussion | 107 |
| 7.5.2 | Experimental Results and Discussion | 110 |
| 7.5.3 | Analysis of Practical Constraints | 112 |
| 7.6 | Conclusion | 114 |
| 8 | Conclusion and Future Scope of work | 115 |
| 8.1 | Conclusion | 115 |
| 8.2 | Suggestions for Future Work | 117 |
| | List of Publications | 119 |
| | Bibliography | 121 |

List of Figures

| | | |
|------|---|----|
| 2.1 | Components of an EV drivetrain | 12 |
| 2.2 | Structure of PMSM | 13 |
| 2.3 | Rotor configuration of PMSM (a)SPMSM (b) IPMSM | 16 |
| 2.4 | Classification of variable frequency drives | 17 |
| 3.1 | Forces acting on the vehicle | 29 |
| 3.2 | Motor Gear arrangement | 30 |
| 3.3 | Two-Pole PMSM Diagram | 35 |
| 3.4 | PMSM Equivalent Circuit | 37 |
| 3.5 | FOC of PMSM Drive System with HCC | 38 |
| 3.6 | Simulink model of PMSM-based EV drivetrain | 39 |
| 3.7 | Inspection and Maintenance (IM240) driving cycle | 42 |
| 3.8 | Simulation results of a PMSM-based EV drivetrain under IM 240 drive cycle, illustrating Motor power, Battery power, Battery current and state of charge(SoC) | 43 |
| 3.9 | Simulation results of a PMSM-based EV drivetrain under IM 240 drive cycle, illustrating Wheel speed, Wheel torque, Motor speed and Motor torque | 43 |
| 3.10 | Simulation results of a PMSM-based EV drivetrain under IM 240 drive cycle, illustrating Acceleration force, Aerodynamic force, Rolling resistance force, and Gradient force | 44 |
| 4.1 | Schematic Layout of the PMSM Drive System | 46 |
| 4.2 | Laboratory Prototype of the PMSM Drive System | 46 |
| 4.3 | Magnetic Powder Brake | 48 |
| 4.4 | dSPACE DS1104 Controller Setup | 48 |
| 4.5 | Software Integration Workflow for dSPACE DS1104 | 50 |
| 4.6 | Bidirectional DC Power Supply | 51 |

xiv

| | | |
|------|--|----|
| 4.7 | Insulated Gate Bipolar Transistor (IGBT) Module | 53 |
| 4.8 | Gate Driver Circuit | 54 |
| 4.9 | Voltage Sensor Circuit | 54 |
| 4.10 | Current Sensor Circuit | 55 |
| 4.11 | Torque Transducer | 55 |
| 4.12 | Rotary Encoder | 56 |
| 4.13 | Construction Principle of Incremental Encoder | 56 |
| 4.14 | Output Pulses of Incremental Encoder | 57 |
| 4.15 | Decoder Section of Incremental Encoder | 58 |
| 4.16 | Simulation Result of Incremental Encoder Output Pulses | 59 |
| 4.17 | Experimental Result of Incremental Encoder Output Pulses | 59 |
| 5.1 | Block Diagram of ANFIS | 62 |
| 5.2 | Flowchart for Training of proposed ANFIS-HCC | 65 |
| 5.3 | ANFIS-HCC Control Strategy for PMSM Drives | 67 |
| 5.4 | Dynamic Response of PMSM Drive under no-load rated speed (3000 rpm) Operation(a)PI-HCC b)ANFIS-HCC | 69 |
| 5.5 | Starting response of the PI-HCC and ANFIS-HCC based PMSM Drive under no-load-rated speed (3000 rpm) Operation | 70 |
| 5.6 | Dynamic response of laboratory prototype at start-up under rated speed and no-load operation: (a) PI-HCC-based FOC, (b) ANFIS-HCC-based FOC | 71 |
| 5.7 | Steady-state PMSM responses under PI-HCC (a–c) and ANFIS-HCC (d–f) at 750 rpm/3 Nm, 1500 rpm/6 Nm, and 2250 rpm/9 Nm, respectively. | 72 |
| 5.8 | PMSM responses under PI-HCC (a–c) and ANFIS-HCC (d–f) based FOC schemes: (a,d) Step speed change (750 → 1500 → 2250 rpm) @ 5 Nm; (b,e) Speed reversal (+1500 → –1500 rpm) @ no load; (c,f) Step load change (0 → 9 Nm) @ 2250 rpm. | 74 |
| 5.9 | Phase current harmonic analysis at 3000rpm at 8Nm load. (a)PI-HCC(b)ANFIS-HCC | 76 |
| 5.10 | Speed Response of the Laboratory Prototype for IM240 Drive Cycle. | 77 |
| 5.11 | Torque Response of the Laboratory Prototype for IM240 Drive Cycle | 77 |

| | |
|--|-----|
| 5.12 Power Response of the Laboratory Prototype for IM240 Drive Cycle Power. | 78 |
| 5.13 Energy consumption curve of the Laboratory Prototype for IM240 Drive Cycle Energy | 78 |
| 6.1 Proposed ANFIS-MPCC PMSM drive's Block Diagram | 84 |
| 6.2 Dynamic response while Speed change from 2250 to 500rpm at 8Nm load | 87 |
| 6.3 Dynamic response while load change from 8Nm to 2Nm at 2250rpm | 87 |
| 6.4 Laboratory Prototype for testing the ANFIS-MPCC based PMSM drive | 88 |
| 6.5 Dynamic response for step speed change from 2250 to 500rpm at 8Nm load | 89 |
| 6.6 Dynamic response for step load change from 8Nm to 2Nm at 2250rpm | 90 |
| 6.7 Comparative Analysis of Normalised Torque Ripple | 91 |
| 6.8 Comparative Analysis of Normalised Current Ripple | 91 |
| 6.9 Phase current harmonic analysis at 2250rpm at 8Nm load. (a)PI-HCC(b)ANFIS-HCC(c)PI-MPCC(d)ANFIS-MPCC | 93 |
| 6.10 Dynamic Response of MIDC Drive Cycle | 94 |
| 6.11 Comparative Analysis of energy consumption for MIDC Cycle | 94 |
| 7.1 ANFIS-SMCC Control Architecture | 101 |
| 7.2 Performance comparison under constant speed (3000 rpm) with torque variation (2–6 Nm) for ANFIS-HCC, ANFIS-MPCC, and ANFIS-SMCC: (a) Speed curves with speed ripple (SR); (b) Torque curves with torque ripple (TR); (c) Phase currents with current ripple (CR); (d) Stator flux current. | 108 |
| 7.3 Performance Comparison under constant load of 5Nm and Speed variation from 500 to 3000 to -500 rpm of ANFIS-HCC, ANFIS-MPCC, and ANFIS-SMCC: (a) Speed curves with Speed Ripples(SR) metrics, (b) Torque curves with Torque Ripples (TR) metrics, (c) Phase currents with Current Ripples (CR) metrics, and (d) Stator flux currents | 109 |

xvi

- 7.4 Experimental response under Constant speed 2800 rpm, while torque steps from 2 Nm to 6 Nm. 110
- 7.5 Experimental response under Constant Torque 5Nm , while speed steps from 500 rpm to 2800 rpm. 111

List of Tables

| | | |
|-----|--|-----|
| 3.1 | Vehicle parameters | 31 |
| 3.2 | PMSM Parameters | 40 |
| 4.1 | Parameters of dSPACE DS1104 Controller Board | 49 |
| 4.2 | Specifications of the Electrical Load System | 52 |
| 4.3 | IGBT specifications | 52 |
| 4.4 | Torque Transducer Specifications | 56 |
| 4.5 | Autonics 1024 PPR Incremental Rotary Encoder Specifications | 57 |
| 5.1 | Comparative Evaluation of ANFIS Membership Function Types and Configurations | 64 |
| 5.2 | Torque Ripple under Steady State Operation | 73 |
| 5.3 | Comparative Performance of PI-HCC and ANFIS-HCC under Varying Operating Conditions | 75 |
| 5.4 | Energy Efficiency Comparison of PI-HCC and ANFIS-HCC Controllers | 78 |
| 6.1 | Comparative Simulation Results of Torque Ripples | 88 |
| 6.2 | Comparative Experimental Results of Torque Ripples | 90 |
| 6.3 | Comparative Experimental Results of Current Ripples | 90 |
| 7.1 | Comparison of Chattering Mitigation Techniques | 103 |
| 7.2 | Computational Complexity of ANFIS-SMCC vs. Other Controllers. | 104 |
| 7.3 | Simulated performance of ANFIS-based controllers under test conditions. | 107 |
| 7.4 | Experimental performance of ANFIS-based controllers under test conditions. | 112 |
| 7.5 | Comparison of Torque and Current Ripple under Practical Constraints | 113 |

Chapter 1

Introduction

1.1 Background and Motivation

Electric vehicles (EVs) play a crucial role in dealing with energy dependence, environmental pollution, and greenhouse gas emissions linked to traditional internal combustion engine vehicles. It is important to recognize that the renewed interest in EVs emerged during the 1973 oil crisis, shedding light on the vulnerabilities of relying on fossil fuels. The modern EVs, which run solely on electricity and are recharged through the power grid, present unique challenges and opportunities for integration with current infrastructure. We should acknowledge that stringent regulations, like California's zero-emission vehicle rules, have stimulated progress in power electronics technology that is essential for EV propulsion and battery charging. Even though high initial costs and limited driving ranges pose obstacles to widespread adoption, battery electric vehicles (BEVs) and fuel cell vehicles (FCVs) are seen as eco-friendly, especially when powered by renewable energy sources. The support provided by government policies and subsidies in various regions, such as Europe, the USA, and China, is crucial in accelerating the development of EV technology. The industry is actively working on improving charging infrastructure and creating smart grids to ensure compatibility with existing power systems. It is evident that advancements in battery chargers, drive systems, and control systems from multiple disciplines are pivotal in enhancing EV efficiency and performance. The environmental advantages of EVs cannot be overstated, as they lead to significant reductions in greenhouse gas emissions and air pollution, playing a vital role in sustainable transportation. The foundation for modern EV

performance enhancements has been laid by early research utilizing innovative methods. The interaction between technological progress, regulatory frameworks, and market demands continues to shape the landscape of EVs, highlighting the importance of this area for further research and development. Overcoming challenges related to pricing, planning, and infrastructure compatibility is crucial for fully realizing the potential of EVs in mitigating environmental and energy security impacts. The ongoing efforts to advance EV technologies and infrastructure underscore their critical role in the future of transportation, offering a cleaner, more sustainable, and energy-efficient mobility solution on a global scale.

1.1.1 Overview of Electric Vehicles (EVs)

The global adoption of electric vehicles (EVs) is experiencing exponential growth, driven by technological advancements, regulatory support, and increasing consumer awareness of environmental issues. As of 2022, there were 26 million electric cars on the road globally, with half of them in China [1]. The market for EVs is projected to reach 858.00 billion by 2027 [2]. This growth is supported by significant investments in EV and battery technologies, which reached nearly \$2.1 billion in 2022, marking a 30 % increase from the previous year. The Model for International Electric Vehicle Trade (MONET) indicates that future EV production will be regionally concentrated, with North America, Europe, Japan, South Korea, and China being major players [3]. Technological advancements in battery systems, drivetrain solutions, and charging infrastructure are pivotal in this growth, with innovations such as smart charging networks and wireless power transfer expected to enhance user convenience and integration with smart city infrastructure. Despite the rapid growth, challenges remain, including the need for extensive charging infrastructure and the impact of EV charging on power grids. The adoption of battery electric vehicles (BEVs) is expected to significantly reduce greenhouse gas emissions from road transport, with projections indicating that the majority of passenger cars in Europe will be electric by 2031 [4]. By 2050, nearly 2 billion vehicles will need to be either battery EVs or fuel cell-based vehicles to achieve net-zero emissions from road vehicles [1]. The global EV fleet is projected to grow from 5 million vehicles in

1.1. Background and Motivation

3

2018 to about 95–105 million by 2030, and 585–823 million by 2050, constituting one-third to one-half of the overall light-duty vehicle fleet [5]. The diffusion of BEVs is expected to accelerate, with global sales growing from 5.3 million units in 2019 to nearly 40 million by 2030, necessitating an increase in charging stations from 2 million to 10 million units in the same period. The environmental impact of widespread EV adoption is substantial, with the potential to significantly reduce CO₂ emissions and reliance on fossil fuels. However, economic and geopolitical factors, such as inflation and high interest rates, may influence the pace of adoption, as seen in the reduced optimism among automotive executives regarding EV market penetration [2]. Overall, the future of EV adoption looks promising, with continued advancements in technology and supportive policies paving the way for a more sustainable transportation system globally [6].

1.1.2 Role of PMSM in EVs

PMSMs are increasingly preferred for EV applications due to their high power density, efficiency, and reliable performance. PMSMs offer notable advantages, including high torque density and superior efficiency, which make them well-suited for EV traction drives [7]. PMSM employed for electrical vehicle application must possess not only superior performance but also ensure safety and reliability for vehicle operations. The performance of PMSMs can be significantly enhanced through optimized design using advanced algorithms such as the hybrid artificial bee colony algorithm–support vector machine (HAS), which effectively navigates the complex design space to achieve optimal configurations with minimal computational effort. Innovative rotor designs, such as the "VV—" shape, further improve torque performance, reduce torque ripple, and minimize cogging torque, which helps to decrease vibration and noise in EVs [8]. Control strategies are also critical; improved sliding mode and proportional resonance controls enhance dynamic performance and robustness under varying conditions. Additionally, flux-weakening (FW) algorithms enable efficient operation over a broad constant-power speed range, essential for high-speed applications [9]. The reverse-salient PMSM (RSPMSM), with its variable flux leakage and saliency ratio, offers high torque performance, particularly in flux-weakening conditions, making it suitable for EVs. Current

sensorless control methods, like the maximum torque per ampere (MTPA) technique with streamline control architecture improves system response and energy efficiency [10]. Safety and reliability can be ensured with techniques such as the stepwise non-transient approach protecting the motor and controller from excessive transient currents and voltage overshoots, thereby enhancing overall safety [11]. The integration of PMSMs is further optimized by balancing motor geometry, bus voltage, and battery sizing to improve powertrain longevity and cost-effectiveness [12]. Nonlinear control techniques, including sliding mode control (SMC), offer reduced steady-state error and enhanced robustness against parameter variations and load disturbances [13]. For urban lightweight EVs, design focuses on reducing motor vibrations and improving energy efficiency through structural modifications like stator chambers and rotor notches [14]. These advancements in PMSM design, control strategies, and safety measures highlight their crucial role in developing efficient, reliable, and high-performance electric vehicles.

1.1.3 Challenges in PMSM Application for Electric Vehicles

PMSMs are widely recognized as the preferred choice for EV traction systems due to their superior efficiency, high torque density, and compact form factor. However, despite their advantages, several challenges hinder the full exploitation of PMSMs in EV applications. These challenges stem from both the inherent characteristics of the motor and the demanding requirements of real-world automotive environments.

1. **Torque and Current Ripple:** One of the most significant issues in PMSM drives is the presence of torque ripple, which leads to mechanical vibrations, acoustic noise, and reduced ride comfort. This phenomenon becomes more pronounced at low speeds and is exacerbated by high pole-pair counts commonly used to increase torque density. Similarly, stator current ripples can cause increased losses, overheating, and electromagnetic interference (EMI), deteriorating the motor's overall efficiency and lifespan. Effective ripple minimization remains a major control challenge in the dynamic operating conditions of EVs.

1.1. Background and Motivation

5

2. **Parameter Sensitivity and Uncertainties:** PMSM performance is highly dependent on motor parameters such as stator resistance, inductance, and rotor flux linkage. These parameters are not constant and vary with temperature, load, and operating conditions. Inaccurate estimation of these parameters leads to performance degradation, including poor torque control, incorrect flux estimation, and instability in closed-loop systems. Traditional control strategies such as Field Oriented Control (FOC) are especially vulnerable to these uncertainties, requiring precise modeling for reliable operation.
3. **Thermal Management:** Due to high current densities and compact motor design, PMSMs in EVs are subject to significant thermal stresses. Inadequate thermal management can cause demagnetization of permanent magnets, reduced efficiency, and long-term reliability issues. Effective cooling strategies must be integrated with control algorithms that can adapt to temperature-induced parameter variations in real-time.
4. **Flux-Weakening Operation and High-Speed Control:** To extend the speed range of EVs, PMSMs are often operated in the flux-weakening (FW) region, where the control strategy must dynamically regulate the stator voltage and current within safe limits. Achieving high-speed performance without compromising torque and efficiency is a major control challenge. Inaccurate FW control can result in overvoltage, instability, or insufficient torque during acceleration or hill climbing.
5. **Sensor Dependence and Fault Tolerance:** Precise rotor position sensing is critical for vector control of PMSMs. However, mechanical encoders are expensive, vulnerable to faults, and reduce overall system reliability. While sensorless control methods have been proposed, their performance deteriorates at low speeds or under sudden load changes. Additionally, PMSM drives in EVs must be resilient to sensor faults, inverter failures, or abrupt driving maneuvers—necessitating robust, fault-tolerant control architectures.
6. **Computational and Implementation Constraints:** Advanced control techniques such as Model Predictive Control (MPC), Sliding Mode Control

(SMC), and Reinforcement Learning (RL)-based controllers can significantly improve dynamic response and robustness. However, they require high computational power, fast sampling rates, and complex tuning procedures, which pose a challenge for real-time implementation on embedded automotive platforms like DSPs or microcontrollers.

7. **Cost and Magnet Material Concerns:** PMSMs typically require rare-earth magnets (e.g., NdFeB) to achieve high torque density. The fluctuating cost and geopolitical supply risks associated with these materials affect the commercial scalability of PMSM-based EV drives. In addition, ensuring demagnetization resistance under high thermal loads and fault conditions remains an open design problem.

1.2 Research Objectives

1. **Mathematical Modeling and analysis of high performance FOC design of PMSM for EV application** Analyzing and modeling for high-performance Field-Oriented Control of PMSM in EV . Developing dynamic equations for electrical and mechanical systems. Applying transformation techniques like Park and Clarke, creating control algorithms, and validating through simulation to optimize torque and speed regulation.
2. **Development and Implementation of control algorithm for encoder based PMSM drive system.** Develop and execute a control algorithm for an encoder-based PMSM drive system. Create feedback loops with rotor position data from the encoder. Utilize vector control techniques for accurate torque and speed control. Incorporate a PI or advanced controller for regulation. Validate the algorithm through simulations and real-world testing.
3. **Performance enhancement of PMSM drive by minimizing Stator Current Ripples and Torque Ripples.** Improving the performance of a PMSM drive by reducing stator current and torque ripples, it is recommended to employ sophisticated control methodologies, utilize high-resolution encoders for

1.3. Organization of Thesis

7

precise feedback, and incorporate adaptive filtering to mitigate harmonic interferences within the drive system.

4. **Laboratory prototype development to test and validate the proposed methodology** Design a scaled-down PMSM drive system with motor, inverter, and control hardware for testing the methodology. Implement control algorithms on a DSP or microcontroller, integrate sensors for feedback, and use data acquisition tools for performance analysis under different conditions.

1.3 Organization of Thesis

Chapter 1: The introduction discusses electric vehicles' significance in the automotive industry, focusing on PMSM. It emphasizes the need to enhance PMSM performance for better EV efficiency and competitiveness. Specific challenges faced by PMSM in EVs include efficiency limits, torque ripple, and thermal management problems. Research goals aim to improve PMSM performance through innovative control strategies and design enhancements. The study's research questions, scope, and limitations are outlined. The thesis structure is briefly introduced, providing an overview of upcoming chapters.

Chapter 2: This section presents a technical review of literature on PMSM applications in EV , beginning with a comparison of motor architectures. It systematically examines key performance issues, including efficiency optimization and torque ripple suppression. The review covers conventional control strategies such as PID and Field-Oriented Control (FOC), as well as advanced approaches including predictive, adaptive, and intelligent control methods. It further highlights recent developments in control-based performance enhancement and system-level engineering, while identifying emerging research trends and unresolved technical challenges in PMSM drive systems.

Chapter 3: This chapter explores the mathematical modeling of the PMSM drive and EV systems that were conducted as part of the research. It begins with

a detailed explanation of the modeling approach, including the mathematical equations and parameters employed to model both the PMSM and the electric vehicle system. The chapter then offers a thorough analysis of performance metrics such as efficiency, torque ripples, and current ripples, with visual tools like charts and graphs used to illustrate the improvements achieved. The chapter concludes by discussing the findings, interpreting the results within the context of PMSM applications in EV .

Chapter 4: This chapter highlights the hardware setup, providing an in-depth description of the equipment and components used to test the enhanced PMSM drivetrain. It details how control systems are integrated with physical hardware, such as power converters, sensors, actuators, and the PMSM. The chapter emphasizes the importance of hardware elements, particularly the drivetrain, in translating research findings into practical PMSM applications, showcasing the real-world application of theoretical advancements.

Chapter 5: This chapter presents an ANFIS-enhanced Hysteresis Current Control (HCC) strategy to improve PMSM performance in EV . By reducing torque and current ripples, the method ensures smoother operation and higher energy efficiency. Simulation and experimental results confirm its advantages over traditional PID control, making it a strong candidate for quieter, more efficient EV drives.

Chapter 6: This chapter describes an advanced control technique combining ANFIS with Model Predictive Current Control (MPCC) to enhance PMSM performance in EV . The ANFIS-MPCC approach effectively minimizes torque and current ripples, resulting in smoother operation and increased energy efficiency. Validated by simulations and experiments, this method outperforms traditional controls. By addressing ripple challenges, it contributes to quieter, more efficient PMSM drives, advancing electric vehicle technology and offering superior performance and reliability to consumers.

Chapter 7: This chapter presents the design and implementation of an Adaptive Neuro-Fuzzy Inference System-based Sliding Mode Current Controller

1.4. Conclusion

9

(ANFIS-SMCC) for torque ripple and current ripple mitigation in PMSM drives. By combining SMC's robustness with ANFIS's learning capability, the proposed controller achieves real-time adaptability, smooth current regulation, and resilience under practical EV operating conditions.

Chapter 8: The concluding chapter summarizes the key findings of the research, reviewing the objectives and emphasizing the study's significant contributions to PMSM performance enhancement. Additionally, the chapter identifies potential areas for future research, suggesting directions for further investigation to build upon this study and continue advancing PMSM technology for EV .

1.4 Conclusion

This chapter introduces the past and future of EVs, emphasizing the significant role of PMSMs in enhancing EV performance. The chapter outlines these key challenges and presents the thesis objectives aimed at optimizing PMSM efficiency and reliability in EV applications. Additionally, the thesis organization is discussed, demonstrating how each section contributes to the broader understanding of PMSM technology and its impact on the sustainable evolution of EVs, driving innovations for the future of electric transportation.

Chapter 2

Literature survey

2.1 Overview of EVs and their growing importance.

EVs are increasingly crucial in the transition to sustainable transportation due to their potential to reduce greenhouse gas emissions and dependence on fossil fuels . Their popularity is driven by zero operational emissions, higher energy efficiency, and lower maintenance costs compared to traditional vehicles, although high initial costs remain a barrier .EVs integration is not just a response to environmental concerns but also a strategy for diversifying energy sources and enhancing energy security . Governments are actively encouraging EVs adoption through incentives, which have significantly boosted market penetration despite early-stage risks [15].

China leads the global EVs market, with Europe and the USA following, signaling a shift in automotive trends [16]. However, widespread EVs use presents challenges, such as the need for extensive charging infrastructure and the management of increased peak loads on power grids [17, 18]. Smart charging solutions and advanced control strategies are essential to maintain grid stability and optimize charging efficiency [18, 19]. Moreover, the integration of hybrid energy systems, such as lithium-ion batteries and fuel cells, enhances the overall efficiency and extends the driving range of EV [20]. Although EVs improve air quality and public health, local factors influence these benefits [21]. Advancements in battery technology and integration with renewable energy sources further reduce the transportation sector's carbon footprint [17–19]. Nonetheless, safety concerns, including fire risks and post-accident procedures,

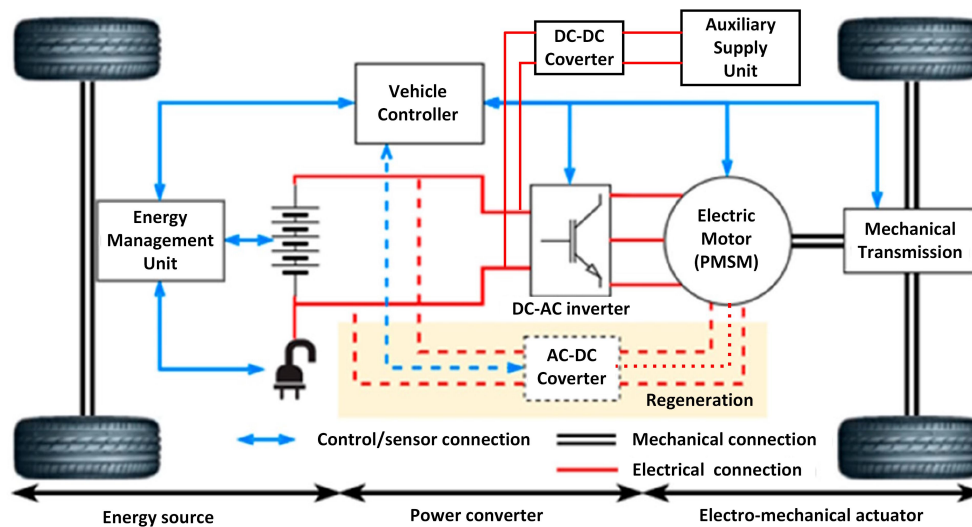


FIGURE 2.1: Components of an EV drivetrain

remain critical issues that require ongoing attention [16]. Overall, the significance of EVs in sustainable transportation is emphasized by environmental benefits, technological advances, and supportive policies, contributing to a more resilient transportation system.

To better understand how these advancements are realized in practice, the technical diagram in Figure. 2.1 illustrates the core components and energy flow within an EV drivetrain. The high-voltage battery pack stores electrical energy, which is managed by a Battery Management System (BMS) to ensure safety and efficiency. Power is delivered to the inverter, which converts DC to AC for the electric motor. The motor generates torque, transmitted via the reduction gear to the wheels, propelling the vehicle. An onboard charger enables external AC charging, while the control unit coordinates system operation and regenerative braking, which recovers kinetic energy during deceleration. This architecture enables efficient, emission-free transportation in modern EVs.

2.2. Architecture and Advanced Control of PMSM Drives for EV Applications 13

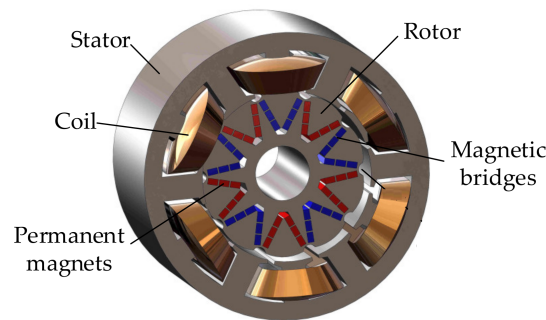


FIGURE 2.2: Structure of PMSM

2.2 Architecture and Advanced Control of PMSM Drives for EV Applications

PMSM are central to electric vehicle propulsion systems due to their high power density, superior efficiency, and dynamic performance. Understanding their construction, operational principles, and classification is essential for optimizing motor behavior under varying load and speed conditions. This study discusses the structural components of PMSMs, distinguishes between surface-mounted and interior magnet configurations, and outlines their key operating modes, such as Maximum Torque Per Ampere (MTPA), Flux Weakening (FW), and regenerative braking. These aspects form the foundation for developing advanced control strategies tailored to the performance demands of modern EVs.

2.2.1 Construction, Types, and Operating Modes of PMSM

A PMSM is a type of synchronous motor that uses permanent magnets embedded in the rotor to create a constant magnetic field. The construction of a PMSM typically includes a stator, rotor, and various control systems as shown in Figure 2.2. The stator is composed of a core and windings, which are usually made of copper wire wound in a specific pattern to create a magnetic field when current flows through them [22]. The rotor contains permanent magnets, which can be arranged in different topologies such as surface-mounted or embedded within the rotor core [23]. The motor operates on the principle of synchronous

rotation, where the rotor and the stator magnetic fields rotate at the same speed. The stator windings are powered by an AC supply, which creates a rotating magnetic field. This field interacts with the magnetic field of the rotor magnets, producing torque and causing the rotor to turn in sync with the stator field [24].

The working principle of PMSM involves several key aspects. Firstly, the motor's speed and torque are controlled by varying the frequency and amplitude of the AC supply to the stator windings. Advanced control techniques such as vector control or FOC are often employed to achieve precise control over the motor's performance. These methods involve controlling the motor's current in a way that decouples the torque and flux-producing components, allowing for efficient and dynamic control [25]. Additionally, PMSMs can operate in different modes, including constant torque and flux-weakening modes. In the flux-weakening mode, the motor can achieve higher speeds by reducing the magnetic flux in the air gap, which is often accomplished by adjusting the current in the stator windings [26]. PMSMs are also equipped with various control systems to enhance their performance and reliability. For instance, the use of sliding mode control (SMC) algorithms can improve the robustness and reduce chattering in the control system [27]. Moreover, PMSMs can be designed to operate without position sensors, using sensorless control techniques that estimate the rotor position based on the motor's electrical characteristics [28]. This not only reduces the cost but also increases the reliability of the motor. In applications requiring high starting torque and a wide field-weakening range, PMSMs with specific magnetic circuit topologies are designed to meet these requirements [23]. Furthermore, PMSMs are widely used in various applications due to their high efficiency, reliability, and superior control performance. They are commonly found in CNC machine tools, where they control the cutting feed motion of the machine tool axes [25]. In hybrid and EV, PMSMs are favored for their high torque density and efficiency [23]. The development of advanced algorithms and control methods, such as those based on backstepping control, further enhances the performance of PMSMs by providing fast dynamic response and minimal steady-state error [29]. Overall, the construction and working principle of PMSMs make them a versatile and efficient choice for a wide range of applications.

PMSMs are categorized primarily into Surface-mounted PMSMs (SPMSMs)

2.2. Architecture and Advanced Control of PMSM Drives for EV Applications 15

and Interior PMSMs (IPMSMs) as shown in Figure. 2.3, each with distinct characteristics and applications. SPMSMs feature a simple magnetic circuit design, fast responsiveness, linear torque-current characteristics, and constant operating speed, making them suitable for applications requiring precise control and high efficiency [30]. They are widely used in industrial applications due to their high efficiency and precise control capabilities [31]. On the other hand, IPMSMs have high power densities because they can utilize both magnetic and reluctance torque, offering a wider operating range when flux-weakening control is employed [30]. This makes IPMSMs particularly attractive for high-performance applications such as EV, where a broad speed range and high efficiency are crucial [32]. Additionally, the construction of permanent magnets in the rotor is critical for the performance of Line-start PMSM (LSPMSMs), which are emerging as high-efficiency alternatives to traditional induction motors, contributing to energy efficiency and sustainability [33]. Advanced control methods, such as non-linear control techniques, are being developed to handle the complex dynamics and non-linearity inherent to PMSMs, further enhancing their performance [31]. Moreover, innovative strategies like the flux observation transfer-based inductance identification and sliding mode control are being employed to improve the accuracy and robustness of PMSM control systems [34]. These advancements highlight the ongoing research and development efforts aimed at optimizing the performance and expanding the application range of PMSMs, making them a versatile and efficient choice for modern electric drive systems [35, 36].

PMSM operate under distinct control modes tailored to specific speed and load conditions to ensure optimal performance and energy efficiency. In low-speed motoring, the MTPA strategy is employed [37]. This mode focuses on minimizing current consumption while maximizing torque output by optimally aligning the stator current vector with the rotor flux. MTPA enhances overall drive efficiency and reduces copper losses, making it ideal for city driving and low-speed acceleration. As the motor transitions to high-speed motoring, it reaches a point where the back-EMF approaches the DC bus voltage limit. To extend the speed range beyond this base speed, FW control is activated [38]. This technique deliberately injects negative d-axis current to reduce the resultant air-gap flux, allowing safe operation at higher speeds without exceeding voltage

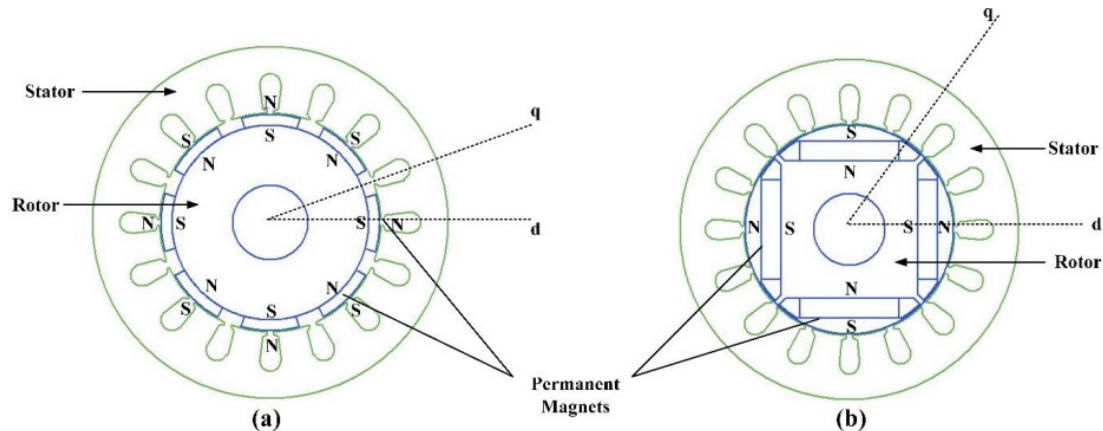


FIGURE 2.3: Rotor configuration of PMSM (a) SPMSM (b) IPMSM

constraints. In regenerative braking mode [39], the PMSM acts as a generator. Instead of consuming electrical energy, it converts the kinetic energy of the vehicle into electrical energy during deceleration. This recovered energy is fed back to the battery, improving overall energy efficiency and extending vehicle range.

Together, these operating modes MTPA at low speeds, FW at high speeds, and regenerative braking during deceleration enable PMSM drive systems to deliver efficient, high-performance operation across the full range of vehicle conditions.

2.2.2 PMSM Control strategies

The control strategies for PMSMs, as illustrated in Figure 2.4, are broadly categorized into Scalar Control and Vector Control under the umbrella of Variable Frequency Drives (VFDs). Scalar control is a simpler technique that maintains a fixed voltage-to-frequency ratio ($V/f = \text{constant}$) or adjusts the stator current as a function of rotor speed ($I_s^* = f(\omega_r)$). While easy to implement, scalar methods offer limited dynamic performance and are typically suited for low-cost, low-performance applications.

Vector control offers a more advanced and dynamic approach by enabling decoupled control of torque and flux. One of the principal methods in this category is FOC, which can be implemented based on rotor flux orientation using either direct or indirect methods or stator flux orientation, depending on the

2.2. Architecture and Advanced Control of PMSM Drives for EV Applications 17

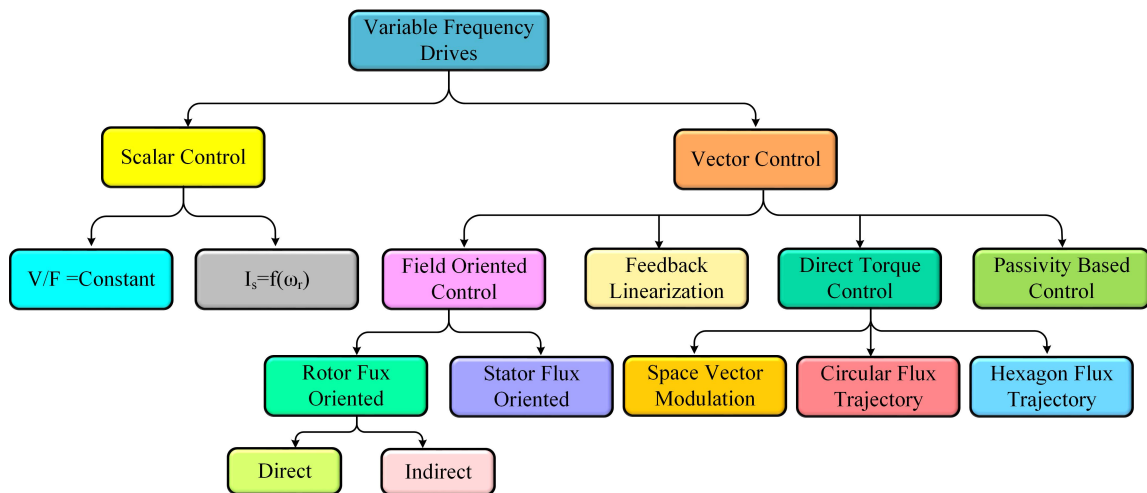


FIGURE 2.4: Classification of variable frequency drives

system requirements. FOC, also known as vector control, is widely used for its ability to decouple torque and flux control, providing precise and rapid torque response. Recent advancements include the introduction of sliding mode control schemes, which improve dynamic torque and speed response while enhancing robustness to parameter variations and external disturbances, as demonstrated in permanent magnet AC motors[40]. Direct Torque Control (DTC) is another key vector control technique that directly regulates torque and flux through instantaneous error correction. Traditional DTC methods, however, suffer from issues such as large torque ripple and variable switching frequency. To address these, various improvements have been proposed. For instance, a novel DTC strategy eliminates common-mode voltage spikes caused by dead-time effects, maintaining a simple control structure without hardware modifications. Additionally, the use of virtual voltage vectors (VVs) in DTC strategies for multiphase machines has shown significant improvements in current regulation and reduced flux/torque disturbances [41]. Another advanced DTC method, deadbeat direct torque and flux control (DB-DTFC), reduces electromagnetic torque ripple and improves dynamic response and robustness to motor parameter variations [42]. Furthermore, observer-based optimal DTC strategies have been developed for SPMSM drives, offering improved transient and steady-state performance with less computational burden and enhanced robustness. DTC performance can be further refined using modulation strategies

such as Space Vector Modulation (SVM), Circular Flux Trajectory, or Hexagon Flux Trajectory, which help minimize torque ripple and switching losses[43, 44].

Feedback Linearization [45] is a vector-based control technique that cancels system nonlinearities, thereby simplifying the control structure and enhancing dynamic performance. In addition, Passivity-Based Control[46] introduces an energy-oriented framework that enhances system stability and robustness, particularly under variable load and dynamic operating conditions.

2.2.3 Integration and Role of PMSM in EV

EVs have specific performance requirements that are critical for their acceptance and efficiency, including driving range, acceleration, and regenerative braking capabilities. The driving range is a fundamental requirement for EVs, as it determines the distance an EV can travel on a single charge. Studies show that many existing analyses underestimate range requirements by focusing on one-day analyses and mean daily trip distances, whereas longitudinal mobility data provide a more accurate picture. For instance, GPS-recorded driving cycles indicate that 80% of small-scale vehicles, 67% of midsize vehicles, and 40% of sport utility vehicles can meet their range requirements with current EV technology [47]. Acceleration performance is another crucial aspect, often enhanced by advanced motor control systems. For example, the use of an interior PMSM (IPMSM) drive with a two-leg interleaved bidirectional front-end dc/dc buck-boost converter can significantly improve high-speed driving performance and acceleration by establishing adjustable and boostable dc-link voltage [48]. Regenerative braking (RBS) is a key technology for extending the driving range by recovering energy that would otherwise be lost during braking. Various control strategies, such as fuzzy logic, neural networks, and sliding mode control, have been developed to optimize energy regeneration without compromising vehicle performance [49]. A fuzzy-logic-based RBS, for instance, can improve energy recuperation efficiency by determining the optimal distribution between friction and regenerative braking forces, thereby enhancing the driving range by up to 25.7% [50]. Additionally, the integration of electric motors/generators as actuators in the braking system allows for faster torque response and better energy feedback, which is crucial for maintaining braking

2.2. Architecture and Advanced Control of PMSM Drives for EV Applications 19

safety under complex conditions [51]. The use of a sliding mode robust controller (SMRC) has been shown to improve the drive range of EVs by about 17% through effective energy-regeneration control [39]. Moreover, a parallel-distribution braking system with gain-scheduling super-twisting sliding mode control (GSTSMC) can capture maximum kinetic energy during braking, increasing the state of charge (SOC) and overall efficiency while maintaining vehicle stability [52]. The choice of refrigerants in EV cooling systems also impacts performance, as low-Global Warming Potential (GWP) refrigerants can enhance energy efficiency and cooling capacity, thereby indirectly affecting the driving range by reducing the cooling load [53]. Finally, the comparison between serial and parallel regenerative braking strategies reveals that serial regenerative braking outperforms parallel strategies in terms of energy recuperation, making it a more promising approach for future developments [54]. Overall, these performance requirements and technological advancements are crucial for the continued development and acceptance of EVs in the market. The integration of PMSMs with other EV components, such as battery management systems, is a multifaceted approach aimed at enhancing the overall performance and efficiency of EVs. A dual three-phase PMSM drive can be connected with ultracapacitors and batteries through inverters to achieve hybrid energy storage system power management, improving dynamic response and seamless transient processes [55]. Additionally, a segmented three-phase interior PMSM (IPMSM) can serve as an inductor filter for integrated battery chargers, optimizing stator winding inductance to manage grid current harmonics during charging and vehicle-to-grid (V2G) modes [56]. This configuration can be further enhanced by using a nine-winding segmented three-phase PMSM, which eliminates torque fluctuations and reduces core loss during charging/V2G modes, while maintaining a simple control strategy [57]. The hybrid energy storage paradigm (HESP) integrates PMSMs with supercapacitors and NMC-lithium batteries, managed by an advanced artificial neural network (ANN) to improve regenerative braking efficiency and energy storage during braking [58]. Moreover, battery thermal management systems (BTMS) incorporating composite phase change materials and polyimide heating films can be integrated with PMSMs to ensure optimal battery temperature control, enhancing safety and lifespan [59]. The use of hybrid proportional-integral (PI)

and sliding mode control (SMC) schemes for hybrid energy storage systems (HESS) with PMSMs further optimizes the performance by reducing tuning efforts and improving transient and steady-state conditions. Finally, integrated drivetrain models that include PMSMs, battery, and power electronics can simulate and validate system-level outputs, identifying energy-conscious actions that significantly reduce energy consumption and improve efficiency [60]. These integrated approaches collectively contribute to the advancement of EV technology, ensuring better performance, efficiency, and reliability.

2.2.4 Performance Enhancement through Advanced Algorithms

In EV applications, control of PMSM typically begins with the MTPA strategy, which aims to achieve the highest torque output for the least stator current magnitude. MTPA is effective at improving drive efficiency and reducing copper losses, especially in low-speed operating regions. However, its performance is highly sensitive to variations in motor parameters such as inductance and flux linkage, which are affected by temperature changes and magnetic saturation. Consequently, conventional MTPA control may result in suboptimal torque generation under practical, time-varying operating conditions [61, 62].

To overcome such parameter sensitivity, Adaptive Neuro-Fuzzy Inference Systems (ANFIS) have emerged as an artificial intelligence-based alternative. ANFIS combines the self-learning ability of neural networks with the rule-based reasoning of fuzzy logic, enabling it to adapt in real time to nonlinear dynamics and parameter uncertainties. In PMSM drives, ANFIS-based control has shown superior torque tracking accuracy, reduced overshoot, and improved robustness under fluctuating loads and speed conditions. Its ability to approximate system behavior from data makes it especially valuable in EV scenarios where precise system modeling is difficult [58].

Building on model-based predictive control, Finite Control Set Model Predictive Control (FCS-MPC) offers a dynamic control solution that predicts future motor behavior and selects the optimal inverter switching state at each sampling instance. Unlike continuous control approaches, FCS-MPC works with a discrete set of switching combinations, minimizing a predefined cost function that accounts for torque control, current regulation, and switching losses. Its fast

2.2. Architecture and Advanced Control of PMSM Drives for EV Applications 21

dynamic response, high precision, and constraint-handling capabilities make it particularly effective for PMSM control in EVs where real-time optimization is crucial [63, 64].

When robustness against uncertainties and disturbances is a primary concern, Sliding Mode Control (SMC) becomes a preferred method. SMC enforces system trajectories to follow a predefined sliding surface using discontinuous control action, ensuring finite-time convergence and resilience to parameter variations and external perturbations. In PMSM applications, SMC has proven effective for managing nonlinearities and ensuring stable operation under rapidly changing conditions. Hybrid PI-SMC structures have further enhanced both transient and steady-state performance while easing controller tuning requirements [65, 66]. Classical SMC, however, suffers from issues like chattering and limited adaptability, which restrict its deployment in dynamic EV environments [67].

To address these limitations, several enhanced SMC variants have been developed. Adaptive SMC algorithms introduce online gain tuning to accommodate changing system dynamics and improve speed regulation [68], while recursive SMC methods employ adaptive observers to eliminate the reaching phase and improve tracking smoothness [69]. Fixed-time SMC and barrier function-based controllers ensure rapid convergence and effectively handle actuator constraints such as input saturation [70]. Event-triggered SMC schemes have also been proposed to reduce computation and communication burden while maintaining control precision [71].

Recognizing the need for greater adaptability and ripple suppression, researchers have explored intelligent hybrid SMC approaches. Techniques such as ANFIS-SMC, fuzzy-SMC, and neural-network-assisted SMC aim to combine the robustness of SMC with the learning capabilities of soft computing. ANFIS-SMC, for instance, integrates neuro-fuzzy adaptation into the SMC framework to enable online tuning and enhanced noise rejection [72], while RBF-NN-aided SMC improves transient tracking based on prescribed performance bounds [73]. Although these intelligent extensions offer improved control precision and adaptability, they also introduce higher computational overhead, posing challenges for real-time implementation on embedded EV platforms.

Overall, the advancement of PMSM control algorithms—from classical MTPA

to intelligent SMC variants—reflects a shift toward more adaptive, robust, and predictive strategies to meet the dynamic and uncertain operating conditions typical of modern electric vehicle drive systems.

2.3 Technical and economic challenges.

PMSMs in EV drivetrain face challenges related to integration with regenerative braking and other components. Improving efficiency and reducing costs requires smart control methods and optimized powertrain design. Issues like complex design, changing motor parameters, and high production costs highlight the need for better models and advanced control strategies.

One significant limitation is the high complexity and strong coupling in the structure of PMSMs, which makes the design process challenging and often requires extensive parameter optimization to achieve optimal performance under various operating conditions [61]. Additionally, the conventional MTPA control, which is commonly used to optimize Joule loss, requires precise knowledge of motor parameters that can vary with operating conditions, leading to suboptimal performance when these parameters are not constant. Another challenge is the need for efficient control strategies that can handle the dynamic behavior of PMSMs, especially in the saturation area where the MTPA trajectory deviates significantly from the initial unsaturated parameters [62]. Furthermore, the design and current reference of PMSMs are coupled, affecting the back electromotive force (EMF) and making it difficult to simultaneously determine the optimal design and current reference under voltage limitations [74]. The performance evaluation of PMSMs also needs to consider the full speed range, temperature constraints, and induced voltage, which adds to the complexity of the design process [61]. In the context of EVs, PMSMs must be designed to provide continuous torque under varying road and weather conditions, which requires careful consideration of stator slot configurations, rotor configurations, and magnetic materials [75]. The use of finite element analysis (FEA) for design optimization, while effective, can be computationally intensive, and there is a need for faster and more reliable methods to evaluate motor performance [76]. Additionally, the emulation of PMSMs for testing purposes requires accurate

2.3. Technical and economic challenges.

23

replication of electrical and mechanical characteristics, which can be challenging due to the constraints on the converter DC bus voltage and the coupling network sizing [77]. The design of PMSMs for specific applications, such as electric bicycles, also involves trade-offs between motor size, weight, cost, and efficiency, with different rotor structures offering varying advantages and limitations [78]. Moreover, the commonly used PI control algorithms in industrial applications can suffer from limitations under certain operational conditions, particularly when dealing with parameter uncertainties and integral windup, which can affect torque production and overall performance [79]. Finally, existing PMSM models often rely on empirical formulations and standard design rules that may not be suitable for high-performance applications, highlighting the need for improved, holistic, and multiphysic models that can support optimized design methodologies [80].

Technically, PMSMs face issues related to dynamic performance and robustness, especially when motor parameters change or external environmental interferences occur. Advanced control strategies, such as improved sliding mode and proportional resonance theory, have been proposed to address these issues, enhancing the motor's dynamic performance and anti-interference capabilities [65]. Additionally, the integration of economic model predictive control (EMPC) can reduce electrical losses and improve system efficiency, thereby extending the cruising range of EVs [66]. However, achieving a wide constant-power speed range and high power factor at high speeds remains challenging, necessitating further research and development in motor design, such as the reverse-salient PMSM (RSPMSM) which shows promise in flux-weakening states [81]. Economically, the high cost of PMSMs is a significant barrier, as the motor constitutes a large portion of the overall vehicle cost. Efforts to reduce costs include optimizing motor topology, material applications, and control strategies [82]. Moreover, the need for high efficiency to maximize battery utilization adds to the complexity and cost of PMSM systems [83]. Sensorless speed control techniques, such as those using artificial neural networks (ANN), offer potential cost savings by eliminating the need for physical sensors, though they require sophisticated algorithms to maintain performance [83]. Furthermore, the use of wide-bandgap semiconductors like silicon carbide (SiC) MOSFETs in conjunction with PMSMs introduces electromagnetic interference (EMI) issues, complicating

the achievement of electromagnetic compatibility (EMC) standards and necessitating additional design considerations and testing infrastructure [84]. Despite these challenges, PMSMs are favored for their high torque density and efficiency, which are crucial for EV applications. Control strategies like FOC and DTC are commonly used, each with its own merits and shortcomings [85]. The adoption of fuzzy logic controllers can further enhance performance by handling non-linearities and uncertainties more effectively than traditional PI controllers [86]. Overall, while PMSMs offer significant advantages for EVs, addressing their technical and economic challenges requires ongoing innovation in motor design, control strategies, and cost reduction techniques to make them a more viable option for widespread adoption in the automotive industry.

2.4 Identified gaps in current research.

The research on PMSM has been extensive, focusing on their application in various industrial and automotive fields due to their high efficiency, power density, and torque-to-weight ratio. Despite the advancements, there are still several gaps identified in the current research that offer opportunities for further investigation and improvement. These gaps include:

1. **Dynamic Performance and Durability:** One of the key challenges with PMSMs is maintaining their dynamic performance and durability, which can be significantly affected by variations in motor parameters and environmental conditions. PMSMs must contend with unpredictable shifts in their operating environment, which can impair motor performance and lifespan.
2. **Torque Ripple:** Torque ripple is a critical issue for PMSMs, especially at low speeds where high pole numbers are required. This often leads to a reliance on rare earth magnets, increasing costs and complexity. Torque ripple can affect vehicle smoothness and stability, making it a major concern for automotive applications.
3. **Control Strategies:** While Traditional control strategies like Field-Oriented Control (FOC) and Direct Torque Control (DTC) are widely used, they

2.4. Identified gaps in current research.

25

often face limitations in terms of dynamic responsiveness and implementation complexity. Effective control strategies are essential for ensuring that PMSMs can adapt to varying operating conditions while maintaining optimal performance. However, achieving this remains a challenge due to the inherent complexity of PMSMs.

4. **Accurate Rotor Position Sensing:** Accurate rotor position sensing and current component regulation are necessary for smooth PMSM operation. These requirements are vital for effective motor control and optimal torque production but can be difficult to implement due to sensor inaccuracies and alignment issues.
5. **Integration with Electric Vehicle Systems:** Integrating PMSMs into electric vehicle systems involves challenges related to power electronics, energy management, and system compatibility. Ensuring that the motor aligns with the vehicle's electrical architecture while delivering the necessary performance is a complex task that requires careful coordination across multiple subsystems.
6. **Energy Efficiency and Cost:** Energy efficiency is a major concern, as PMSMs must deliver high performance without excessive energy consumption. Balancing efficiency with cost-effectiveness is critical, particularly given the high initial investment associated with PMSMs in EV.
7. **Environmental Considerations:** As the automotive industry shifts towards renewable energy sources, PMSMs face pressure to align with these environmental goals. Meeting sustainability targets without compromising performance or increasing costs remains a significant challenge.

These identified gaps highlight the potential for significant advancements in the performance and application of PMSMs, particularly in electric vehicle technologies. Addressing these gaps through detailed study and innovative research could lead to more efficient, reliable, and cost-effective PMSM systems

2.5 Conclusion

This chapter presents an overview of the existing literature regarding the application of PMSM in EVs. The study highlights the ongoing efforts and future directions in PMSM research and development, emphasizing the importance of addressing technical and economic challenges, bridging research gaps, and leveraging emerging trends to enhance the effectiveness and use of PMSMs in EV and other fields.

Chapter 3

Modeling and Simulation of PMSM Drive for EV application

3.1 Introduction

Accurate modeling of EV drivetrains, especially those using PMSMs, is essential for improving overall efficiency. By simulating the interaction between motors, inverters, and batteries, it becomes possible to evaluate and optimize the propulsion system before creating physical prototypes. This chapter highlights how such modeling enables the development of control strategies while addressing real-world challenges, and supporting informed component selection.

3.2 Mathematical Modeling of EV

It is imperative for every EV to exhibit performance characteristics that ensure safe integration with regular urban traffic. To achieve this, a comprehensive understanding of the various forces influencing the dynamics of an EV is essential. This section aims to elucidate each of these forces, ultimately synthesizing their contributions to derive an expression for the total force that must be overcome. This total force signifies the effort required by the PMSM to induce the linear movement of the electric vehicle[87]. Figures. 3.1 and 3.2 offer a graphical depiction of the forces influencing the dynamics of the vehicle. Table 3.1 represents the vehicle parameters.

28 Chapter 3. Modeling and Simulation of PMSM Drive for EV application

Rolling resistance force The force of rolling resistance primarily arises due to the friction between the tire and the ground. This force remains relatively constant and is directly proportional to the total weight of the vehicle. The mathematical representation of this force is given by:

$$F_{rr} = \mu_{rr}mg \quad (3.1)$$

where μ_{rr} is the coefficient of rolling resistance, m is vehicle mass in kg, g is acceleration due to gravity

Aerodynamic drag force The aerodynamic drag force originates from the air resistance experienced by the moving vehicle body and is dependent on the frontal area. The equation governing this force is formulated as follows:

$$F_{ad} = \frac{1}{2}\rho AC_d v^2 \quad (3.2)$$

where, ρ represents the air density in kg/m^3 , A stands for the frontal area m^2 , v in m/s denotes the speed of the vehicle and C_d , known as the drag coefficient, decreases its value, enhancing the aerodynamics of the vehicle

Hill climbing force The force needed to drive the vehicle uphill on a slope ψ , designated as F_{hc} is essentially the weight of the vehicle component acting parallel to the incline. By analysing the forces, it can be represented as illustrated in Figure. 3.1 .

$$F_{hc} = mg \sin \psi \quad (3.3)$$

Acceleration force When the vehicle speed changes, an additional force beyond that depicted in Figure. 3.1 is necessary. This force, F_{la} , induces the linear acceleration of the vehicle and is described by Newton's second law equation,

$$F_{la} = ma \quad (3.4)$$

Both angular acceleration of the vehicle's rotating elements and linear acceleration must be considered.

3.2. Mathematical Modeling of EV

29

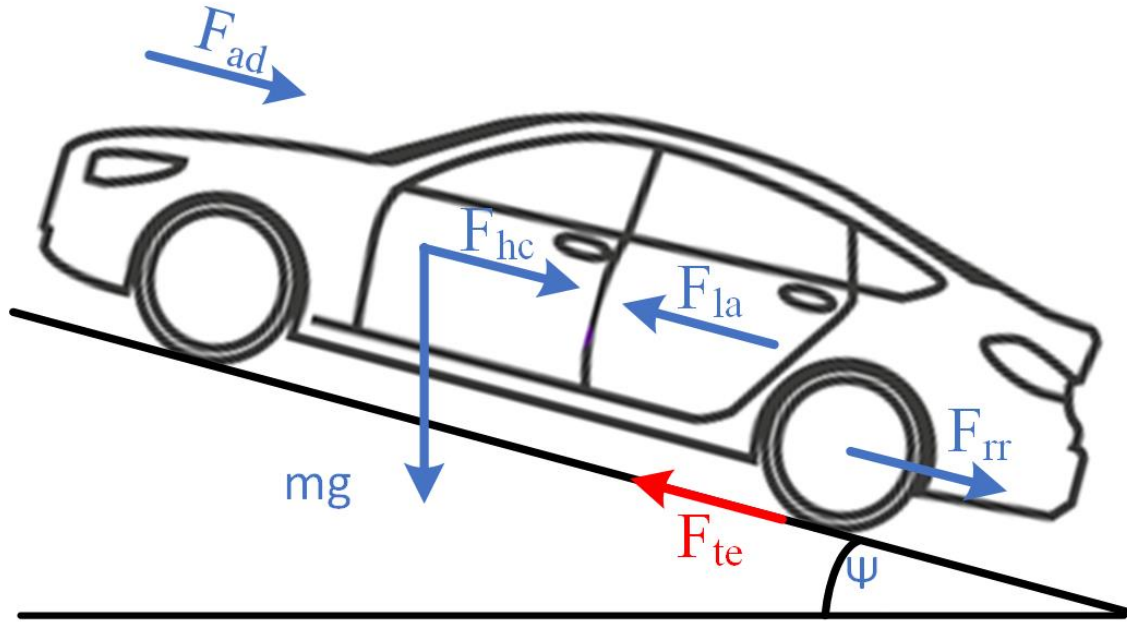


FIGURE 3.1: Forces acting on the vehicle

Figure. 3.2 illustrates a simple method of connecting the PMSM with the traction wheels. The angular force required is:

$$F_{\omega a} = I \frac{G^2}{\eta_g r^2} a \quad (3.5)$$

The angular force required is linked to the motor transmission ratio (G), moment of inertia (I) of the motor's rotor, gear efficiency (η_g) and the radius (r) of the drive wheels. This relationship is expressed as follows: for: $\omega < \omega_c$, or $< rG\omega_c$, then $T_L = T_{\max}$ where:

$$F_{te} = \frac{G}{r} T \quad (3.6)$$

$$F_{te} = \mu_{rr} mg + \rho AC_d v^2 + ma + I \frac{G^2}{\eta_g r^2} a \quad (3.7)$$

then substituting (3.6) in (3.7), we have:

$$T_L = \mu_{rr} mg \cdot \frac{r}{G} + \frac{\rho}{2} AC_d \omega^2 \cdot \frac{r^3}{G^3} + \left(m \cdot \frac{r}{G} + I \cdot \frac{G}{\eta_g r} \right) \cdot \omega \cdot \frac{r}{G} \quad (3.8)$$

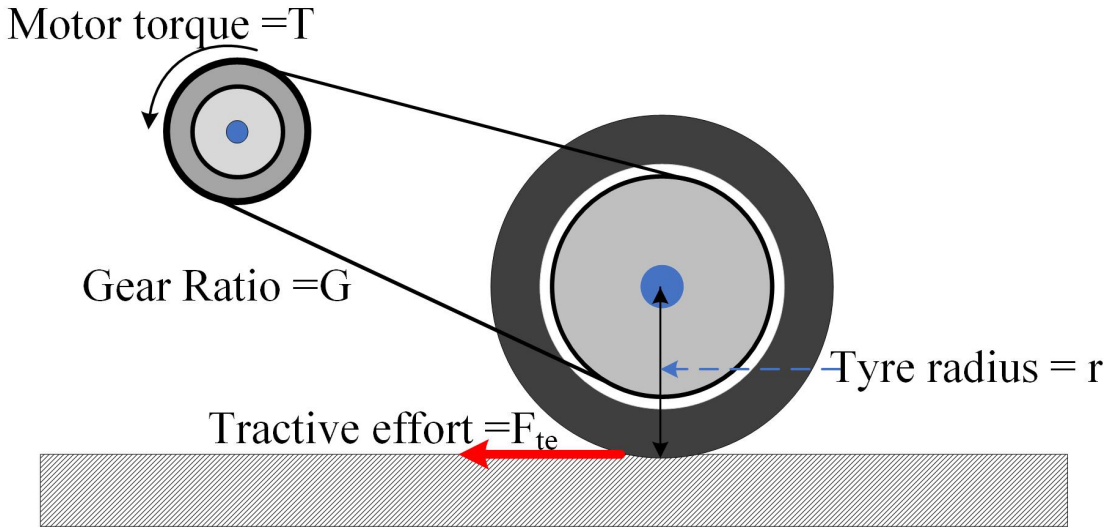


FIGURE 3.2: Motor Gear arrangement

Considering that the Torque equation of the PMSM is:

$$J\dot{\omega} = T_e - T_L \quad (3.9)$$

substituting (8) in (9):

$$\dot{\omega} = \frac{T_e - \left(\mu_{rr}mg \cdot \frac{r}{G} + \frac{1}{2}\rho AC_d \omega^2 \cdot \frac{r^3}{G^3} \right)}{J + m \cdot \frac{r^2}{G^2} + \frac{IG^2}{\eta_s r^2}} \quad (3.10)$$

The linear acceleration $\frac{dv}{dt}$ is given by:

$$\frac{dv}{dt} = \frac{T_e - \left(\mu_{rr}mg \cdot \frac{r}{G} + \frac{1}{2}\rho AC_d v^2 \right)}{\left(J + m \cdot \frac{r^2}{G^2} + \frac{IG^2}{\eta_s r^2} \right) \cdot \frac{r}{G}} \quad (3.11)$$

3.3 Mathematical Modeling of PMSMs

To facilitate controller design, simulation studies, and digital control implementation, a comprehensive mathematical model of the PMSM is essential. The model employs variable transformations to account for time-varying

3.3. Mathematical Modeling of PMSMs

31

TABLE 3.1: Vehicle parameters

| Parameters | Symbols | Value | Unit |
|---------------------------------|------------|--------|----------------|
| Vehicle mass | m | 340 | kg |
| Vehicle frontal area, | A | 2.35 | m ² |
| Wheel rolling radius, | r | 0.3048 | m |
| Gear natio, | G | 5 | - |
| Rolling resistance coefficient, | μ_{rr} | 0.005 | - |
| Wind resistance coefficient, | C_d | 0.4 | - |

inductances and differential equation coefficients. The PMSM equations are formulated in two reference frames: the stationary frame, where the stator is fixed, and the rotating frame, where the rotor is fixed. The stationary frame is typically used to analyze transient behavior due to its computational simplicity and static nature, while the rotating frame is preferred for small-signal stability analysis, capturing steady-state voltage and current imbalances.

3.3.1 PMSM Modeling in the Stationary a-b-c Frame

The voltage equations for a PMSM in the stationary a-b-c reference frame are given by :

$$\begin{bmatrix} v_{sa} \\ v_{sb} \\ v_{sc} \end{bmatrix} = R_s \begin{bmatrix} i_{sa} \\ i_{sb} \\ i_{sc} \end{bmatrix} + \frac{d}{dt} \begin{bmatrix} \phi_{sa} \\ \phi_{sb} \\ \phi_{sc} \end{bmatrix} \quad (3.12)$$

Here, v_{sa} , v_{sb} , v_{sc} represent stator voltages, and i_{sa} , i_{sb} , i_{sc} denote stator currents. The flux linkages ϕ_{sa} , ϕ_{sb} , ϕ_{sc} are expressed as :

$$\begin{bmatrix} \phi_{sa} \\ \phi_{sb} \\ \phi_{sc} \end{bmatrix} = L_{abc} \begin{bmatrix} i_{sa} \\ i_{sb} \\ i_{sc} \end{bmatrix} + \phi_m \begin{bmatrix} \cos \theta \\ \cos \left(\theta - \frac{2\pi}{3} \right) \\ \cos \left(\theta + \frac{2\pi}{3} \right) \end{bmatrix} \quad (3.13)$$

The inductance matrix L_{abc} is defined as :

$$L_{abc} = \begin{bmatrix} L_{aa} & L_{ab} & L_{ac} \\ L_{ba} & L_{bb} & L_{bc} \\ L_{ca} & L_{cb} & L_{cc} \end{bmatrix} \quad (3.14)$$

32 Chapter 3. Modeling and Simulation of PMSM Drive for EV application

In this matrix, L_{aa}, L_{bb}, L_{cc} are self-inductances, while $L_{ab}, L_{ba}, L_{ac}, L_{ca}, L_{bc}, L_{cb}$ are mutual inductances. The permanent magnet flux linkage magnitude is denoted by ϕ_m .

The flux linkage in equation (3.13) comprises contributions from stator currents and the permanent magnet. The self and mutual inductances incorporate a constant DC component and second-order harmonics, expressed as:

$$\begin{aligned} L_{aa} &= L_{0s} + L_{0a} - L_{ms} \cos 2\theta \\ L_{bb} &= L_{0s} + L_{0a} - L_{ms} \cos 2\left(\theta - \frac{2\pi}{3}\right) \\ L_{cc} &= L_{0s} + L_{0a} - L_{ms} \cos 2\left(\theta + \frac{2\pi}{3}\right) \\ L_{ab} &= L_{ba} = -\frac{L_{0s}}{2} - L_{ms} \cos 2\left(\theta - \frac{\pi}{3}\right) \\ L_{ac} &= L_{ca} = -\frac{L_{0s}}{2} - L_{ms} \cos 2\left(\theta + \frac{\pi}{3}\right) \\ L_{bc} &= L_{cb} = -\frac{L_{0s}}{2} - L_{ms} \cos 2(\theta + \pi) \end{aligned} \quad (3.15)$$

Here, L_{0s} and L_{0a} represent the stator winding's leakage and fundamental magnetizing inductances, respectively, while L_{ms} is the rotor-position-dependent inductance, which is zero for Surface PMSM and independent of rotor position. Using equations (3.13) and (3.15), the flux linkage derivative for phase A is:

$$\begin{aligned} \frac{d\phi_{sa}}{dt} &= \frac{d}{dt} (L_{aa}i_{sa} + L_{ab}i_{sb} + L_{ac}i_{sc} + \phi_m \cos \theta) \\ &= \frac{d}{dt} [(L_{aa} - L_{ac})i_{sa} + (L_{ab} - L_{ac})i_{sb} + \phi_m \cos \theta] \end{aligned} \quad (3.16)$$

This simplifies to:

$$\frac{d\phi_{sa}}{dt} = K_{a1}i_{sa} + K_{a2}\frac{di_{sa}}{dt} + K_{a3}i_{sb} + K_{a4}\frac{di_{sb}}{dt} - \phi_m\omega_r \sin \theta \quad (3.17)$$

3.3. Mathematical Modeling of PMSMs

33

where the coefficients are:

$$\begin{aligned} K_{a1} &= 2\omega_r L_{ms} \sin 2\theta - 2\omega_r L_{ms} \sin 2\left(\theta - \frac{\pi}{3}\right) \\ K_{a2} &= \frac{3}{2}L_{0s} + L_{ms} \cos 2\left(\theta + \frac{\pi}{3}\right) - L_{ms} \cos 2\theta \\ K_{a3} &= 2\omega_r L_{ms} \sin 2\left(\theta - \frac{\pi}{3}\right) - 2\omega_r L_{ms} \sin 2\left(\theta + \frac{\pi}{3}\right) \\ K_{a4} &= L_{ms} \cos 2\left(\theta + \frac{\pi}{3}\right) - L_{ms} \cos 2\left(\theta - \frac{\pi}{3}\right) \end{aligned} \quad (3.18)$$

For phase B, the flux linkage derivative is:

$$\frac{d\phi_{sb}}{dt} = K_{b1}i_{sa} + K_{b2}\frac{di_{sa}}{dt} + K_{b3}i_{sb} + K_{b4}\frac{di_{sb}}{dt} - \phi_m\omega_r \sin\left(\theta - \frac{2\pi}{3}\right) \quad (3.19)$$

with coefficients:

$$\begin{aligned} K_{b1} &= 2\omega_r L_{ms} \sin 2\left(\theta - \frac{\pi}{3}\right) - 2\omega_r L_{ms} \sin 2(\theta + \pi) \\ K_{b2} &= L_{ms} \cos 2(\theta + \pi) - L_{ms} \cos 2\left(\theta - \frac{\pi}{3}\right) \\ K_{b3} &= 2\omega_r L_{ms} \sin 2\left(\theta - \frac{2\pi}{3}\right) - 2\omega_r L_{ms} \sin 2(\theta + \pi) \\ K_{b4} &= \frac{3}{2}L_{0s} + L_{ms} \cos 2(\theta + \pi) - L_{ms} \cos 2\left(\theta - \frac{2\pi}{3}\right) \end{aligned} \quad (3.20)$$

The stator voltages are derived using equations (3.13) to (3.20):

$$\begin{aligned} v_{sa} &= R_s i_{sa} + K_{a1}i_{sa} + K_{a2} \cdot \frac{di_{sa}}{dt} + K_{a3}i_{sb} + K_{a4} \cdot \frac{di_{sb}}{dt} - \phi_m\omega_r \sin \theta \\ v_{sb} &= R_s i_{sa} + K_{b1}i_{sa} + K_{b2} \cdot \frac{di_{sa}}{dt} + K_{b3}i_{sb} + K_{b4} \cdot \frac{di_{sb}}{dt} - \phi_m\omega_r \sin\left(\theta - \frac{2\pi}{3}\right) \end{aligned} \quad (3.21)$$

Stator current derivative can be evaluated from equations (3.20) and (3.21)

$$\begin{aligned} \frac{di_{sa}}{dt} &= M_a = \frac{1}{K_{b4}K_{a2} - K_{a4}K_{b2}} \\ &\quad (K_{b4}v_{sa} - K_{a4}v_{sb} - [K_{b4}(R_s + K_{a1}) - K_{a4}K_{b1}]i_{sa} - [K_{a3}K_{b4} - K_{a4}(R_s + K_{b3})]i_{sb} \\ &\quad + K_{b4}\phi_m\omega_r \sin \theta - K_{a4}\phi_m\omega_r \sin\left(\theta - \frac{2\pi}{3}\right)) \end{aligned} \quad (3.22)$$

34 Chapter 3. Modeling and Simulation of PMSM Drive for EV application

$$\begin{aligned} \frac{di_{sb}}{dt} = M_b = & \frac{-1}{Kb_4Ka_2 - Ka_4Kb_2} \\ & (Kb_2v_{sa} - Ka_2v_{sb} - [Kb_2(R_s + Ka_1) - Ka_2Kb_1]i_{sa} - [Ka_3Kb_2 - Ka_2(R_s + Kb_3)]i_{sb} \\ & + Kb_2\phi_m\omega_r \sin \theta - Ka_2\phi_m\omega_r \sin \left(\theta - \frac{2\pi}{3} \right)) \end{aligned} \quad (3.23)$$

Stator current derivatives, $\frac{di_{sa}}{dt}$ and $\frac{di_{sb}}{dt}$, are expressed using M_a and M_b . The stator currents are computed discretely using the forward Euler method using equations (3.22) and (3.23) :

$$\begin{aligned} i_{sa}(k) &= M_a \cdot T_s + i_{sa}(k-1) \\ i_{sb}(k) &= M_b \cdot T_s + i_{sb}(k-1) \\ i_{sc}(k) &= -i_{sa}(k) - i_{sb}(k) \end{aligned} \quad (3.24)$$

The electromagnetic torque is formulated as:

$$\begin{aligned} T_e &= \frac{p}{2} \left(i_{abc}^T \frac{\partial L_{abc}(\theta)}{\partial \theta} i_{abc} + i_{abc}^T \frac{\partial \lambda_m(\theta)}{\partial \theta} \right) \\ N_1 &= i_{abc}^T \frac{\partial L_{abc}(\theta)}{\partial \theta} i_{abc} \\ N_2 &= i_{abc}^T \frac{\partial \lambda_m(\theta)}{\partial \theta} \end{aligned} \quad (3.25)$$

The torque is then:

$$T_e = \frac{p}{2} (N_1 + N_2) \quad (3.26)$$

The electromagnetic torque is expressed in standard form as:

$$T_e = \frac{p}{2} (\text{reluctance term} + \text{PM torque term}) \quad (3.27)$$

Clark's and Park's Transformations

The time-varying nature of PMSM voltage, flux linkage, and torque equations complicates three-phase AC machine models. Clark's and Park's transformations simplify these dynamics.

3.3. Mathematical Modeling of PMSMs

35

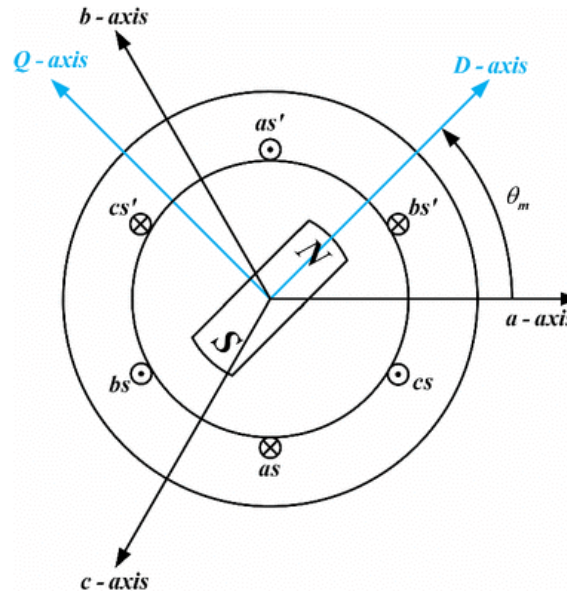


FIGURE 3.3: Two-Pole PMSM Diagram

Clark's transformation is :

$$\begin{bmatrix} v_{s\alpha} \\ v_{s\beta} \\ v_0 \end{bmatrix} = \frac{2}{3} \begin{bmatrix} 1 & -\frac{1}{2} & -\frac{1}{2} \\ 0 & \frac{\sqrt{3}}{2} & -\frac{\sqrt{3}}{2} \\ \frac{1}{\sqrt{2}} & \frac{1}{\sqrt{2}} & \frac{1}{\sqrt{2}} \end{bmatrix} \begin{bmatrix} v_{sa} \\ v_{sb} \\ v_{sc} \end{bmatrix} \quad (3.28)$$

Park's transformation is :

$$\begin{bmatrix} v_{sd} \\ v_{sq} \\ v_0 \end{bmatrix} = \frac{2}{3} \begin{bmatrix} \cos \theta & \cos \left(\theta - \frac{2\pi}{3} \right) & \cos \left(\theta - \frac{2\pi}{3} \right) \\ \sin \theta & \sin \left(\theta - \frac{2\pi}{3} \right) & \sin \left(\theta - \frac{2\pi}{3} \right) \\ \frac{1}{\sqrt{2}} & \frac{1}{\sqrt{2}} & \frac{1}{\sqrt{2}} \end{bmatrix} \begin{bmatrix} v_{sa} \\ v_{sb} \\ v_{sc} \end{bmatrix} \quad (3.29)$$

3.3.2 PMSM Modeling in the d-q Rotating Frame

In the rotating d-q frame, the rotor axis is at an angle θ_r relative to the stationary stator axis, and the stator magnetomotive force (mmf) is at an angle α to the rotor d-axis . Figure. 3.3 illustrates a two-pole PMSM schematic.

The PMSM model without damper windings assumes:

1. Negligible saturation effects.
2. Sinusoidal induced EMF

36 Chapter 3. Modeling and Simulation of PMSM Drive for EV application

3. No eddy current or hysteresis losses.

4. Neglected field current dynamics.

The voltage equations are:

$$\begin{aligned} v_{sq} &= R_s i_{sq} + \omega_r \phi_{sd} + p \phi_{sq} \\ v_{sd} &= R_s i_{sd} - \omega_r \phi_{sq} + p \phi_{sd} \end{aligned} \quad (3.30)$$

Flux linkages are:

$$\begin{aligned} \phi_{sq} &= L_q i_{sq} \\ \phi_{sd} &= L_d i_{sd} + \phi_m \end{aligned} \quad (3.31)$$

Substituting equations (3.30) and (3.31) yields:

$$\begin{aligned} v_{sq} &= R_s i_{sq} + \omega_r (L_d i_{sd} + \phi_m) + p L_q i_{sq} \\ v_{sd} &= R_s i_{sd} - \omega_r L_q i_{sq} + p (L_d i_{sd} + \phi_m) \end{aligned} \quad (3.32)$$

These are arranged as:

$$\begin{bmatrix} v_{sq} \\ v_{sd} \end{bmatrix} = \begin{bmatrix} R_s + p L_q & \omega_r L_d \\ -\omega_r L_q & R_s + p L_d \end{bmatrix} \begin{bmatrix} i_{sq} \\ i_{sd} \end{bmatrix} + \begin{bmatrix} \omega_r \phi_m \\ p \phi_m \end{bmatrix} \quad (3.33)$$

The motor torque is:

$$T_e = \frac{3}{2} \left(\frac{p}{2} \right) (\phi_{sd} i_{sq} - \phi_{sq} i_{sd}) \quad (3.34)$$

The mechanical torque equation is:

$$T_e = T_l + B \omega_m + J \frac{d\omega_m}{dt} \quad (3.35)$$

The rotor mechanical speed is:

$$\begin{aligned} \omega_m &= \int \left(\frac{T_e - T_l - B \omega_m}{J} \right) dt \\ \omega_m &= \frac{2}{p} \omega_r \end{aligned} \quad (3.36)$$

3.4. Field-Oriented Control (FOC) for PMSM Speed Regulation

37

3.3.3 PMSM Equivalent Circuit

Figure. 3.4 shows the equivalent circuit of PMSM. The d-q model-derived

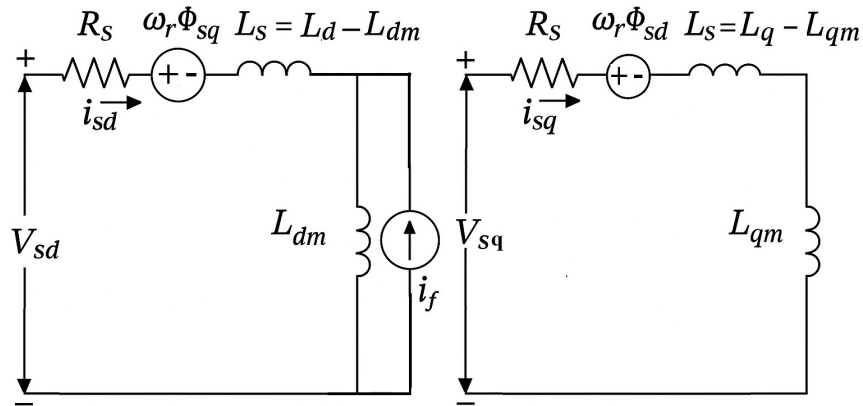


FIGURE 3.4: PMSM Equivalent Circuit

equivalent circuit uses stator voltages, with the d-axis rotor flux represented as a constant source

$$\phi_m = L_d i_f \quad (3.37)$$

3.4 Field-Oriented Control (FOC) for PMSM Speed Regulation

Applications such as robotics and industrial automation require precise speed and position control. The PMSM drive system integrates a speed reference, inverter, feedback mechanism, rotor, and controller. FOC regulates torque and flux independently. The stator currents are:

$$\begin{aligned} I_a &= I_0 \sin(\omega t + \alpha) \\ I_b &= I_0 \sin\left(\omega t + \alpha - \frac{2\pi}{3}\right) \\ I_c &= I_0 \sin\left(\omega t + \alpha + \frac{2\pi}{3}\right) \end{aligned} \quad (3.38)$$

38 Chapter 3. Modeling and Simulation of PMSM Drive for EV application

The magnetic field is:

$$\begin{bmatrix} K_\alpha \\ K_\beta \\ K_0 \end{bmatrix} = \begin{bmatrix} \sin(\omega t + \alpha) \\ \sin(\omega t + \alpha - \frac{2\pi}{3}) \\ \sin(\omega t + \alpha + \frac{2\pi}{3}) \end{bmatrix} [K_1] \quad (3.39)$$

Using Park's transformation, stator currents are converted to d-q components, maintaining a fixed angle between rotor field and stator currents:

$$\begin{bmatrix} i_d \\ i_q \end{bmatrix} = i_s \begin{bmatrix} \sin \alpha \\ \cos \alpha \end{bmatrix} \quad (3.40)$$

The electromagnetic torque, derived from equations (3.38),(3.39) and (3.40) is:

$$T_e = \frac{3P}{2} \left[\frac{1}{2}(L_d - L_q)I_s^2 \sin 2\alpha + \phi_m I_s \sin \alpha \right] \quad (3.41)$$

The motor torque depends on rotor type and d-q inductance differences, with rotor saliency introducing a reluctance torque component.

In high-performance vector-controlled drives, a current-control loop with high bandwidth is essential to (a) ensure accurate current tracking, (b) minimize the transient period, and (c) enable the Voltage Source Inverter (VSI) to function as a current source amplifier within the current loop bandwidth. Figure. 3.5 illustrates the block diagram of a vector-controlled PMSM drive using HCC.

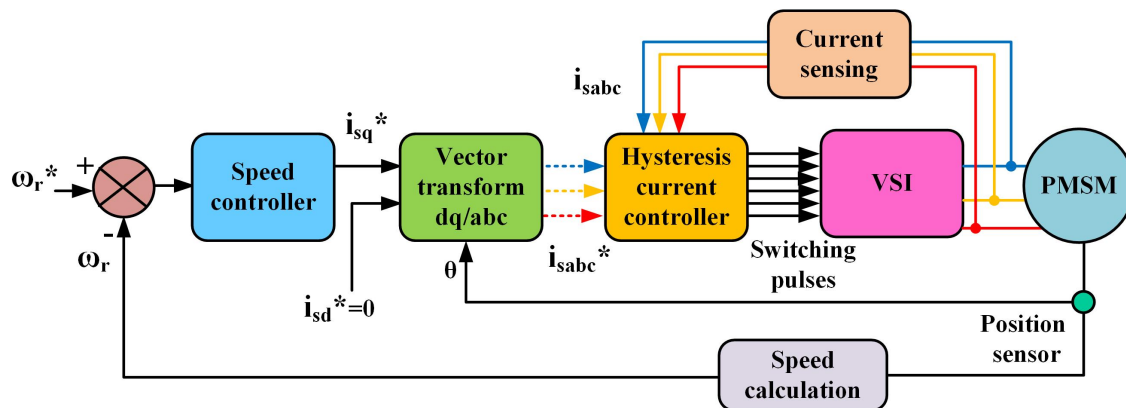


FIGURE 3.5: FOC of PMSM Drive System with HCC

Hysteresis current control (HCC) is employed to achieve near-sinusoidal AC

3.5. Modeling of PMSM-drive for EV applications

39

output current while meeting torque or speed requirements . A hysteresis band controller ensures a regular switching frequency by comparing the actual stator current with the desired reference current of the motor, maintaining low harmonic content in the stator current. The reference currents are generated by the controller with the inverter, constrained within a range determined by the width of the hysteresis band. The error between the desired currents (i_{sa}^* , i_{sb}^* , or i_{sc}^*) and the measured currents (i_{sa} , i_{sb} , i_{sc}) is fed to a comparator with a hysteresis band. When the error exceeds the upper limit, a HIGH signal (i.e., '1') is generated, and when it falls below the lower limit, a LOW signal (i.e., '0') is produced. This controller does not have a fixed switching frequency, which varies continuously with the bandwidth. The speed controller calculates the error between the reference speed (ω^*) and the actual speed (ω_r), which is processed by a PI controller. Position feedback is obtained via a position encoder mounted on the motor shaft.

3.5 Modeling of PMSM-drive for EV applications

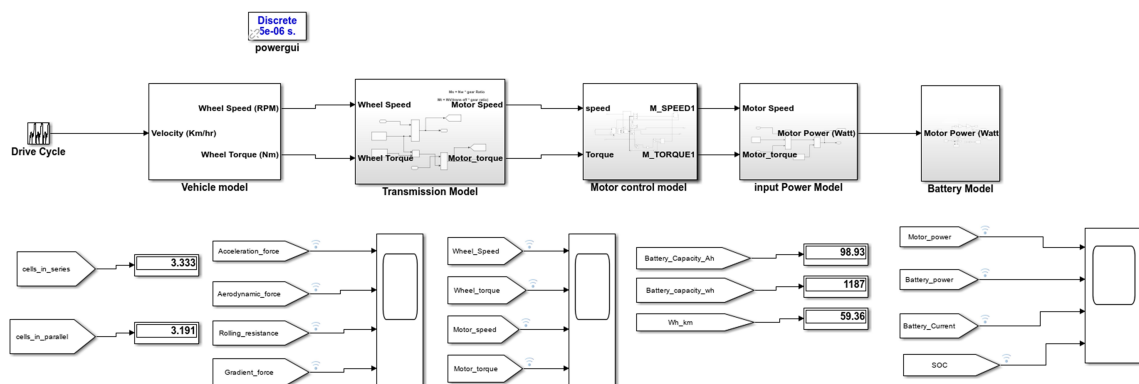


FIGURE 3.6: Simulink model of PMSM-based EV drivetrain

The modeling and simulation of an EV drivetrain with a PMSM provide a comprehensive framework to evaluate vehicle performance, energy efficiency, and control strategies under realistic conditions. This analysis, conducted in MATLAB/Simulink using the IM240 drive cycle (as shown in Figure. 3.6), focuses on the key components of the EV drivetrain: the PMSM, battery system,

40 Chapter 3. Modeling and Simulation of PMSM Drive for EV application

transmission, and their integration. The following subsections detail each component's model, the simulation results, and their implications for EV design.

TABLE 3.2: PMSM Parameters

| Parameter | Symbol | Value | Unit |
|-------------------|------------|-------|------------------------------|
| Stall Torque | T_s | 11 | Nm |
| Peak Torque | T | 33 | Nm |
| Rated Speed | ω_r | 3000 | rpm |
| Rated Voltage | V | 380 | V |
| Number of Poles | P_n | 6 | – |
| Stator Resistance | R | 0.95 | ohm |
| Rated Current | I | 6.8 | A |
| Inductance | L_s | 8.2 | mH |
| Inertia | J | 0.015 | $\text{kg} \cdot \text{m}^2$ |

The PMSM is a cornerstone of the EV drivetrain due to its high efficiency (typically exceeding 90%), compact design, and excellent torque characteristics at low speeds, making it ideal for urban driving scenarios. The PMSM model captures its electrical and mechanical behavior accurately, enabling precise control during dynamic operations. PMSM parameters used in this study are shown in Table 3.2. It delivers torque efficiently during acceleration, achieving a maximum torque of 8 Nm at 2500 rpm (as shown in Figure 3.9), and supports energy recovery through regenerative braking, where it functions as a generator, enhancing overall energy efficiency.

Although the motor only outputs 11 Nm, the gearbox multiplies this torque by 4.5, and the wheel radius reduces the torque-to-force conversion factor. This is how a modest-torque motor can generate sufficient tractive force for acceleration, such as the observed 94 N peak in the simulation results. .

3.5.1 Battery Model

The battery model, based on a lithium-ion battery with a nominal voltage of 48 V and a capacity of 3 Ah, powers the drivetrain and accounts for power delivery, current draw, and state of charge (SOC) dynamics. The battery power is derived

3.5. Modeling of PMSM-drive for EV applications

41

from the motor power using the relation

$$P_{\text{battery}} = \frac{P_{\text{motor}}}{\eta_{\text{inverter}}},$$

where η_{inverter} (set to 0.95) represents the inverter efficiency. The battery current is calculated as

$$I_{\text{battery}} = \frac{P_{\text{battery}}}{V_{\text{battery}}},$$

where V_{battery} is the battery voltage. The SOC is determined by integrating the current over time:

$$\text{SOC}(t) = \text{SOC}(0) - \frac{1}{C_{\text{battery}}} \int_0^t I_{\text{battery}}(\tau) d\tau,$$

where C_{battery} is the battery capacity. This model captures the battery's dynamic response, showing a gradual SOC decline from 92% to 35% over the 250 second IM240 drive cycle (Figure. 3.8), reflecting realistic energy consumption patterns. The battery power peaks at 20 W, and the current reaches up to 0.42 A.

3.5.2 Transmission Model

The transmission model converts motor speed and torque to wheel speed and torque, using a gear ratio of 4.5 and a transmission efficiency of 0.95. The wheel speed (ω_w) is related to the motor speed (ω_m) as

$$\omega_w = \frac{\omega_m}{G},$$

and the wheel torque (T_w) is given by

$$T_w = T_m G \eta_{\text{trans}}.$$

This ensures efficient mechanical energy transfer to the wheels, accurately reflecting vehicle speeds, such as a reduction from 40 km/h to 32.3 km/h during braking scenarios, and wheel speeds up to 400 rpm (Figure. 3.9).

42 Chapter 3. Modeling and Simulation of PMSM Drive for EV application

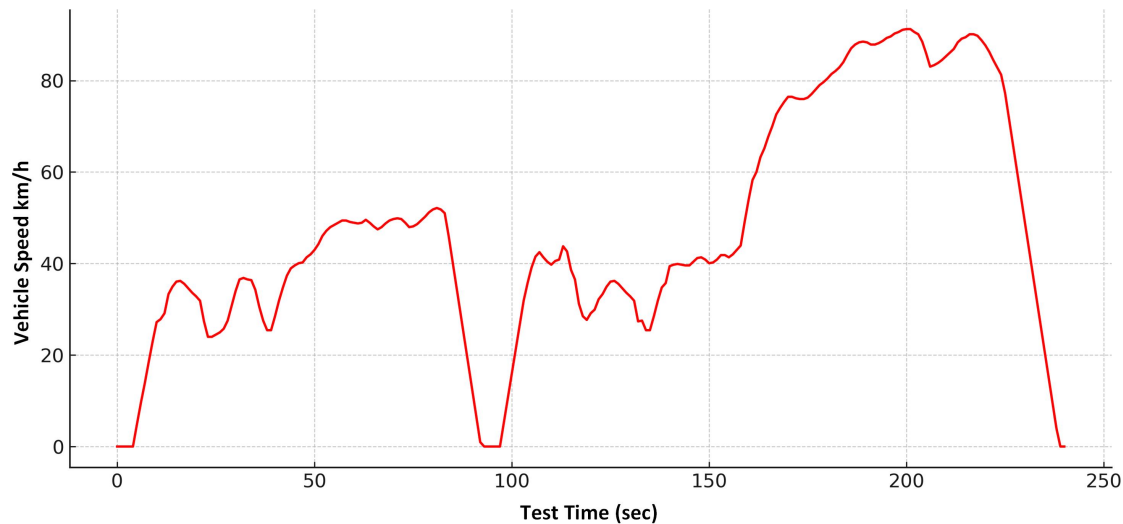


FIGURE 3.7: Inspection and Maintenance (IM240) driving cycle

3.5.3 Simulation Results under IM240 Drive Cycle

The "The Inspection and Maintenance (IM240) driving cycle shown in Figure 3.7 is a 240-second standardized test simulating a 3.1-kilometer urban route, characterized by a peak speed of 91.2 km/h and an average speed of 47.3 km/h [88]. It evaluates the drivetrain's performance through diverse operational stages such as idling, steady cruising, acceleration, and braking. The simulation results validate the model's robustness, with the motor speed closely tracking the reference speed (Figure. 3.9). Additionally, the motor and battery power align with operational demands, as shown in Figure. 3.8, demonstrating the system's capability to handle dynamic conditions. The drivetrain achieves accelerations of 2 m/s^2 , corresponding to acceleration force peaks of 94 N, and decelerations of 1.925 m/s^2 . The forces acting on the vehicle during the IM240 drive cycle include acceleration force, aerodynamic force, rolling resistance force, and gradient force. The acceleration force peaks at 94 N, reflecting the vehicle's dynamic response to acceleration demands. The aerodynamic force reaches 90 N, influenced by the vehicle's speed and air resistance. Rolling resistance remains constant at 12 N, accounting for tire friction, while the gradient force is negligible due to the flat terrain assumed in the simulation. These forces, illustrated in Figure. 3.10, provide insight into the mechanical challenges faced by the drivetrain during operation.

3.5. Modeling of PMSM-drive for EV applications

43

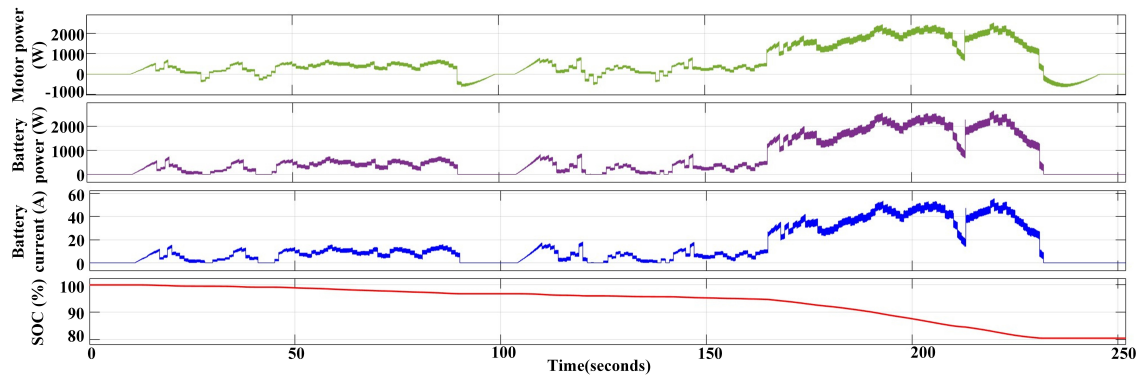


FIGURE 3.8: Simulation results of a PMSM-based EV drivetrain under IM 240 drive cycle, illustrating Motor power, Battery power, Battery current and state of charge(SoC)

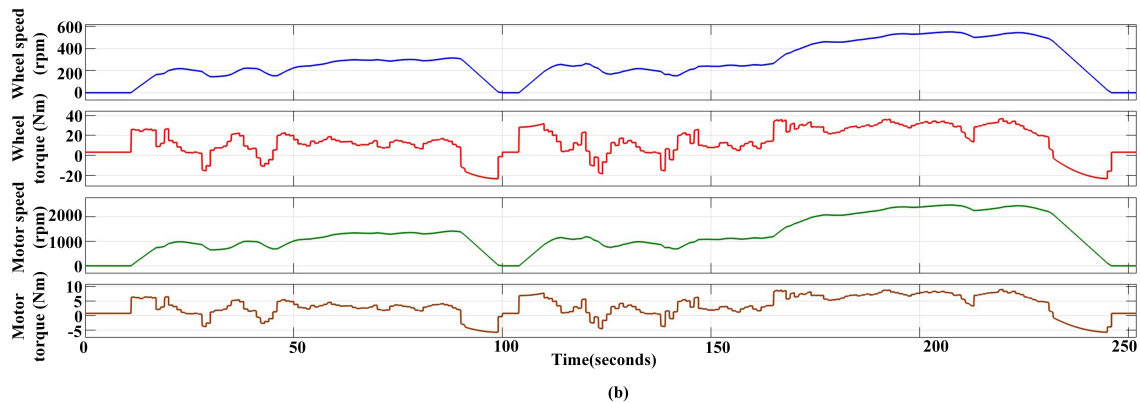


FIGURE 3.9: Simulation results of a PMSM-based EV drivetrain under IM 240 drive cycle, illustrating Wheel speed, Wheel torque, Motor speed and Motor torque

3.5.4 Significance for EV Drivetrain Design

This integrated simulation provides valuable insights into the EV drivetrain's performance, enabling precise calculations for power and transmission requirements. These insights are crucial for selecting appropriate ratings for drivetrain components, such as the motor, inverter, and battery, ensuring alignment between real-world demands and laboratory integration. For instance, the motor rating must deliver sufficient torque and speed to meet the dynamic demands of the drive cycle, supporting efficient acceleration and regenerative braking. The inverter should handle power conversion efficiently, facilitating

44 Chapter 3. Modeling and Simulation of PMSM Drive for EV application

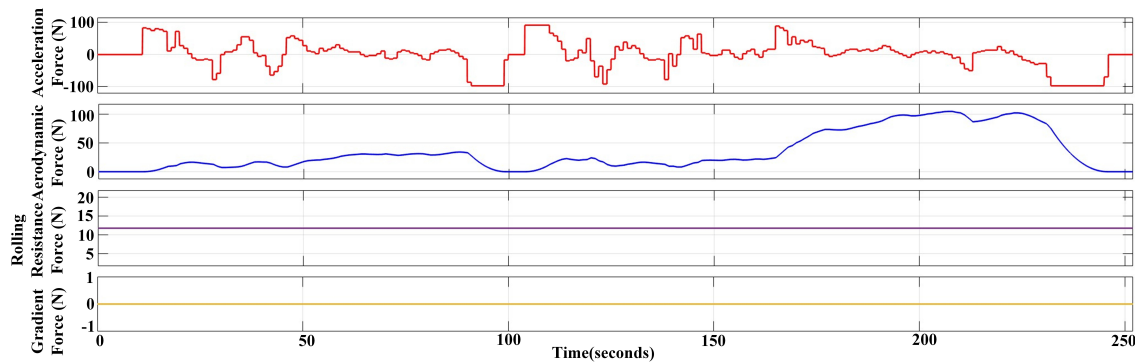


FIGURE 3.10: Simulation results of a PMSM-based EV drivetrain under IM 240 drive cycle, illustrating Acceleration force, Aerodynamic force, Rolling resistance force, and Gradient force

energy transfer between the battery and motor under varying loads. Similarly, the battery rating must sustain the required current and maintain a stable state of charge throughout the drive cycle, ensuring reliable performance across diverse operating conditions.

3.6 Conclusion

This chapter laid the groundwork for understanding the dynamic behavior of a PMSM-based EV drivetrain through comprehensive system modeling. Using the IM240 drive cycle as a benchmark, the analysis revealed critical insights into power flow, energy consumption, and drivetrain efficiency. These findings guided crucial decisions regarding the specifications of the motor, inverter, and battery, thereby bridging the gap between simulation outcomes and real-world application. To ensure alignment between the modeled system and its practical performance, an experimental hardware setup has been developed, as detailed in the following chapter.

Chapter 4

Design and Development of PMSM Drive Train

4.1 Introduction

This chapter presents the design and implementation of a laboratory prototype for a PMSM drive system, tailored for electric vehicle applications and research purposes. The prototype integrates advanced control, power, and measurement systems to achieve precise motor control and performance evaluation. Key components, including the dSPACE DS1104 controller, a three-phase Voltage Source Inverter (VSI), and various sensors, are interfaced using MATLAB and SIMULINK. The following sections detail the system's design, components, experimental setup, and measurement techniques.

4.2 PMSM Drive System Overview

The laboratory prototype is designed to operate a 380 V, 3.4 kW, 6-pole PMSM at a rated speed of 3000 rpm. The system's architecture is illustrated in Figure. 4.1, which shows the schematic layout, and Figure. 4.2, which depicts the physical laboratory setup. These figures provide a comprehensive view of the system's design and implementation.

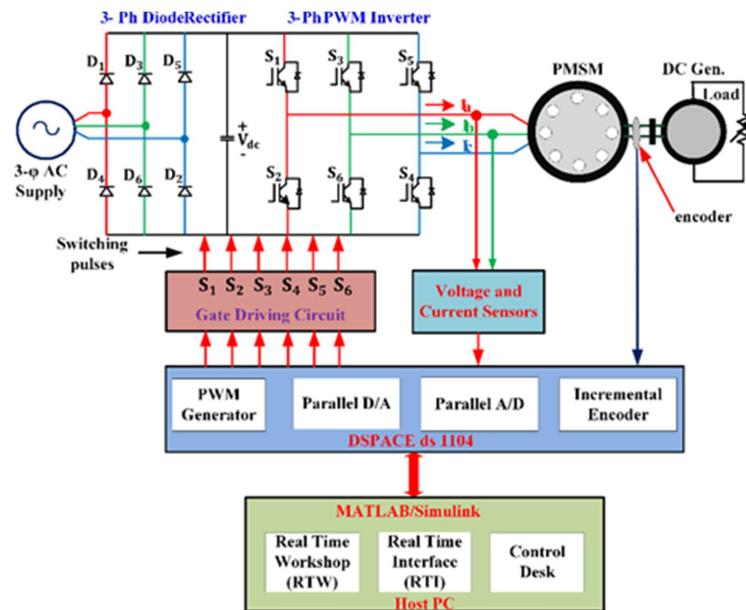


FIGURE 4.1: Schematic Layout of the PMSM Drive System

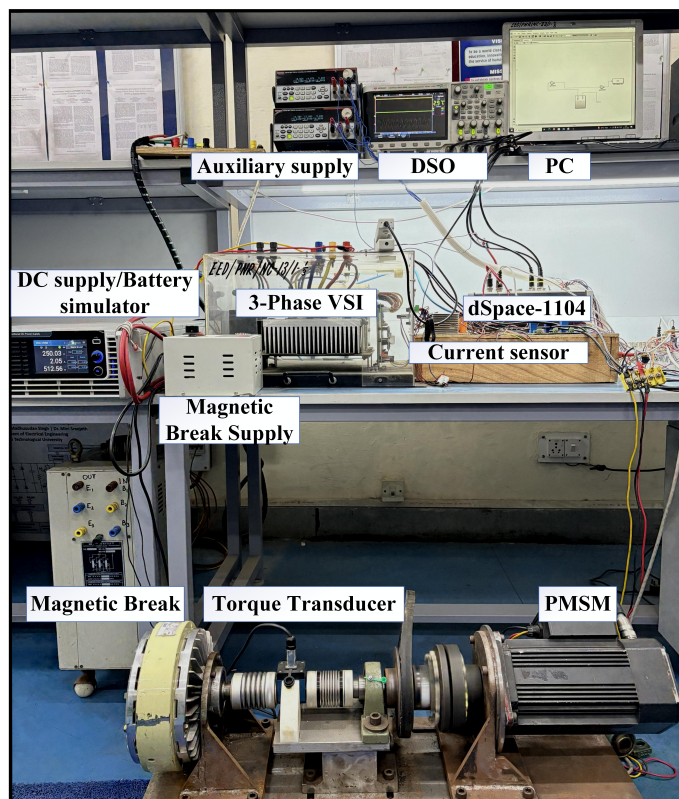


FIGURE 4.2: Laboratory Prototype of the PMSM Drive System

4.3. Controller Design

47

4.2.1 Motor Specifications

section The PMSM is the core component of the drive system, chosen for its high efficiency, compact design, and suitability for electric vehicle applications. Table. 3.2 summarizes the motor's key parameters, which underpin its performance in the prototype.

The PMSM operates at 380 V, delivering 3.4 kW with a 6-pole configuration, enabling a rated speed of 3000 rpm. Its high torque density (stall torque of 11 Nm, peak torque of 33 Nm), low stator resistance (0.95 ohm), and inductance (8.2 mH) ensure efficient power conversion. The low inertia (0.015 kg·m²) supports rapid dynamic response, critical for automotive applications. The motor's performance is optimized using precise control algorithms implemented via the dSPACE DS1104 controller.

4.2.2 Loading System

A magnetic powder brake, shown in Figure. 4.3, is integrated into the PMSM drive train to apply controlled loading for performance testing. By varying the electromagnetic coil current, the brake adjusts magnetic field strength, enabling precise torque control from 0 N m to 50 N m without physical contact. Its compact design and adaptability to dynamic load variations make it ideal for simulating real-world conditions, such as acceleration and deceleration in EV .

4.3 Controller Design

The dSPACE DS1104 R&D controller board serves as the central processing unit for the PMSM drive system, enabling high-speed multivariable control and real-time simulation for Rapid Control Prototyping (RCP). Figure. 4.4 illustrates the DS1104 controller setup.

4.3.1 Hardware Configuration

The DS1104 controller board, designed for cost-sensitive RCP applications, is installed in a computer's PCI port. It features a 250 MHz 603 PowerPC floating-point processor and a TMS320F240 DSP-based slave subsystem for



FIGURE 4.3: Magnetic Powder Brake



FIGURE 4.4: dSPACE DS1104 Controller Setup

advanced I/O operations. The board includes dedicated connectors for interfacing with sensors and actuators, with eight Analog-to-Digital Converter (ADC) channels for measuring input voltages and motor phase currents, and six master bit I/O channels for generating gating signals for the IGBT-based

4.3. Controller Design

49

inverter. In a balanced three-phase system, only two phase currents are sensed, and the third is calculated to minimize sensor requirements. Table 4.1 summarizes the key specifications of the DS1104 controller.

TABLE 4.1: Parameters of dSPACE DS1104 Controller Board

| Component | Specifications |
|-----------------------------|---|
| Processor | |
| - CPU | 250 MHz, MPC8240 with PPC603e core |
| - PCI Bridge | 33 MHz on-chip |
| - Processor Type | Floating-point |
| - On-chip Cache | 2×16 KB |
| - Peripherals | On-chip peripherals |
| Interrupt Controller | |
| - Encoder Interrupts | Two incremental encoder index line interrupts |
| - PWM Interrupt | One slave DSP PWM interrupt |
| - UART Interrupt | One UART interrupt |
| - Timer Interrupts | Five timer interrupts |
| - Slave DSP Interrupt | One slave DSP interrupt |
| - Host Interrupt | One host interrupt |
| - ADC Interrupts | Five ADC end-of-conversion interrupts |

4.3.2 Software Integration

The DS1104 leverages a software ecosystem comprising MATLAB, SIMULINK, Real-Time Workshop (RTW), Real-Time Interface (RTI), and ControlDesk. These tools facilitate the development, simulation, and deployment of control algorithms:

1. **MATLAB:** Provides over 600 mathematical functions for modeling and simulation, supporting system design and analysis.
2. **Simulink:** Enables block-diagram-based modeling of linear, nonlinear, and hybrid systems.
3. **RTW:** Generates C or ADA code from Simulink models for real-time implementation.

4. **RTI**: Integrates Simulink models with DS1104 hardware, providing libraries for I/O interfacing and optimized code generation.
5. **ControlDesk**: Supports real-time parameter tuning, signal visualization, data acquisition, and automation.

Figure. 4.5 illustrates the software integration workflow. Simulink models incorporate RTI blocks (e.g., ADC and master bit I/O) to link with DS1104 hardware, enabling automatic code generation via RTW and RTI, thus eliminating manual code conversion.

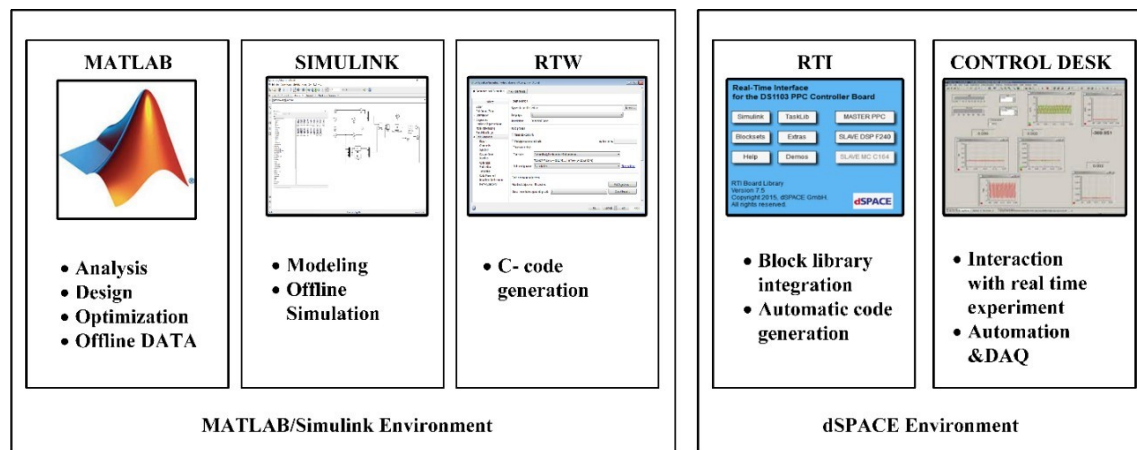


FIGURE 4.5: Software Integration Workflow for dSPACE DS1104

4.3.3 System Integration

The dSPACE DS1104 integrates hardware and software to enable RCP, as shown in the block diagram in Figure. 4.1. The controller receives sensor inputs (e.g., voltage and current) via ADC channels, processes them using Simulink models with RTI blocks, and outputs gating signals to the IGBT-based inverter via master bit I/O channels. This setup ensures precise control of the PMSM drive.

4.4 Power Supply and Inverter System

For PMSM drive train development, the power electronics system integrates a bidirectional DC power supply and a compact inverter unit. The DC power

4.4. Power Supply and Inverter System

51

supply enables controlled energy input and regeneration during braking, while the 3-phase IGBT-based inverter converts DC to AC for motor operation. Together, they support voltage and current control modes, ensure efficient energy flow, and enable reliable testing and validation of PMSM performance under dynamic conditions. This setup is essential for implementing and evaluating advanced motor control strategies using platforms like dSPACE, STM32, or DSP.

4.4.1 Bidirectional Power Supply

The Chroma 62000D Series bidirectional DC power supply, shown in Figure. 4.6, serves as both a power source and regenerative load, simulating battery behavior for electric vehicle component testing. It supports EV batteries from 12 V to 800 V, enabling testing of bidirectional chargers, power systems, and motor drivers without physical batteries. The supply features a fast response time (<1.5 ms), 100 programmable sequences, and compliance with EV testing standards (LV123/LV148). Its Charge-Discharge mode evaluates battery capacity and electrical properties, while its compact design enhances energy efficiency.



FIGURE 4.6: Bidirectional DC Power Supply

4.4.2 Inverter and Driver Circuit

The three-phase PMSM drive system, depicted in Figure. 4.2, uses a DC voltage input (e.g., from a battery or rectified DC) stabilized by a DC link capacitor to supply a three-phase Voltage Source Inverter (VSI). The VSI, configured with six

23

TABLE 4.2: Specifications of the Electrical Load System

| Parameter | Specification |
|--------------------|---|
| Voltage Rating | 0–600V |
| Power Rating | 18 kW |
| Load Functions | CC, CP, CR (for battery simulation) |
| Transient Response | < 1.5 ms for -90% to +90% load change |
| Input Power | 3-phase 4-wire, 200–480 Vac |
| Built-in Functions | Battery simulation, charge–discharge mode |

IGBTs in a three-leg topology, converts DC to three-phase AC for the PMSM. Interfacing inductors, designed based on the PMSM's rated current and VSI switching frequency (5–20 kHz), ensure smooth current flow and reduced harmonics. The dSPACE DS1104 processes feedback signals (rotor position, motor currents, DC bus voltage) to generate six gating pulses using Space Vector Pulse Width Modulation (SVPWM) and field-oriented control (FOC) for precise torque and speed regulation. Performance variables, including voltages and currents, are measured using LEM sensors and recorded by a Digital Storage Oscilloscope (DSO).

IGBT Switch Ratings

TABLE 4.3: IGBT specifications

| Parameter | Specifications |
|---|---|
| Type | IGBT Module |
| Manufacturer | Semikron |
| Configuration | Half Bridge |
| Collector-Emitter Voltage (VCES) | 1200 V |
| Nominal Collector Current ($I_{C_{nom}}$) | 150 A |
| Continuous Collector Current (IC) @ 25°C | 231 A |
| Operating Temperature Range | –40°C to +175°C |
| Key Features | High current density, low saturation loss |

The VSI employs SKM150GB12V IGBT modules, selected for their low on-state voltage drop, high voltage capability, and smooth switching characteristics. Figure. 4.7 illustrates the IGBT switch leg and schematic. Three

4.5. Measurement System

53

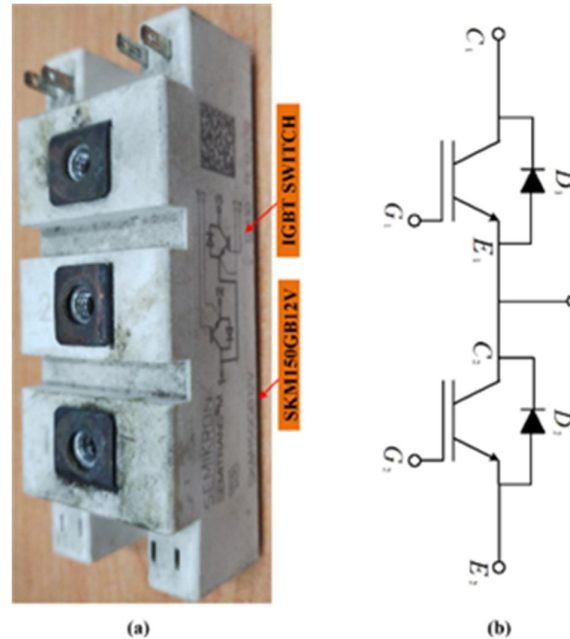


FIGURE 4.7: Insulated Gate Bipolar Transistor (IGBT) Module

modules are used to drive the PMSM, with specifications including a collector-emitter voltage (V_{CE}) of 1200 V, collector current (I_C) of 150 A, maximum switching frequency (f_s) of 20 kHz, gate-emitter voltage (V_{GE}) of 15 V, and operating temperature range of -40°C . to 150°C . These ensure reliable performance under dynamic load conditions.

Gate Driver Circuit

The inverter's IGBT-based power module (1200 V, 25 A) receives gating pulses from the dSPACE DS1104 via an isolated gate driver circuit using opto-coupler ICs (e.g., 6N136/6N137/6N139). The controller generates 5 V pulses, amplified to 15 V to meet IGBT switching requirements. Figure. 4.8 shows the amplifier and isolation circuit's diagram and PCB design.

4.5 Measurement System

Accurate measurement of parameters like input AC voltage, stator currents, rotor position, torque, and speed is essential for closed-loop operation. The

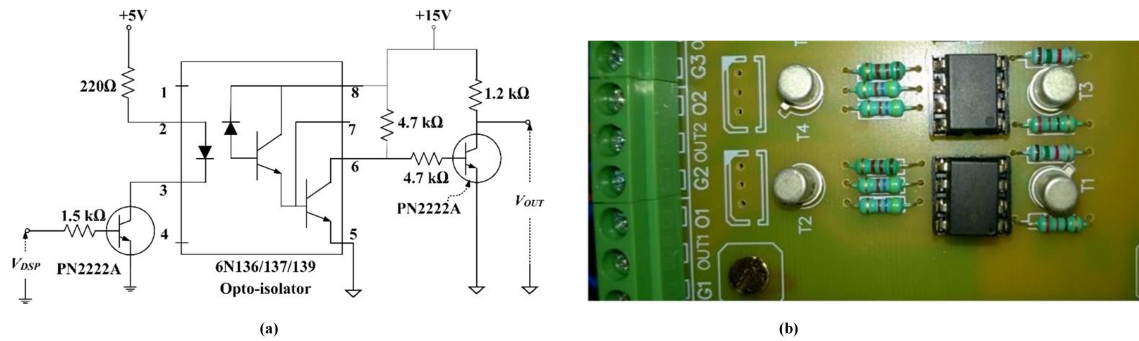


FIGURE 4.8: Gate Driver Circuit

measurement system uses Hall-effect sensors and isolation amplifiers to ensure precision, galvanic isolation, and linear response.

4.5.1 Voltage Measurement

Three LEM LV-20-P Hall-effect sensors measure the three-phase input voltages from the inverter to the PMSM. The sensor output current, proportional to the input voltage, is converted to an equivalent voltage via a measuring resistance, limited to 10 V by an op-amp-based signal conditioning circuit to match the dSPACE ADC voltage limits. Figure. 4.9 shows the voltage sensor circuit and PCB.

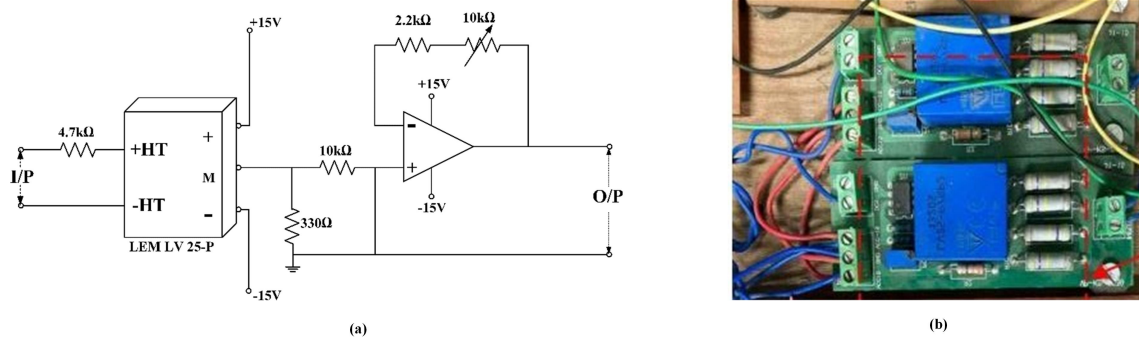


FIGURE 4.9: Voltage Sensor Circuit

4.5. Measurement System

55

4.5.2 Current Measurement

Stator currents are measured using LEM LA 55-P Hall-effect current sensors, which offer excellent accuracy, linearity, wide frequency bandwidth, and galvanic isolation. The sensor output current is proportional to the input, processed by the circuit shown in Figure. 4.10.

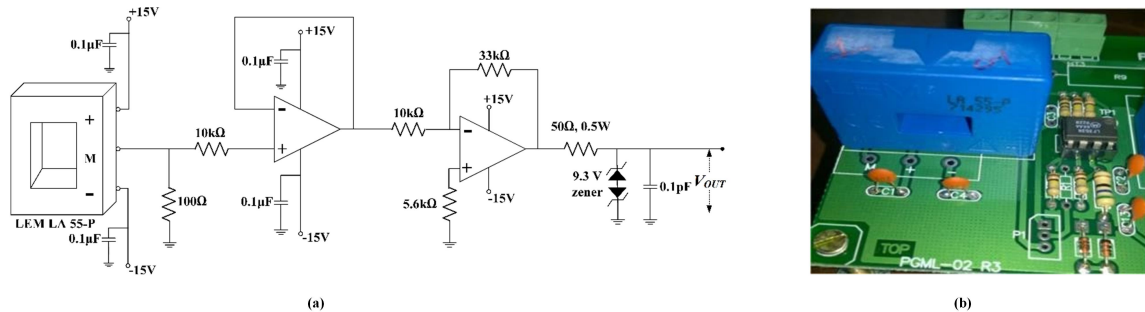


FIGURE 4.10: Current Sensor Circuit

4.5.3 Torque Measurement

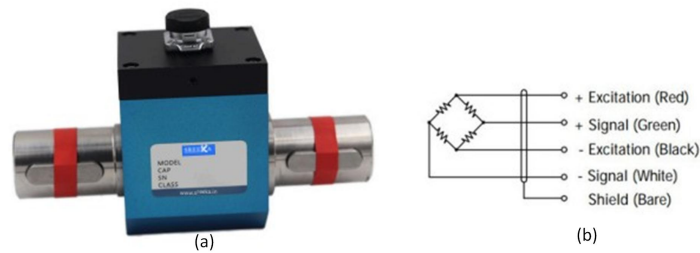


FIGURE 4.11: Torque Transducer

A torque transducer, integrated between the PMSM shaft and load, measures mechanical torque using strain gauges in a Wheatstone bridge configuration, as shown in Figure. 4.11. The amplified and conditioned signal provides precise torque values in N m, critical for validating motor performance and optimizing control strategies.

TABLE 4.4: Torque Transducer Specifications

| Feature | Typical Values |
|-------------------|-----------------------------------|
| Torque Range | 0–50 Nm |
| Accuracy | $< \pm 0.5\%$ |
| Non-Linearity | $< \pm 0.5\%$ |
| Hysteresis | $< \pm 0.1\%$ |
| Non-Repeatability | $< \pm 0.1\%$ |
| Rotational Speed | Up to 4000 RPM |
| Output Signal | $\pm 5\text{Vdc}$, 4–20mA, RS485 |



FIGURE 4.12: Rotary Encoder

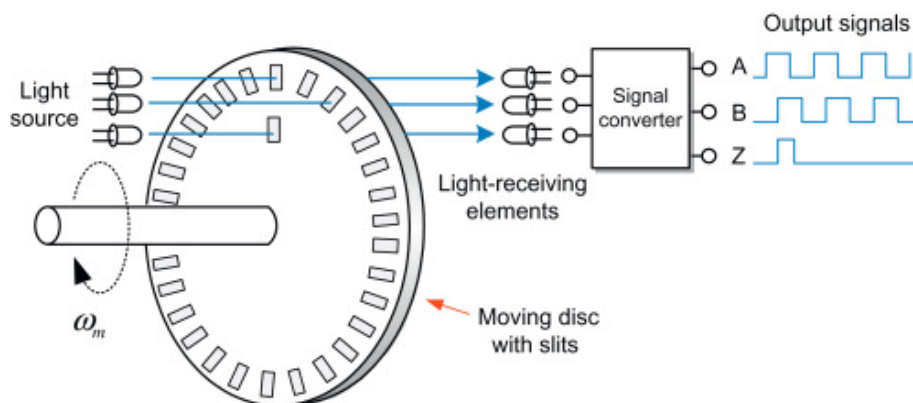


FIGURE 4.13: Construction Principle of Incremental Encoder

4.5. Measurement System

57

4.5.4 Speed and Position Measurement

An incremental optical encoder measures rotor position and speed, producing pulses corresponding to shaft rotation. Figure. 4.12 shows the encoder setup, and Figure. 4.13 illustrates its construction principle. The encoder features a glass rotor disc with alternating transparent and non-transparent zones, modulating a light beam detected by optical sensors [89]. Two channels (A and B), offset by a quarter of the angular step, produce pulses to determine position and rotation direction, while a third channel (Z) provides a reference pulse per revolution. Figure. 4.14 depicts the A, B, and Z output signals.

TABLE 4.5: Autonics 1024 PPR Incremental Rotary Encoder Specifications

| Parameter | Specification |
|-------------------------|--|
| Resolution (PPR) | 1024 pulses per revolution |
| Shaft Diameter | 4 mm |
| Output Signals | Quadrature A, \bar{A} , B, \bar{B} , +Index Z, \bar{Z} |
| Output Type | Line-driver or Totem-pole |
| Supply Voltage | 5VDC $\pm 5\%$ (5–24VDC for some models) |
| Max. Response Frequency | 180–300kHz |
| Max. RPM | Up to 5000rpm |
| Protection Rating | IP50 |
| Operating Temp. Range | –10°C to +70°C |

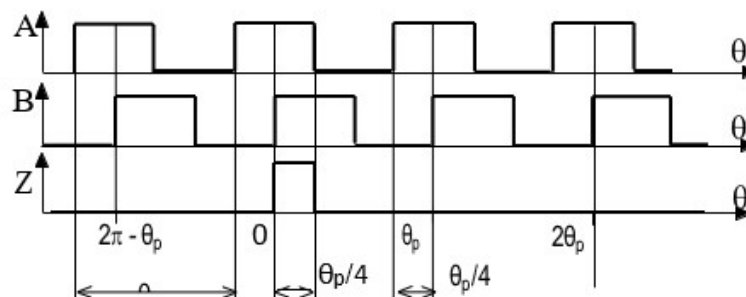


FIGURE 4.14: Output Pulses of Incremental Encoder

The encoder's mathematical model, described by Equations (4.1), defines the A, B, and Z outputs based on the angular position θ and step θ_p :

121

$$\begin{aligned}
 A &= \begin{cases} 1 & \text{if } 0 < |\theta_p(\theta)| < \theta_p/2 \\ 0 & \text{if } \theta_p/2 < |\theta_p(\theta)| < \theta_p \end{cases} \\
 B &= \begin{cases} 1 & \text{if } 0 < |\theta_p(\theta - \theta_p/4)| < \theta_p/2 \\ 0 & \text{if } \theta_p/2 < |\theta_p(\theta - \theta_p/4)| < \theta_p \end{cases} \\
 Z &= \begin{cases} 1 & \text{if } |2\pi(\theta)| = 0 \\ 0 & \text{if } |2\pi(\theta)| \neq 0 \end{cases}
 \end{aligned} \tag{4.1}$$

The number of pulses per rotation, N_r , is given by:

$$N_r = \frac{2\pi}{\theta_p} \tag{4.2}$$

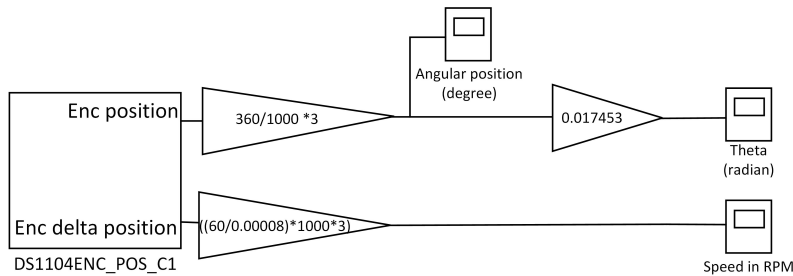


FIGURE 4.15: Decoder Section of Incremental Encoder

The frequency of the encoder's A and B signals, based on angular velocity ω_e , is:

$$f_A = f_B = \frac{\omega_e}{2\pi} N_r \tag{4.3}$$

For an encoder with $N_r = 1000$ pulses/rotation and $\omega_e = 314$ rad/s, the signal frequency is 150 kHz. Figure. 4.16 shows the simulated encoder output pulses, and Figure. 4.15 depicts the decoder section.

The DS1104ENC_POS_C1 block from the RTI library processes quadrature signals A and B, adjusting pulse counts by 0.25 per edge, yielding 1000 counts per revolution for a 1000-slot encoder. The position is calculated with a gain of 360/1000, and speed is derived from the change in pulse counts with a gain of $(60/0.00008) \times 1000$. Figure. 4.17 shows the experimental encoder output pulses. To mitigate noise at low speeds, the average of approximately 10 speed samples is used.

4.6. Conclusion

59

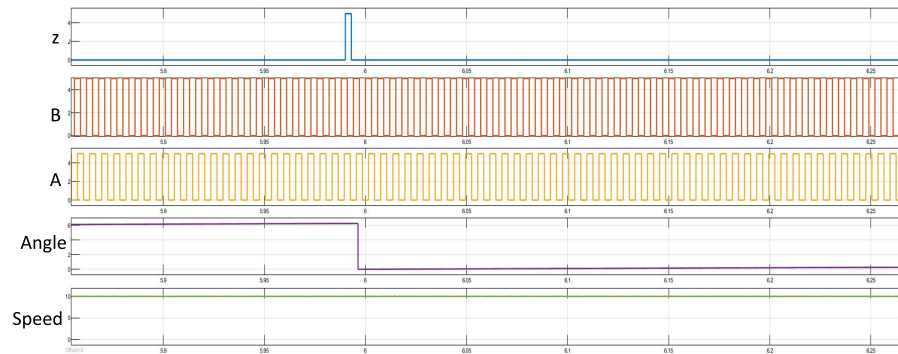


FIGURE 4.16: Simulation Result of Incremental Encoder Output Pulses

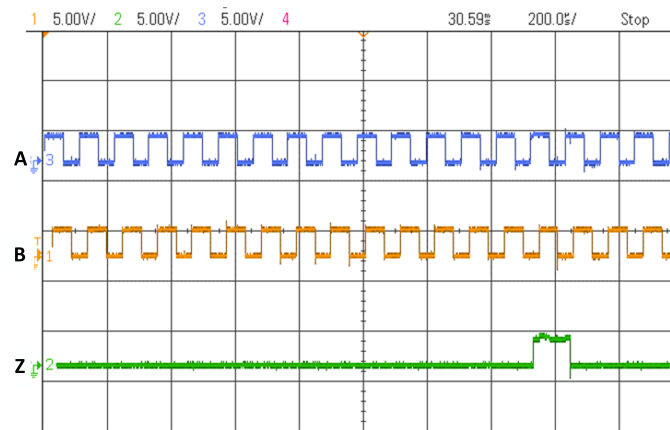


FIGURE 4.17: Experimental Result of Incremental Encoder Output Pulses

4.6 Conclusion

This chapter detailed the design and implementation of a PMSM drive train laboratory prototype, integrating a 3.4 kW, PMSM with a dSPACE DS1104 controller, IGBT-based VSI, and precise measurement systems. The controller's hardware and software ecosystem, including MATLAB, SIMULINK, RTW, RTI, and ControlDesk, enables efficient RCP. The bidirectional power supply, magnetic powder brake, and sensors (current, voltage, torque, and encoder) ensure accurate closed-loop operation for EV and industrial applications. Subsequent chapters will explore the advanced control techniques, including Predictive Control, Hysteresis Control, Sliding Mode Control, and ANFIS, implemented on the DS1104 platform to further optimize PMSM performance.

Chapter 5

Enhancing PMSM Drive Performance for Electric Vehicles through ANFIS-HCC Integration

5.1 Introduction

Electric Vehicles offer a promising solution to reduce automotive pollution by replacing conventional internal combustion engine vehicles, necessitating efficient and reliable motor drives [90]. PMSM drives are preferred in EV applications due to their high power density, precise torque and speed control, and energy efficiency over wide operating ranges [91–93]. However, conventional control methods like PI-based Field-Oriented Control (FOC) struggle with nonlinearities, external disturbances, and modeling inaccuracies in high-performance scenarios [94]. Advanced techniques such as sliding mode control, fuzzy logic, neural networks, adaptive control, and Model Predictive Control (MPC) have been explored to address these challenges [95–107]. Despite their effectiveness, these methods often involve high computational complexity, making real-time implementation challenging [103, 105, 106]. To overcome these limitations, this chapter proposes a novel ANFIS-HCC (Adaptive Neuro-Fuzzy Inference System – Hysteresis Current Control) strategy for FOC of PMSM drives. ANFIS, introduced by Jang in 1993 [108], integrates the learning capabilities of neural networks with fuzzy logic's reasoning, enabling adaptive, nonlinear control with reduced computational overhead compared to MPC and SMC [109, 110]. The ANFIS-HCC controller enhances PMSM drive performance

Chapter 5. Enhancing PMSM Drive Performance for Electric Vehicles through ANFIS-HCC Integration

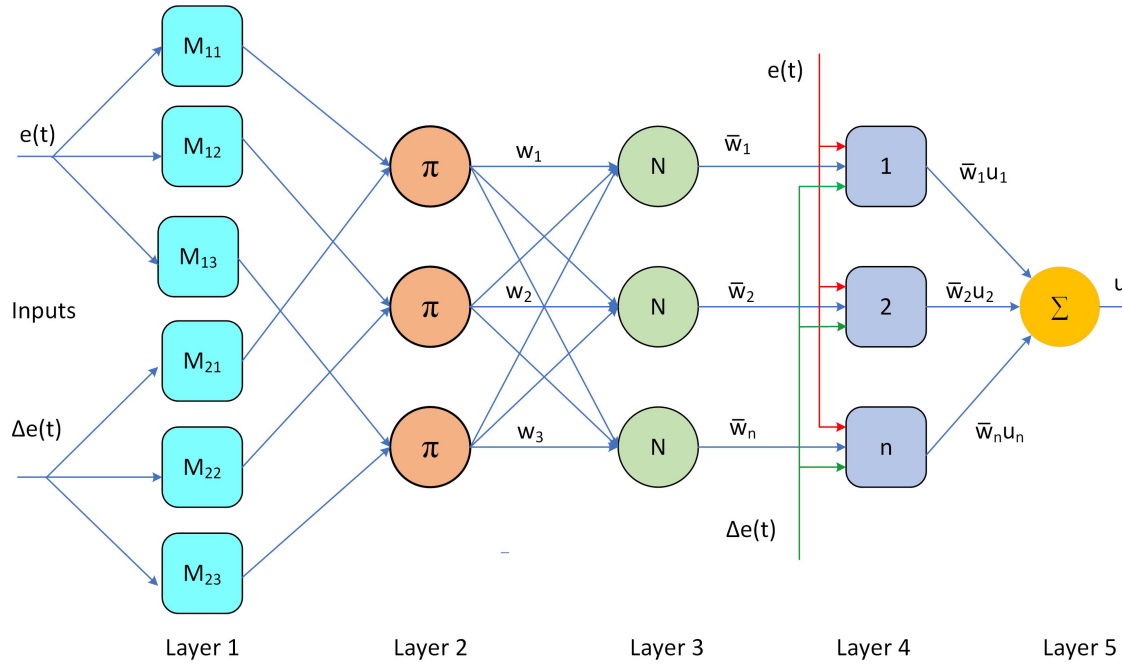


FIGURE 5.1: Block Diagram of ANFIS

by mitigating system nonlinearities and ensuring robust operation under diverse EV operating conditions, validated through simulations and experiments on a dSPACE DS1104 platform.

5.2 Design of ANFIS-HCC Control Strategy for PMSM Drives

The ANFIS model controls the outer loop of the FOC-based PMSM drive, whereas the HCC controls inner current loop, as shown in Figure. 5.3. The control design strategy is elucidated in this section.

5.2.1 Overview of Adaptive Neuro-Fuzzy Inference(ANFIS) System

ANFIS is an ANN that works with the Takagi-Sugeno fuzzy inference system [108]. The technique builds the fuzzy inference system from an input-output pair and an observation data set that has been provided. In the learning phase, the

5.2. Design of ANFIS-HCC Control Strategy for PMSM Drives

63

backpropagation technique is used to modify the membership function's parameters in the designed ANFIS architecture. As shown in Figure. 5.1, the ANFIS structure is divided into five layers. The nodes in Layer 1 are adaptive nodes. Equations (5.1) and (5.2) are used to calculate the fuzzy membership grades of the inputs, indicating the degree of belongingness of each input to their associated fuzzy sets

$$O_{1Ai} = \mu_{Ai}(x), i = 1, 2, 3 \dots n \quad (5.1)$$

$$o_{1Bi} = \mu_{Bi}(y), i = 1, 2, 3 \dots n \quad (5.2)$$

Where x and y are the inputs to node i ; A_i and B_i are the linguistic labels (high, low, etc.) connected to this node function μ . Each fuzzy membership function is adaptable by A_i and B_i , which depends on the least error. A triangular membership function is chosen as the shape with the least amount of error. It is specified by three variables: a and c for the feet and b for the curve tip. The triangular function is expressed as given in (5.3)

$$\text{triangular}(x, a, b, c) = \max \left(\min \left(\frac{x-a}{b-a}, 1, \frac{c-x}{c-b} \right), 0 \right) \quad (5.3)$$

Each node with a label of π corresponds to the firing strength of a fuzzy rule in Layer 2 (inference layer). The output of the Inference Layer is given in (5.4)

$$O_{2,i} = w_i = A_i(x) \times B_i(y), i = 1, 2, 3 \dots n \quad (5.4)$$

The third layer, a normalization layer, normalizes the estimated firing strengths of the previous layer using (5.5).

$$o_{3,i} = \bar{w}_i = \frac{w_i}{\sum_l (w_l)}, i = 1, 2, 3 \dots n \quad (5.5)$$

The nodes in Layer 4, are adaptive. The output of each node in this layer is the product of the normalized firing strength and a first order polynomial (for a first order Sugeno model). The output of this layer is given by (5.6).

$$o_{4,i} = \bar{w}_i f_i = \bar{w}_i (p_i x + q_i y + n_i), i = 1, 2, 3 \dots n \quad (5.6)$$

Chapter 5. Enhancing PMSM Drive Performance for Electric Vehicles through ANFIS-HCC Integration

where f_i is the control signal and (p_i, q_i, r_i) is the consequence parameter set. The output layer calculates the sum of all incoming signals and de-fuzzifies the subsequent set of rules using (5.7)

$$o_{5,i} = \Sigma_i (\bar{w}_i f_i) = \frac{\Sigma_i w_i f_i}{\Sigma_i w_i} \quad i = 1, 2, 3, \dots, n \quad (5.7)$$

TABLE 5.1: Comparative Evaluation of ANFIS Membership Function Types and Configurations

| MF Type | MFs/Input | Fuzzy Rules | Total Parameters | RMSE |
|-------------------|-----------|----------------|------------------------------------|-----------------|
| Triangular | 2 | 4 (2×2) | 16 (12 nonlinear, 4 linear) | 0.0045 |
| Gaussian | 2 | 4 (2×2) | 16 (12 nonlinear, 4 linear) | 0.005 |
| Trapezoidal | 2 | 4 (2×2) | 20 (16 nonlinear, 4 linear) | 0.0055 |
| Triangular | 3 | 9 (3×3) | 27 (18 nonlinear, 9 linear) | 0.003681 |
| Gaussian | 3 | 9 (3×3) | 27 (18 nonlinear, 9 linear) | 0.004 |
| Trapezoidal | 3 | 9 (3×3) | 36 (27 nonlinear, 9 linear) | 0.0043 |
| Triangular | 4 | 16 (4×4) | 48 (32 nonlinear, 16 linear) | 0.0042 |
| Gaussian | 4 | 16 (4×4) | 48 (32 nonlinear, 16 linear) | 0.0048 |
| Trapezoidal | 4 | 16 (4×4) | 64 (48 nonlinear, 16 linear) | 0.005 |

5.2.2 Training and Structure Identification of ANFIS

ANFIS controllers cannot be used until they have been properly trained and tuned. To operate the PMSM and collect the input-output data required for training the newly formed ANFIS controller, a conventional PI-HCC controller was first utilized. The dataset, consisting of 50,001 input-output pairs, was collected from the dSPACE ControlDesk environment under various PMSM drive operating conditions. The two inputs to the ANFIS controller speed error (e) and change in error (Δe) ranged within ± 3500 rpm and ± 5000 rpm/s, respectively. These inputs were normalized to the range $[-1, +1]$ to facilitate stable and efficient training.

To structure the ANFIS model, a grid partitioning method was adopted, assigning three triangular membership functions (MFs) to each input variable. This resulted in a complete rule base of 9 fuzzy rules (3×3 combinations), ensuring full input space coverage. The fuzzy rules were automatically generated, and the output layer of the ANFIS used a first-order Sugeno model.

5.2. Design of ANFIS-HCC Control Strategy for PMSM Drives

65

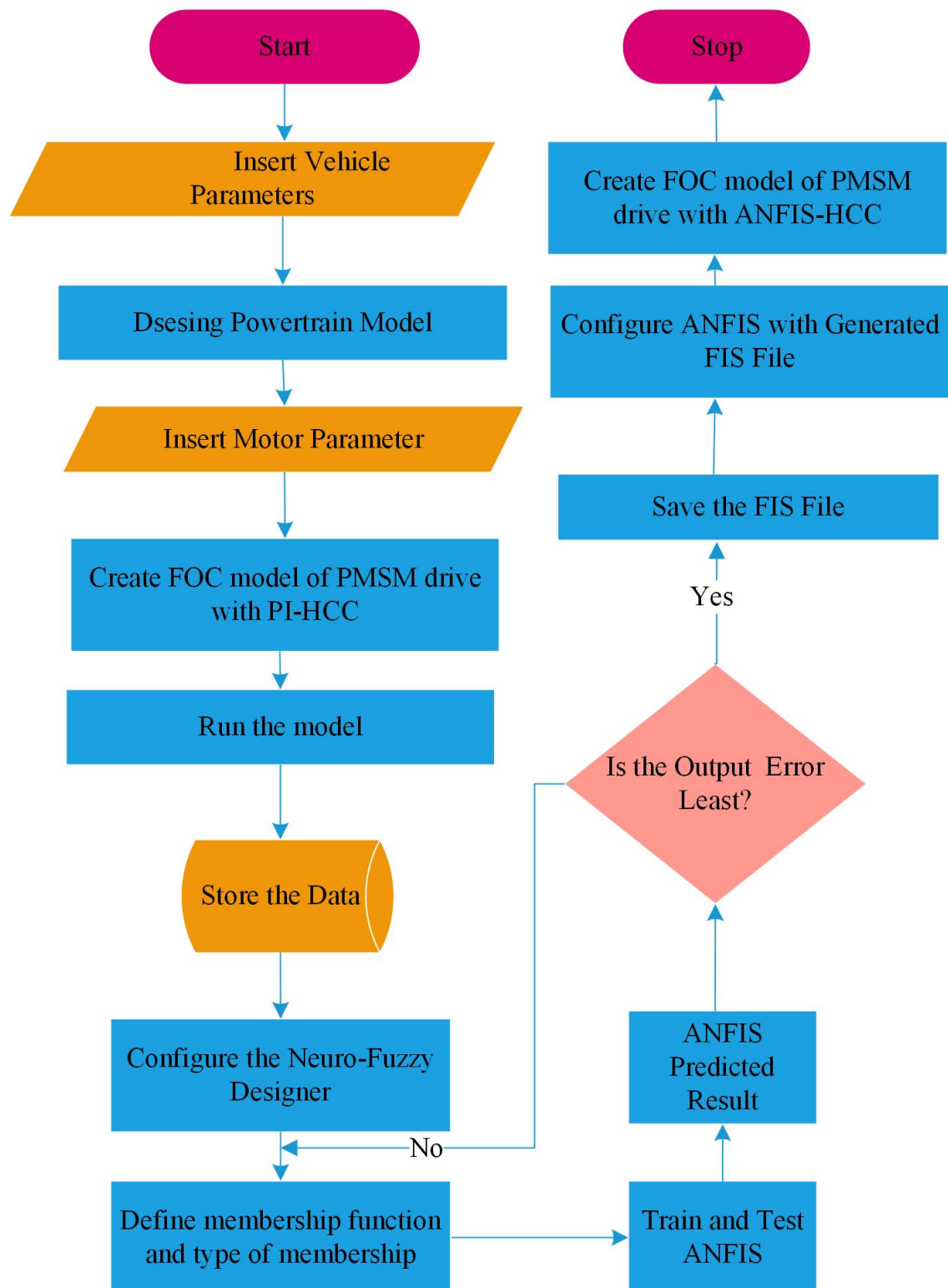


FIGURE 5.2: Flowchart for Training of proposed ANFIS-HCC

Chapter 5. Enhancing PMSM Drive Performance for Electric Vehicles through ANFIS-HCC Integration

The training process used a hybrid learning algorithm, which combined least squares estimation for linear parameter optimization and backpropagation for nonlinear parameter tuning. A total of 50 training epochs were conducted with zero error tolerance specified to maximize accuracy and convergence stability. The flowchart illustrating the training process of the ANFIS-HCC controller is shown in Figure. 5.2.

To determine the most effective MF structure, several MF types (triangular, Gaussian, and trapezoidal) and configurations (2 to 5 MFs per input) were evaluated. Table 5.1 summarizes this comparison. The triangular MF with 3 MFs per input provided the best performance with the lowest RMSE of 0.003681 and moderate computational complexity (27 parameters), and was thus selected for the final implementation.

5.2.3 Hysteresis Current Controller

For high-performance vector-controlled drives, broad current-control loop bandwidths are essential. These bandwidths ensure precise tracking of current and quick transient responses, enabling the Voltage Source Inverter (VSI) to act effectively as a current-generating amplifier within the defined bandwidth. HCC is used to provide a virtually sinusoidal output current when the necessary torque or speed is reached [88]. Using an HCC with a hysteresis band for VSI current control in the inner loop ensures a nearly sinusoidal waveform, which is achieved by comparing the actual stator current, (i_{abc}) to the reference motor current, (i_{abc}^*). Due to the reference current being within a predetermined bandwidth, this also guarantees a low harmonic content in the stator current. The hysteresis band was set to ± 0.1 A, empirically determined to balance current ripple (0.20 A peak-to-peak) and switching frequency (9–11 kHz), ensuring optimal performance and efficiency for the PMSM drive in EV applications. The error in current determines the activation of the appropriate switches of the VSI depending on its value. The switching frequency of the controller is band limited. The ANFIS controller creates the quadrature axis stator current, i_q , in the outer loop based on the difference between the reference speed (ω_r^*) and the actual speed (ω_r). This along with the direct axis stator current, i_d , is converted to i_{abc}^* using park transformation. This reference three-phase current (i_{abc}^*) is

5.2. Design of ANFIS-HCC Control Strategy for PMSM Drives

67

fed along with the measured current (i_{abc}) to the HCC to generate the firing pulse for the VSI to drive the PMSM

5.2.4 Proposed ANFIS-HCC PMSM Drive

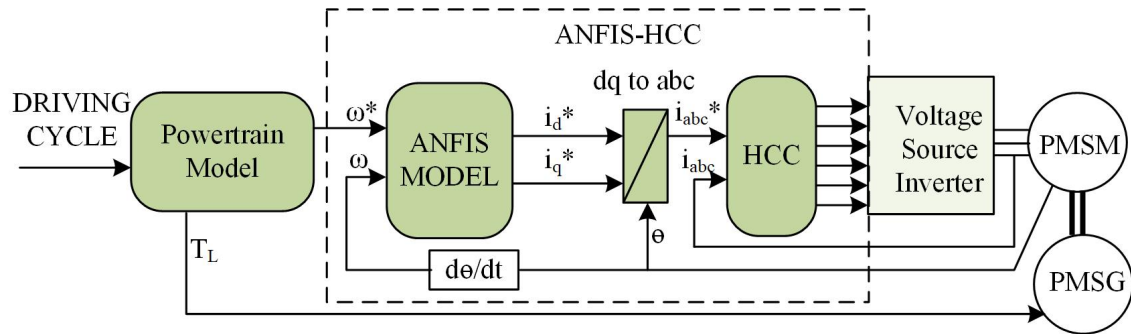


FIGURE 5.3: ANFIS-HCC Control Strategy for PMSM Drives

The proposed ANFIS-HCC strategy for a PMSM drive is illustrated in the block diagram shown in Figure. 5.3. The system begins with a driving cycle input feeding into a powertrain model, which simulates real-world conditions and generates the load torque T_L and rotor speed ω . The ANFIS model, a hybrid neuro-fuzzy controller, takes inputs including the reference speed ω^* , measured rotor speed ω , its time derivative $\frac{d\theta}{dt}$, and the d-q axis currents i_d and i_q . Using these inputs, the ANFIS model adaptively computes the reference currents i_d^* and i_q^* , leveraging its fuzzy inference system trained via neural networks to optimize transient response and minimize current ripple. These reference currents are transformed from the d-q to the abc reference frame using the Park and Clarke transformations, producing i_{abc}^* . The HCC block then compares i_{abc}^* with the actual currents i_{abc} , employing hysteresis bands to generate switching signals for the voltage source inverter. The inverter, in turn, supplies the PMSM, which is coupled to the PMSG (Permanent Magnet Synchronous Generator) with precise voltage and current, ensuring robust torque and speed control. This ANFIS-HCC approach enhances the PMSM drive's dynamic performance by reducing torque ripples, improving current regulation, and achieving higher energy efficiency, making it well-suited for electric vehicle applications under variable operating conditions. Simulations and experiments are performed to validate the proposed theory in a subsequent part of the chapter.

5.3 Simulation studies and Discussion

The proposed ANFIS-HCC controller is developed through simulation studies using MATLAB/Simulink with a sampling time of $5\mu s$. This section presents the comparison of the performance of the FOC based PMSM drive using conventional PI-HCC and the proposed ANFIS-HCC controller under different operating conditions.

The cascaded control system is comprised of two control loops. The outer loop is the speed control loop, while the inner loop is the current control loop. The PI-HCC control structure employs PI and HCC controllers for the outer speed controller loop and the inner-current controller loop, respectively. In contrast, the ANFIS-HCC control scheme uses ANFIS in the speed control loop and HCC in the current control loop. When a motor starts up, it requires a large amount of current to overcome inertia, but this current gradually decreases as the speed reaches a steady state value. The speed responses of the aforesaid two controllers are simulated and analyzed. The starting behaviour of PMSM drive at rated-speed and no-load operation using PI-HCC and proposed ANFIS-HCC are presented in Figure. 5.4. While starting with the reference speed set to 3000 rpm under no-load condition, some distortion and overshoot in electromagnetic torque (T_e), speed (ω_r), and phase-a stator current (i_e) are observed in PI-HCC based controller. However, the ANFIS-HCC based drive gives fast and smooth speed characteristics without overshoot. Figure. 5.5 shows the zoomed-in starting characteristics of the PMSM drive. In addition, the ANFIS-HCC controller has shorter rising and settling time than the PI-HCC controller.

The proposed ANFIS-HCC for FOC of PMSM drive provides a significant reduction in current and torque ripples of PMSM drive in addition to fast and accurate speed tracking in comparison with the conventional PI-HCC-based controller.

5.3. Simulation studies and Discussion

69

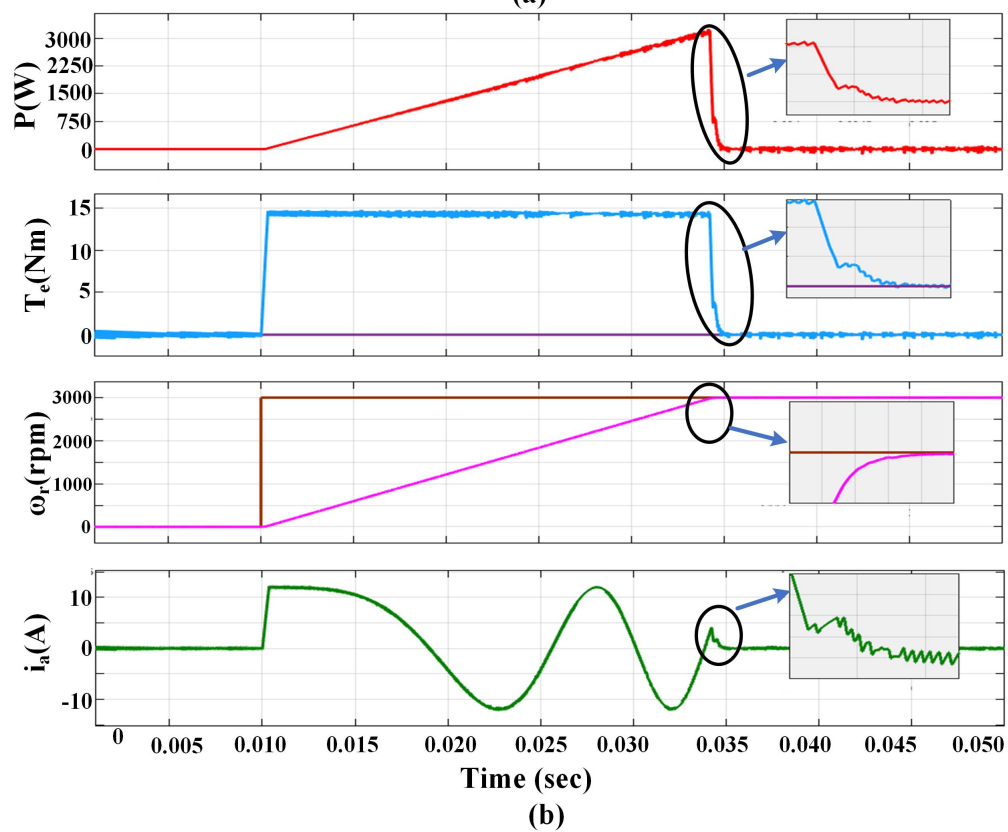
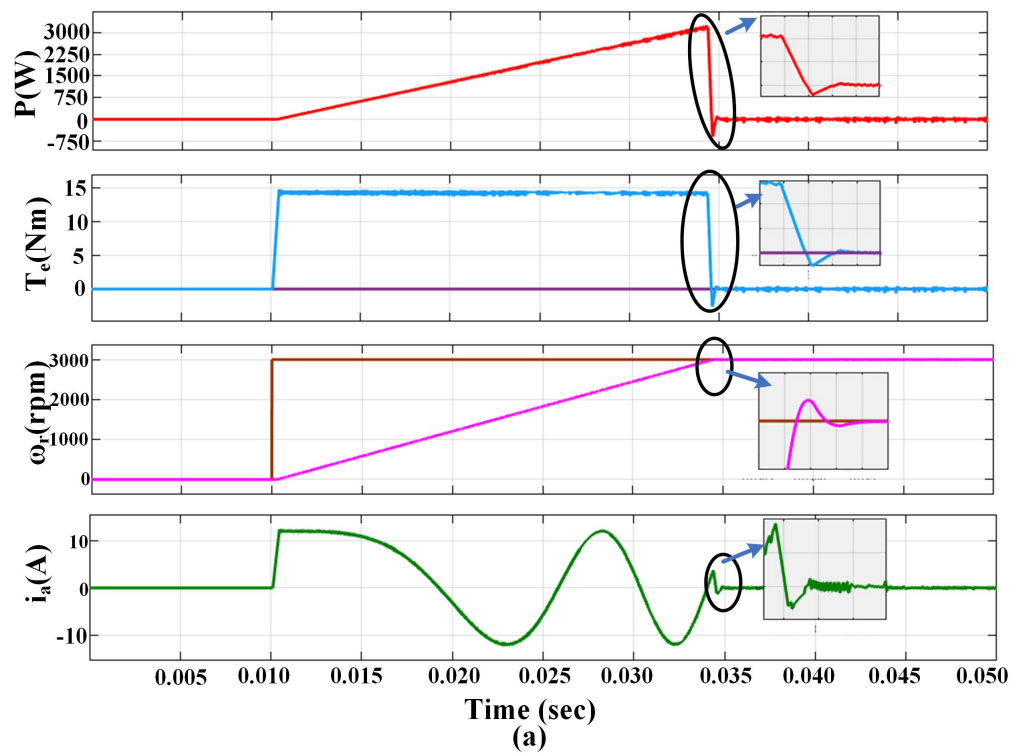


FIGURE 5.4: Dynamic Response of PMSM Drive under no-load rated speed (3000 rpm) Operation(a)PI-HCC b)ANFIS-HCC

Chapter 5. Enhancing PMSM Drive Performance for Electric Vehicles through ANFIS-HCC Integration

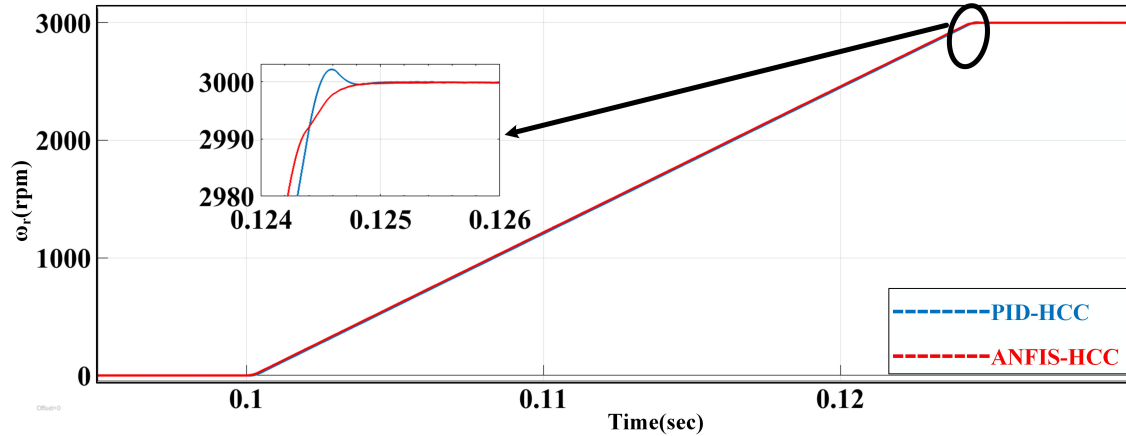


FIGURE 5.5: Starting response of the PI-HCC and ANFIS-HCC based PMSM Drive under no-load-rated speed (3000 rpm) Operation

5.4 Experimental Validation and Comparison of proposed ANFIS-HCC with PI-HCC

5.4.1 Starting Performance of PMSM drive

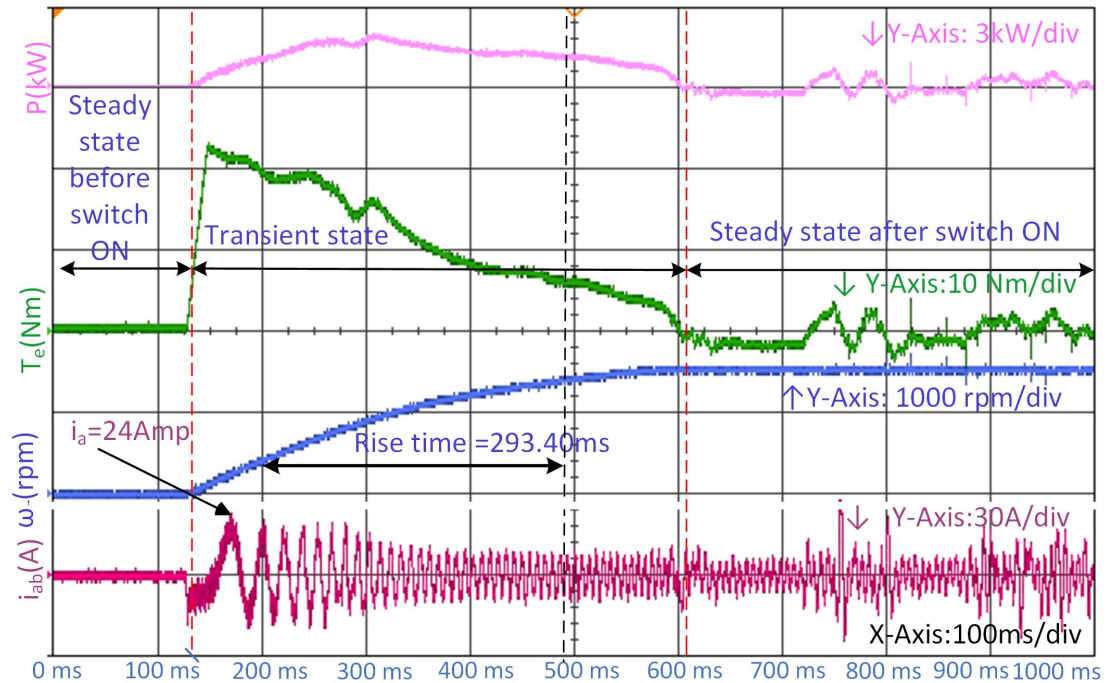
The dynamic response of the laboratory prototype using conventional PI-HCC and the proposed ANFIS-HCC for FOC of PMSM Drive during startup under no load, rated speed (3000 rpm) operation is shown in Figure. 5.6. The electromagnetic torque produced on reaching steady state speed enables the PMSM to achieve and maintain the reference rotor speed. It is observed that the FOC of PMSM using ANFIS-HCC takes 10% lesser rise time as compared to the conventional PI-HCC-based FOC of PMSM. In addition, the speed, torque, and stator currents exhibit some distortion in PI-HCC based controller, unlike the ANFIS-HCC-based controller. The ANFIS-HCC controller is thus observed to offer a quick and smooth response.

5.4.2 Steady-state performance of PMSM drive

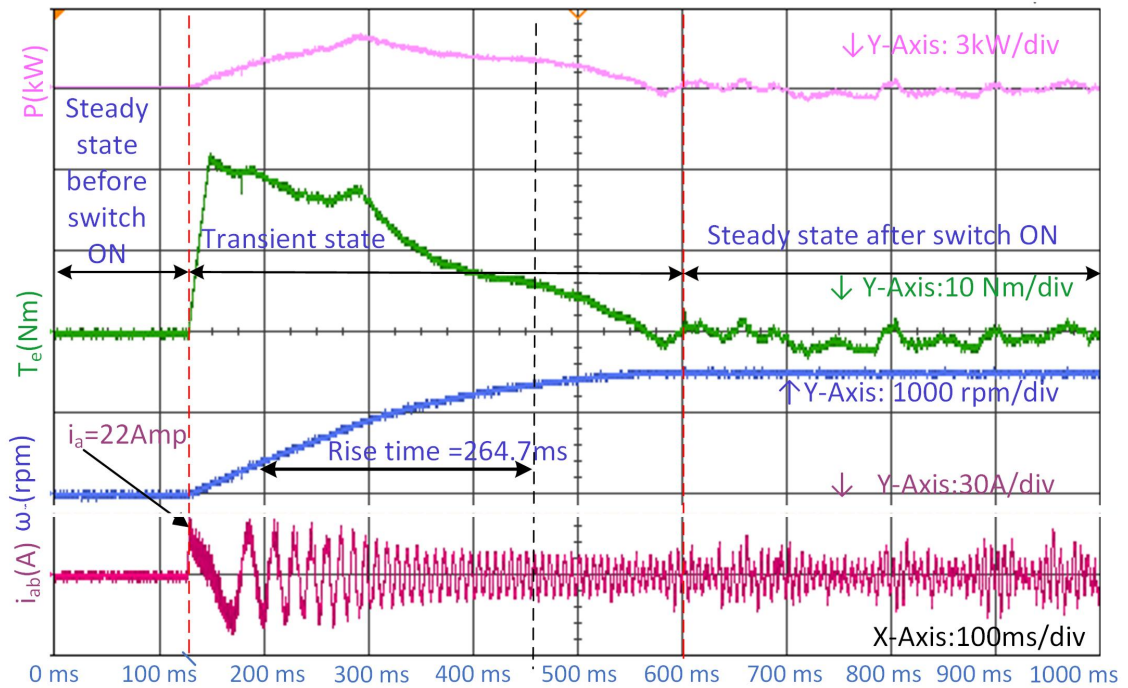
To validate the effectiveness of the proposed ANFIS-HCC-based scheme for FOC of PMSM Drive, the Steady State performance is assessed under different speeds with load torque of 25%, 50%, and 75% of its rated load. The motor speed, electromagnetic torque, stator current, and input power for the PMSM drive

5.4. Experimental Validation and Comparison of proposed ANFIS-HCC with PI-HCC

71



(a)



(b)

FIGURE 5.6: Dynamic response of laboratory prototype at start-up under rated speed and no-load operation: (a) PI-HCC-based FOC, (b) ANFIS-HCC-based FOC

Chapter 5. Enhancing PMSM Drive Performance for Electric Vehicles through ANFIS-HCC Integration

72

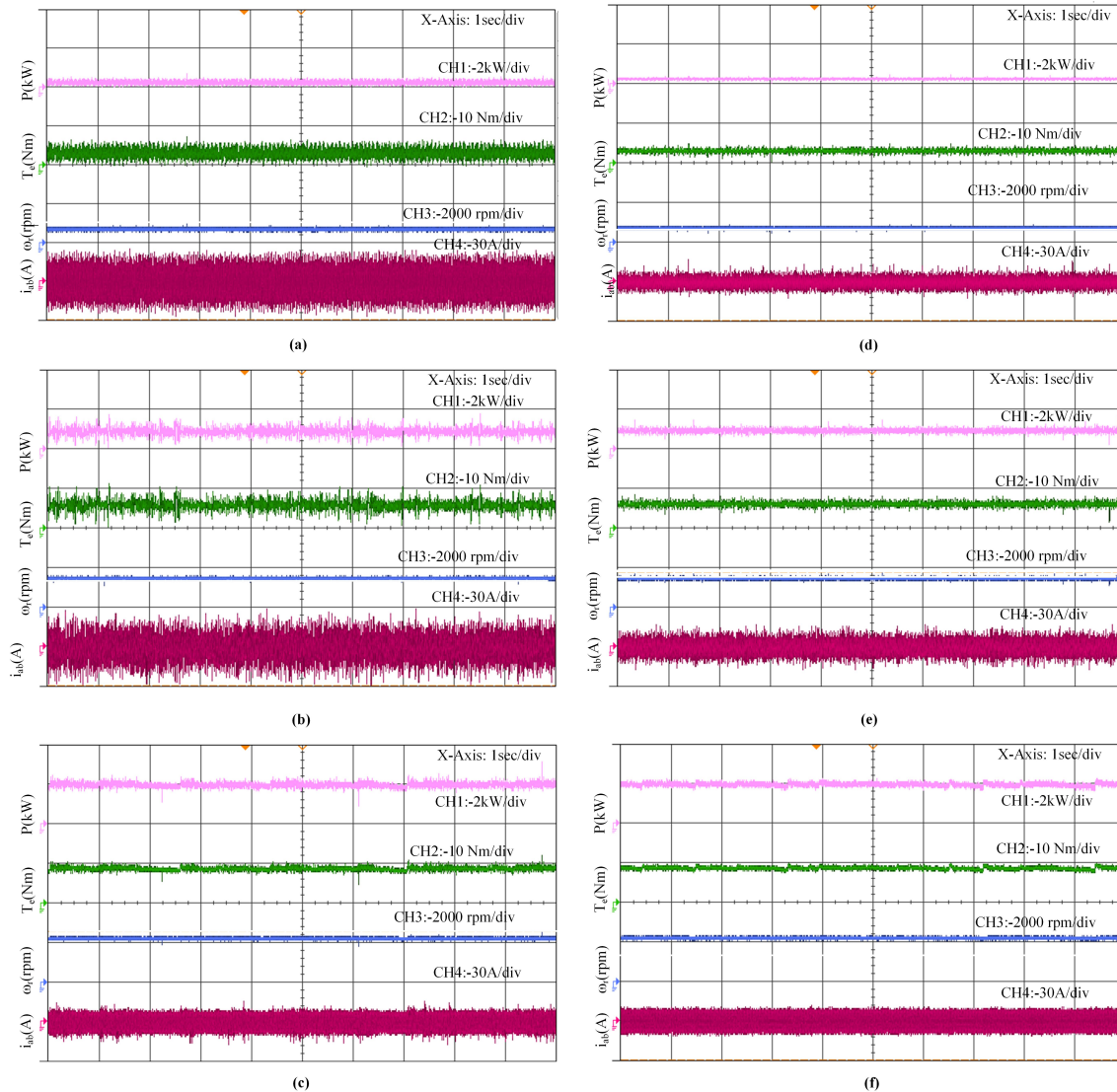


FIGURE 5.7: Steady-state PMSM responses under PI-HCC (a–c) and ANFIS-HCC (d–f) at 750 rpm/3 Nm, 1500 rpm/6 Nm, and 2250 rpm/9 Nm, respectively.

using the conventional PI-HCC and proposed ANFIS-HCC are shown in Figure. 5.7. It is observed that the perturbations in power and current are less in the ANFIS-HCC based FOC. Torque ripples in electromagnetic torque in the above specified steady-state conditions for both the controllers is tabulated in Table. 5.2. The proposed ANFIS-HCC controller has lower torque ripples than PI-HCC at low load and low rpm, but it is comparable to the conventional PI-HCC-based FOC at higher rpm and higher load.

5.4. Experimental Validation and Comparison of proposed ANFIS-HCC with PI-HCC 73

Thus, experimentally validating the better performance of the proposed ANFIS-HCC controller in comparison with the conventional PI-HCC controller with superior torque characteristics with fewer ripples under steady-state conditions for various operating conditions.

TABLE 5.2: Torque Ripple under Steady State Operation

| Control Method | 750 rpm-3 Nm | 1500 rpm-6 Nm | 2250 rpm-9 Nm |
|----------------|--------------|---------------|---------------|
| PI-HCC | 2.05 | 0.53 | 0.31 |
| ANFIS-HCC | 0.80 | 0.40 | 0.22 |

5.4.3 Dynamic Response of PMSM drive under variable conditions

The dynamic response of the PMSM drives with conventional PI-HCC based FOC for step change in speed from 750 to 1500 to 2250 rpm during forward motoring mode under no-load condition, for speed reversal from +1500 to -1500 rpm under no load condition, and step change in load from 0 to 9 Nm at constant speed (2250 rpm) operation are shown in Figures. 5.8 (a) to 5.8 (c) respectively. Figures. 5.8 (d) to 5.8 (f) display the respective corresponding dynamic responses of the drive using the developed ANFIS-HCC for FOC of PMSM drive. It is observed that the proposed ANFIS-HCC-based controller reduces the torque and current ripples and provides smooth transition under step change in speed, step change in load, and change in motoring mode. The comparative analysis of the recovery time for the two controllers for a step change in load is given in Table. 5.3. To further validate the robustness of the proposed ANFIS-HCC controller, simulations and experiments were conducted under two key conditions: (i) maintaining constant speed with a step change in load (0 to 9 Nm), and (ii) maintaining constant load (5 Nm) with step changes in speed (750 to 1500 to 2250 rpm). The comparative performance of the conventional PI-HCC and proposed ANFIS-HCC controllers is summarized in Table. 5.3. It is evident that the ANFIS-HCC controller provides improved dynamic response, lower speed error, and reduced torque ripple across both scenarios. These observations obtained from steady-state and dynamic condition highlight the superior transient handling capability of the ANFIS-HCC-based controller under dynamic operating conditions. To further quantify these

Chapter 5. Enhancing PMSM Drive Performance for Electric Vehicles through ANFIS-HCC Integration

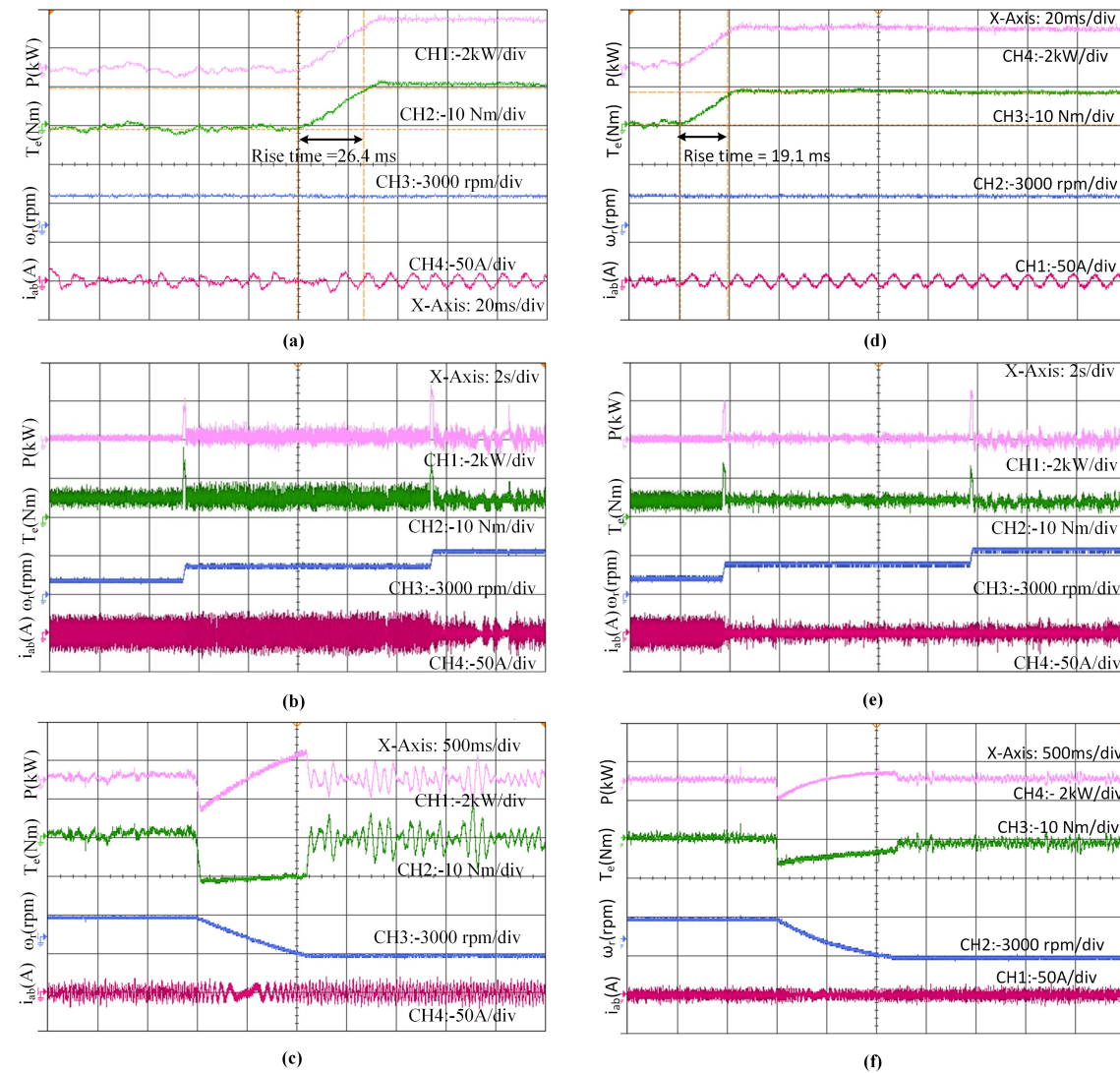


FIGURE 5.8: PMSM responses under PI-HCC (a–c) and ANFIS-HCC (d–f) based FOC schemes: (a,d) Step speed change (750 → 1500 → 2250 rpm) @ 5 Nm; (b,e) Speed reversal (+1500 → −1500 rpm) @ no load; (c,f) Step load change (0 → 9 Nm) @ 2250 rpm.

improvements, a comparative analysis is presented based on experimental data. The proposed controller achieves a reduction in torque ripple of up to 61% at low speed (750 rpm, from 2.05 Nm to 0.80 Nm) and 29% at high speed (2250 rpm, from 0.31 Nm to 0.22 Nm). Additionally, the rise time is improved by 9.8% (from 293.4 ms to 264.7 ms), and settling time by 11.2%. During step load variation, the speed error is reduced by over 55%, from ±45 rpm (PI-HCC) to ±20 rpm

5.4. Experimental Validation and Comparison of proposed ANFIS-HCC with PI-HCC 75

TABLE 5.3: Comparative Performance of PI-HCC and ANFIS-HCC under Varying Operating Conditions

| Condition | Controller | Rise Time (ms) | Settling Time (ms) | Over-shoot (%) | Under-shoot (%) | Speed Error (rpm) | Torque Ripple (Nm) |
|--|------------|----------------|--------------------|----------------|-----------------|-------------------|--------------------|
| Constant Speed (2250 rpm), Load 0→9 Nm | PI-HCC | 26.4 | 48.0 | 5.2 | 3.7 | ±45 | 0.31 |
| | ANFIS-HCC | 19.1 | 41.2 | 2.1 | 1.5 | ±20 | 0.22 |
| Constant Load (5 Nm), Speed 750→2250 rpm | PI-HCC | 54.3 | 90.5 | 7.5 | 6.2 | ±60 | 0.53 |
| | ANFIS-HCC | 40.1 | 72.8 | 3.2 | 2.4 | ±25 | 0.38 |

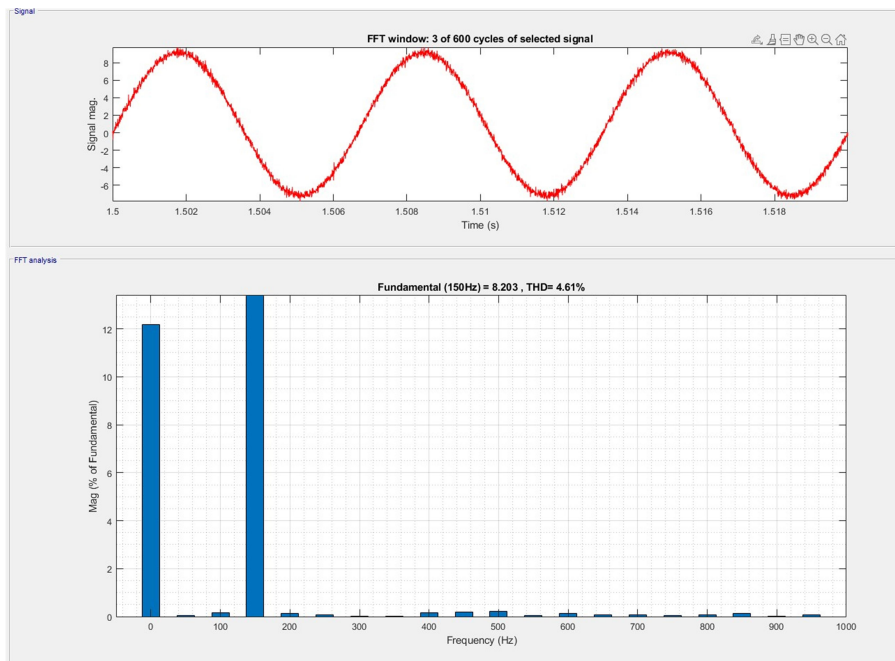
(ANFIS-HCC), confirming better speed tracking accuracy.

Furthermore, harmonic analysis of the stator current Figure. 5.9 shows that the current THD is reduced from 4.61% (PI-HCC) to 3.57% (ANFIS-HCC). This indicates better waveform quality and reduced harmonic losses in the motor windings. These improvements were consistent across multiple trials, with less than ±5% variation, validating the robustness and reliability of the proposed controller. THD reduction is practically significant for EV drive standards, as it minimizes torque ripples for smoother operation, reduces electrical losses to enhance efficiency and range, lowers thermal stress on motor and inverter components for improved durability, and aligns with industry standards for electromagnetic compatibility. .

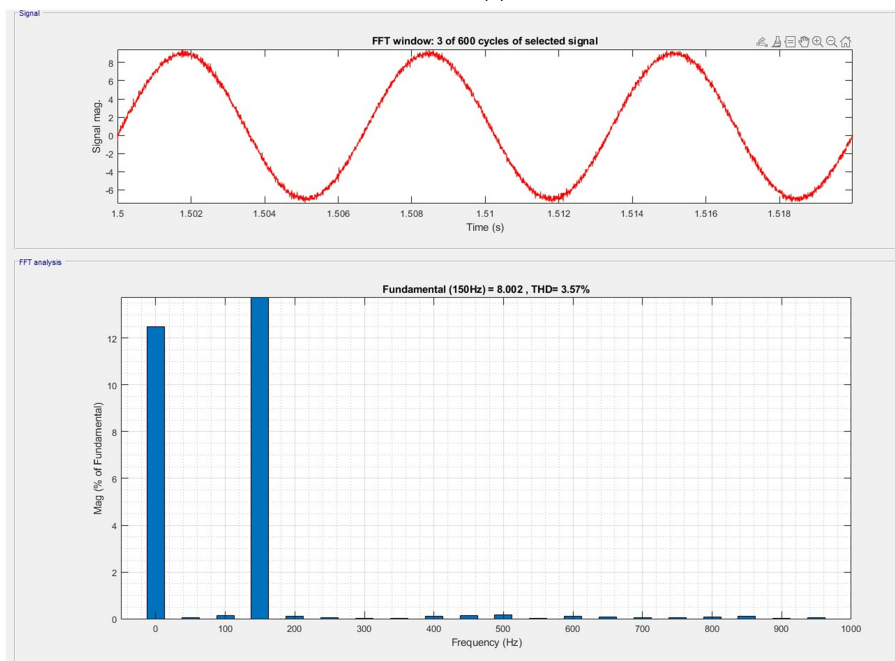
5.4.4 Performance Validation using IM240 Drive Cycle

Electrical motor drives used for EV applications must withstand frequent changes in load torque and speed due to diverse traffic conditions, type of road surface, the gradient of the road, etc. It thus becomes imperative to test electric motor drives for EV applications under such varied operating conditions. The Inspection and Maintenance (IM240) driving cycle, a 240-second test representing a 3.1-km driving track with a maximum speed of 91.2 km/h and an average speed of 47.3 km/h [88], is used to evaluate the effectiveness and energy efficiency of the developed ANFIS-HCC-based laboratory prototype. Figures

Chapter 5. Enhancing PMSM Drive Performance for Electric Vehicles through ANFIS-HCC Integration



(a)



(b)

FIGURE 5.9: Phase current harmonic analysis at 3000rpm at 8Nm load. (a)PI-HCC(b)ANFIS-HCC

5.4. Experimental Validation and Comparison of proposed ANFIS-HCC with PI-HCC

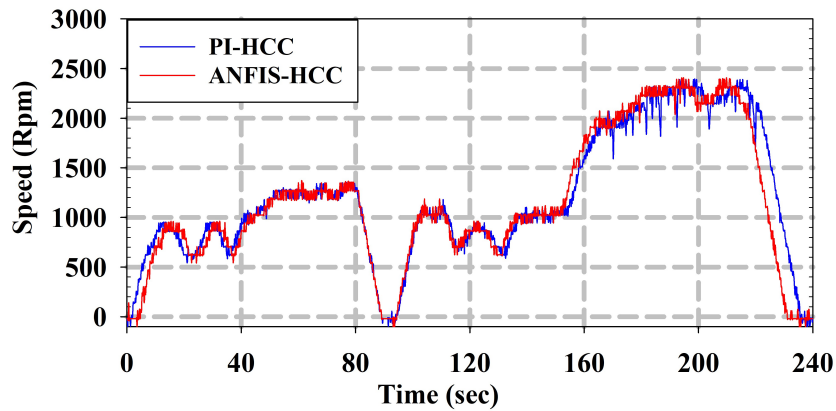


FIGURE 5.10: Speed Response of the Laboratory Prototype for IM240 Drive Cycle.

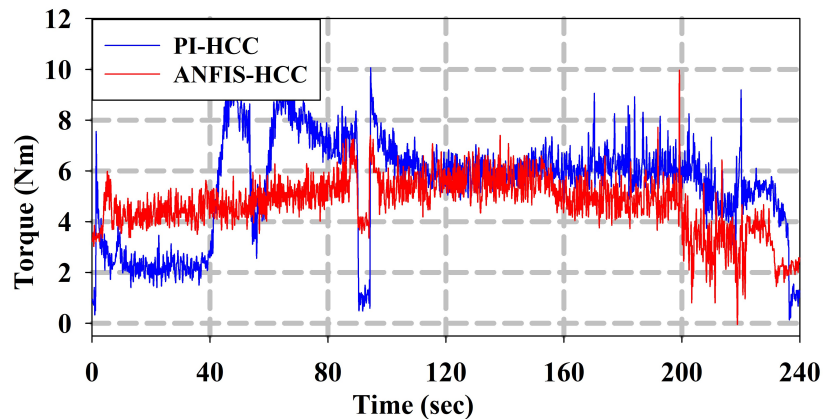


FIGURE 5.11: Torque Response of the Laboratory Prototype for IM240 Drive Cycle

5.10 to 5.13 show the dynamic response of the ANFIS-HCC and PI-HCC-based FOC of the prototype under the IM240 cycle. Both controllers demonstrate flawless speed tracking (Figure. 5.10), but the ANFIS-HCC exhibits superior performance during transients, with smoother torque generation (Figure. 5.11) and 27% lower energy consumption (0.19 kWh vs. 0.26 kWh for PI-HCC, Figure. 5.13).

Further analysis reveals that the ANFIS-HCC achieves 93.71% average efficiency a 4.62% improvement over the PI-HCC's 89.09% as detailed in Table

Chapter 5. Enhancing PMSM Drive Performance for Electric Vehicles through ANFIS-HCC Integration

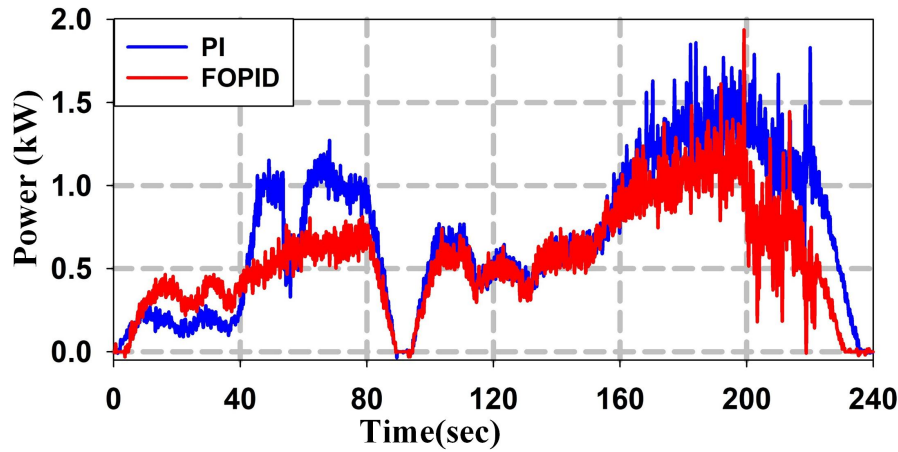


FIGURE 5.12: Power Response of the Laboratory Prototype for IM240 Drive Cycle Power.

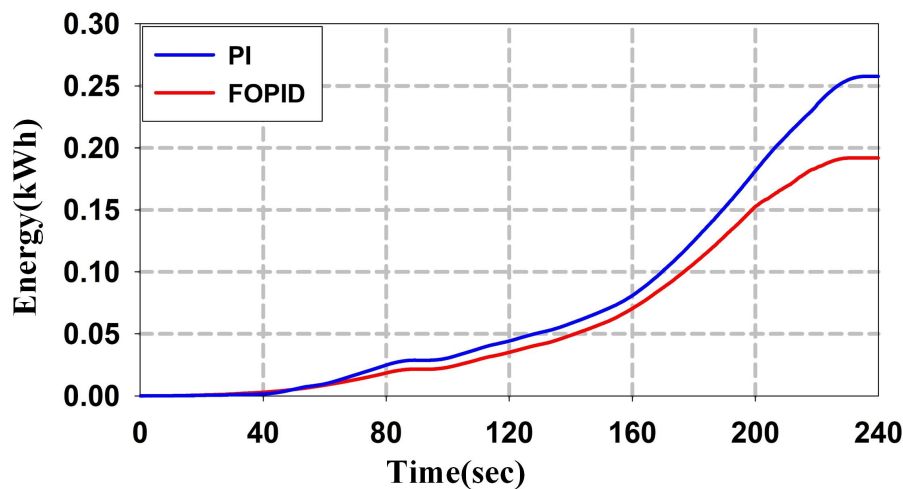


FIGURE 5.13: Energy consumption curve of the Laboratory Prototype for IM240 Drive Cycle Energy

TABLE 5.4: Energy Efficiency Comparison of PI-HCC and ANFIS-HCC Controllers

| Controller | Energy Cons. (kWh) | Efficiency (%) | Wh/km |
|------------|--------------------|----------------|-------|
| PI-HCC | 0.26 | 89.09 | 83.87 |
| ANFIS-HCC | 0.19 | 93.71 | 61.29 |

5.5. Conclusion

79

5.4. This efficiency gain is attributed to reduced torque ripples and optimal power usage, and translates to a lower energy cost of 61.29 Wh/km compared to 83.87 Wh/km for the PI-HCC, reinforcing the ANFIS-HCC's advantages for EV applications under real-world driving conditions. The improved performance under the IM240 cycle is primarily due to smoother transients, reduced current ripple, and better torque regulation achieved by the ANFIS-HCC controller. A 22.56% reduction in current THD and lower torque ripple lead to decreased switching and copper losses. These benefits result in a 27% lower energy consumption and a 4.62% increase in drive efficiency, confirming the controller's suitability for real-world EV conditions.

5.5 Conclusion

This chapter presented a novel ANFIS-HCC strategy for field-oriented control (FOC) of a PMSM drive tailored for EV applications. The proposed control scheme was developed through MATLAB/Simulink simulations and implemented on a laboratory prototype using a DSP-based dSPACE DS1104 controller for experimental validation. Compared to the conventional PI-HCC-based FOC, the ANFIS-HCC controller demonstrated superior performance across various operating conditions, including starting, steady-state operation, step changes in load and torque, and speed reversal. Its suitability for EV applications was further validated using the IM240 Drive Cycle.

Key findings include:

- A 60 % to 65 % reduction in torque ripples at lower speeds and 10 % to 20 % at higher speeds under steady-state conditions,
- up to 28 % faster torque recovery during dynamic speed changes, and
- 27 % lower energy consumption during the IM240 Drive Cycle.

Chapter 6

Ripple and Current Minimization in PMSM Drives Using ANFIS-MPCC for EV Applications

6.1 Introduction

PMSM are favored in electric vehicle propulsion due to their high torque-to-current and power-to-weight ratios, compact size, robustness, and minimal maintenance [111]. However, their nonlinear and multi-variable nature, coupled with uncertainties like friction coefficients, poses significant control challenges [112]. Effective control is essential to address electrical, mechanical, magnetic, thermal, and environmental constraints in EV applications, ensuring optimal performance, fast transient response, and flexibility [113].

Various control strategies, such as Field-Oriented Control (FOC), sliding mode control, Direct Torque Control (DTC), and neuro-fuzzy control, have been developed for high-performance PMSM drives [114–116]. Among these, Model Predictive Control (MPC) has emerged as a robust and efficient methodology, leveraging system models to predict control variable behavior and optimize actions based on predefined criteria [117]. MPC, particularly Finite Control Set Model Predictive Control (FCS-MPC), excels in handling multivariate systems, nonlinearities, and constraints while offering fast dynamic responses [118, 119].

FCS-MPC simplifies implementation by using a finite set of switching states, reducing computational complexity, but faces challenges like steady-state ripple

113 due to single voltage vector application [120, 121]. To address this, an Adaptive Neuro-Fuzzy Inference System-based Model Predictive Current Control (ANFIS-MPCC) is proposed, utilizing the motor's current model in the rotor reference frame and an ANFIS-based adaptation mechanism to manage nonlinearities and parameter variations effectively [122, 123]. This approach aims to enhance steady-state performance, reduce torque ripples, and improve efficiency without increasing sampling frequency.

This chapter explores the design and implementation of the ANFIS-MPCC strategy for PMSM drives in EVs, focusing on its ability to optimize control under diverse operating conditions. The methodology integrates predictive control with adaptive neuro-fuzzy techniques to achieve superior dynamic performance and robust operation.

6.2 Adaptive Neuro-Fuzzy Inference System (ANFIS)

27 As detailed in Chapter 5, the Adaptive Neuro-Fuzzy Inference System (ANFIS) integrates the Takagi-Sugeno fuzzy inference system with artificial neural networks to effectively handle nonlinear control challenges in PMSM drives. ANFIS employs a five-layer architecture to map input-output relationships, using adaptive nodes in Layer 1 to compute fuzzy membership grades, as defined in equations (5.1) and (5.2). A triangular membership function, expressed in equation (5.3), is selected for minimal error. Layer 2 calculates the firing strength of fuzzy rules, while Layer 3 normalizes these strengths. Layer 4 computes the weighted control signals, and Layer 5 aggregates the outputs for defuzzification, as described in Equations (5.4) to (5.7). The ANFIS controller is trained using a hybrid learning approach combining least-squares methods and backpropagation, with 50,001 input-output pairs collected via a dSPACE control desk tool, as outlined in Figure. 5.2. Training over 50 epochs with zero error tolerance ensures optimal accuracy.

In Chapter 6, ANFIS is adapted for Model Predictive Current Control (ANFIS-MPCC), leveraging its ability to manage system nonlinearities and

6.3. Model Predictive Current Control

83

parameter variations, enhancing the control of PMSM drives for electric vehicle applications.

6.3 Model Predictive Current Control

Following the fundamental tenet of predictive control, the Euler algorithm [124] is employed to discretize equation (6.1). Here, T_s denotes the sampling period, and the current at time $(k + 1)$ is predicted on the measurement available at time (k) . The resulting discrete linear time-invariant system is :

$$\begin{cases} i_{sd}(k+1) = \left(1 - \frac{R_s T_s}{L_{sd}}\right) i_{sd}(k) + \omega_r T_s \\ \frac{L_{sq}}{L_{sd}} i_{sq}(k) + \frac{T_s}{L_d} u_d^*(k) \\ i_{sq}(k+1) = \left(1 - \frac{R_s T_s}{L_{sq}}\right) i_{sq}(k) - \omega_r T_s \\ \frac{L_{sq}}{L_{sd}} i_{sd}(k) + \frac{T_s}{L_d} u_q^*(k) - \omega_r T_s \frac{\psi_f}{L_q} \end{cases} \quad (6.1)$$

Due to the extensive computational requirements of the MPC control scheme, there is an inherent delay in its execution [125]. Failure to address this delay issue can impede the controller's ongoing operations, potentially resulting in a decline in control performance. Consequently, it is imperative to account for time delay compensation. Time delay compensation represents a straightforward and effective computational approach, wherein prediction control involves forecasting future values to serve as delay compensation. This approach is applied to current predictions to mitigate the impact of delays in the control process. The delay compensation algorithm is for forecasting the value at time $k + 2$, with the available information at time k , where $u_d^*(k)$ and $u_q(k)$ represent the applied voltage vectors .

$$\begin{cases} i_{sd}(k+2) = \left(1 - \frac{R_s T_s}{L_{sd}}\right) i_{sd}(k+1) + \omega_r T_s \\ \frac{L_{sq}}{L_{sd}} i_{sq}(k+1) + \frac{T_s}{L_{dd}} u_d^*(k) \\ i_{sq}(k+2) = \left(1 - \frac{R_s T_s}{L_{sq}}\right) i_{sq}(k+1) - \omega_r T_s \\ \frac{L_{sq}}{L_{sd}} i_{sd}(k+1) + \frac{T_s}{L_{dd}} u_q^*(k) - \omega_r T_s \frac{\psi_f}{L_q} \end{cases} \quad (6.2)$$

The control objectives of FCS-MPC algorithms are articulated through a cost function, serving as an indicator of the extent to which each switching state of the inverter achieves the desired system behaviour. Specifically, in the context of current control, where the aim is to follow a reference current (i_{sd}^* , i_{sq}^*) with predicted components (i_{sd} , i_{sq}), the cost function is precisely defined as

$$g = |i_{sd}^*(k+2) - i_{sd}(k+2)|^2 + |i_{sq}^*(k+2) - i_{sq}(k+2)|^2 \quad (6.3)$$

6.4 Proposed ANFIS-MPCC PMSM Drive

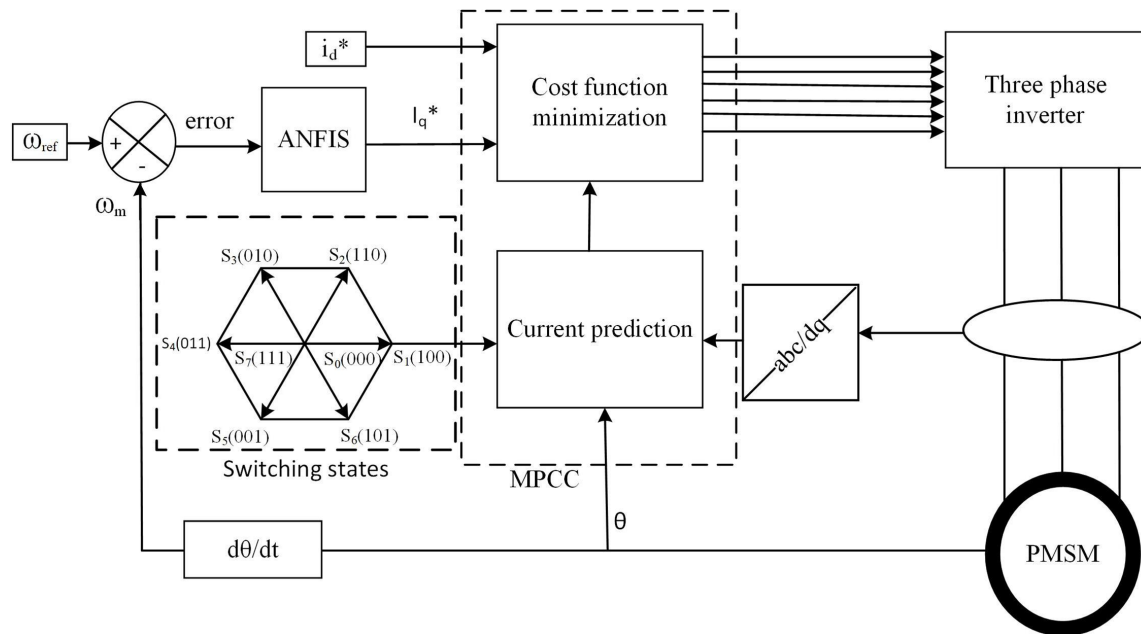


FIGURE 6.1: Proposed ANFIS-MPCC PMSM drive's Block Diagram

The block diagram Figure. 6.1 represents the control architecture of the proposed ANFIS-MPCC for a P PMSM drive, designed to enhance performance in EV applications. The system integrates speed and current control loops, leveraging ANFIS for adaptive control and MPCC for predictive current regulation.

The control process initiates with the reference speed ω_{ref} , which is compared to the measured rotor speed ω_m of the PMSM through a feedback loop. The speed error, calculated as $\omega_{ref} - \omega_m$, is fed into the ANFIS block. The ANFIS, a hybrid

6.4. Proposed ANFIS-MPCC PMSM Drive

85

of neural networks and fuzzy logic, processes this error to generate the reference d-axis and q-axis currents, i_d^* and i_q^* , respectively. The d-axis current i_d^* is typically set to zero for maximum torque per ampere operation in PMSM drives, while i_q^* directly influences the torque production. The ANFIS employs a Takagi-Sugeno fuzzy inference system, utilizing a five-layer architecture (as detailed in Chapter 5) to map the nonlinear relationship between the speed error and the reference currents, adapting to system variations through a hybrid learning algorithm.

These reference currents i_d^* and i_q^* are then passed to the Cost Function Minimization block within the Model Predictive Current Control (MPCC) framework. The MPCC operates by predicting the future behavior of the PMSM currents based on the motor's mathematical model and a finite set of switching states. The Switching States block illustrates the possible voltage vectors S_0 to S_7 , corresponding to the eight switching combinations of a three-phase inverter (e.g., $S_0(000)$, $S_1(100)$, ..., $S_7(111)$). Each state defines a unique voltage vector applied to the PMSM, influencing the stator currents.

The Current Prediction block within the MPCC uses the discrete-time model of the PMSM in the d-q reference frame to forecast the d-axis and q-axis currents (i_d , i_q) at the next sampling instant for each switching state. The prediction model accounts for the motor's electrical dynamics, including stator resistance, inductance, and back-EMF, as well as the rotor position θ , obtained from the PMSM feedback. The predicted currents are then compared against the reference currents i_d^* and i_q^* in the Cost Function Minimization block. The cost function, typically defined as the squared error between predicted and reference currents given in equation (6.3), may also include additional terms to penalize excessive switching or constraint violations. The MPCC selects the switching state that minimizes this cost function, ensuring optimal current tracking and minimal ripple.

The selected switching state is applied to the Three-Phase Inverter, which converts the DC-link voltage into a three-phase AC voltage to drive the PMSM. The inverter's output voltages, corresponding to the chosen voltage vector, regulate the stator currents, thereby controlling the torque and speed of the PMSM. The rotor position θ and its derivative $d\theta/dt$, representing the electrical angular velocity, are fed back to the MPCC for coordinate transformations (abc to dq) and current prediction, ensuring alignment with the rotor reference frame.

The abc/dq transformation block facilitates this conversion, enabling the control of currents in the synchronous d-q frame, which is essential for Field-Oriented Control (FOC) principles embedded within the MPCC.

This integrated ANFIS-MPCC approach enhances the PMSM drive's performance by combining the adaptive, nonlinearity-handling capabilities of ANFIS with the predictive, constraint-aware nature of MPCC, resulting in improved dynamic response, reduced torque ripple, and robust operation under varying vehicular conditions.

6.5 Simulaton Results and Discussion

This section describes the simulations studies on a 3.4k kW PMSM with parameters as shown in Table 3.2. To assess the efficacy of the proposed novel ANFIS-MPCC technique, siumaltion model is developed in MATLAB/SIMULINK and also a prototype laboratory setup to validate the simulated results . This study describes comparative simulations conducted on a 3.4kW PMSM to assess the efficacy of the proposed method. The simulation commences with an initial speed of 2250 rpm(75% of the rated speed) and a load torque of 8Nm(100% of the rated load)as shown in Figure. 6.2. In the time interval from 0 to 0.6 seconds, the PI-HCC algorithm is utilized, followed by the execution of ANFIS-HCC from 0.6 to 1.2 sec. Subsequently, PI-MPCC is implemented from 1.2 sec to 1.8 sec, and the proposed algorithm is activated from 1.8 sec to 2.4 sec. Upon a sudden reduction in the speed command from 2250 to 500 rpm, the motor speed closely tracks the reference speed. The proposed ANFIS-MPCC exhibits a slightly reduced torque ripple(TR). There is percentage reduction of 73.2% as comapred to (PI-HCC), 50.5% as compared to (ANFIS-HCC), and 37.8% as comapred to (PI-MPCC) at 2250rpm . At low speed of 500rpm, ANFIS-MPCC yields a lower percentage torque ripple of 64.9% , 32.3% , and 11.8% (PI-HCC), and (ANFIS-HCC)(PI-MPCC).

Similarly , in the event of a sudden reduction in load torque from 8 Nm to 2 Nm, the speed controller sustains the constant speed at 2250 rpm, with a momentary speed dip illustrated in Figure. 6.3. Furthermore, at 100% of full

6.6. Experimental Results and Analysis

87

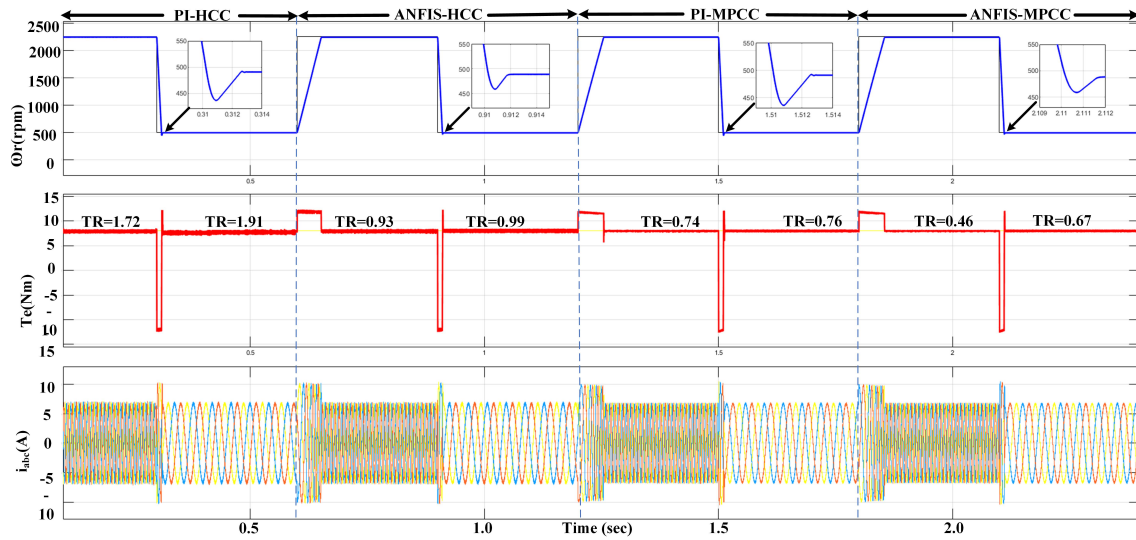


FIGURE 6.2: Dynamic response while Speed change from 2250 to 500rpm at 8Nm load

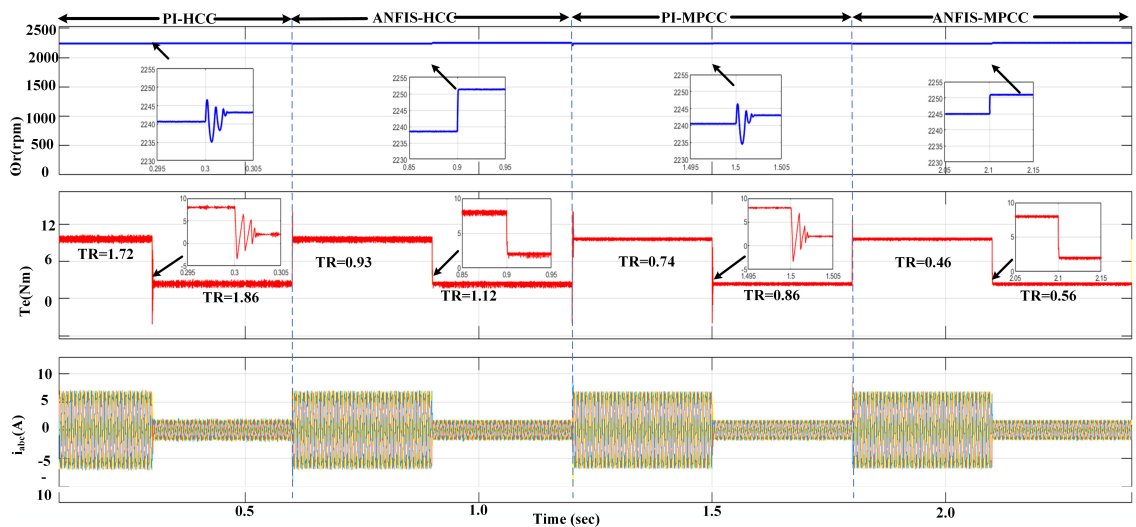


FIGURE 6.3: Dynamic response while load change from 8Nm to 2Nm at 2250rpm

load, it is observed that ANFIS-MPCC exhibits a lower torque ripple compared to other control algorithms, as detailed in Table. 6.1.

TABLE 6.1: Comparative Simulation Results of Torque Ripples

| Control Scheme | PI-HCC | ANFIS-HCC | PI-MPCC | ANFIS-MPCC |
|-------------------|--------|-----------|---------|------------|
| 2250rpm, 8Nm (Nm) | 1.72 | 0.93 | 0.74 | 0.46 |
| 500rpm, 8Nm (Nm) | 1.91 | 0.99 | 0.76 | 0.67 |
| 2250rpm, 2Nm (Nm) | 1.86 | 1.12 | 0.86 | 0.56 |

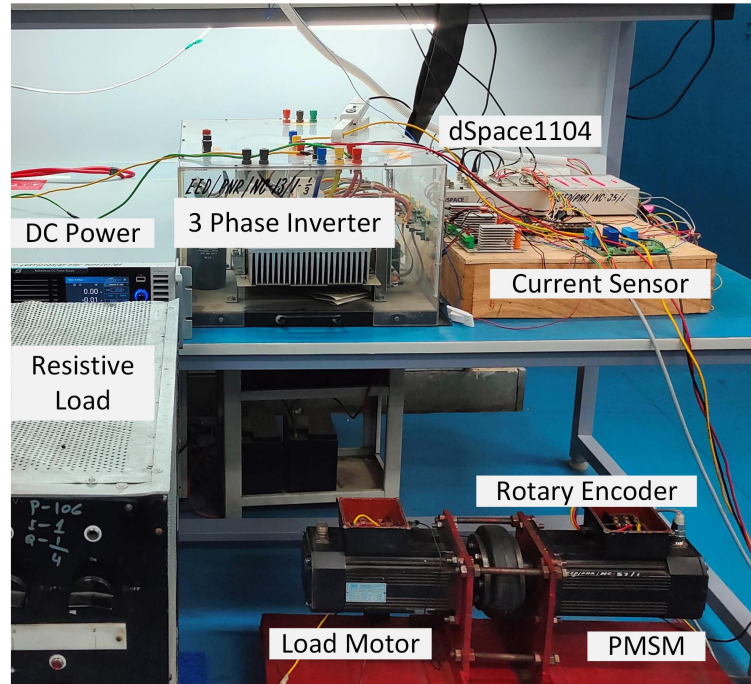


FIGURE 6.4: Laboratory Prototype for testing the ANFIS-MPCC based PMSM drive

6.6 Experimental Results and Analysis

This section presents a comparative study of theoretical and experimental results, conducted using a 3.4kW experimental setup featuring a PMSM with parameters listed in Table 3.2. The setup evaluates the efficacy of the proposed ANFIS-MPCC scheme for a six-leg Voltage Source Inverter (VSI) driving the PMSM. Experimental tests of the ANFIS-MPCC scheme were performed and compared with conventional Proportional-Integral Hysteresis Current Control (PI-HCC) schemes. Details of the laboratory prototype for the PMSM drive are provided in Chapter 4 and illustrated in Figure. 6.4.

In each control approach, the PI controller parameters are tuned according to

6.6. Experimental Results and Analysis

89

the Ziegler Nichols method to attain optimal control performance. To facilitate a fair comparison, the speed PI controller maintains consistent parameters across all schemes, set as $K_p = 0.012$ and $K_i = 0.2$

6.6.1 Dynamic performance of PMSM drive

In this experimental setup, PMSM is initially started with a speed of 2250 rpm, representing 75% of the rated speed, and a load torque of 8 Nm, corresponding to 100% of the rated load . The PI-HCC algorithm is used in the time interval from 0 to 20 seconds, followed by the execution of ANFIS-HCC from 20.1 to 50 seconds. Subsequently, PI-MPCC is applied from 50.1 seconds to 80 seconds, and the proposed algorithm is activated from 80.1 seconds to 100 seconds as shown in Figure. 6.5. When the speed command undergoes an abrupt reduction from 2250 to 500 rpm, the motor speed closely adheres the reference speed. The proposed ANFIS-MPCC, as suggested, exhibits a significantly reduction in torque ripple of 70.9%, 58.9%, and 33.3% in comparison to PI-HCC, ANFIS-HCC, and PI-MPCC, respectively, at 2250 rpm. Likewise, at 500 rpm, the torque ripple is decreased by 64.7%, 58.3%, and 45.5%when compared to the corresponding control strategies mentioned above as delineated in Table. 6.2.

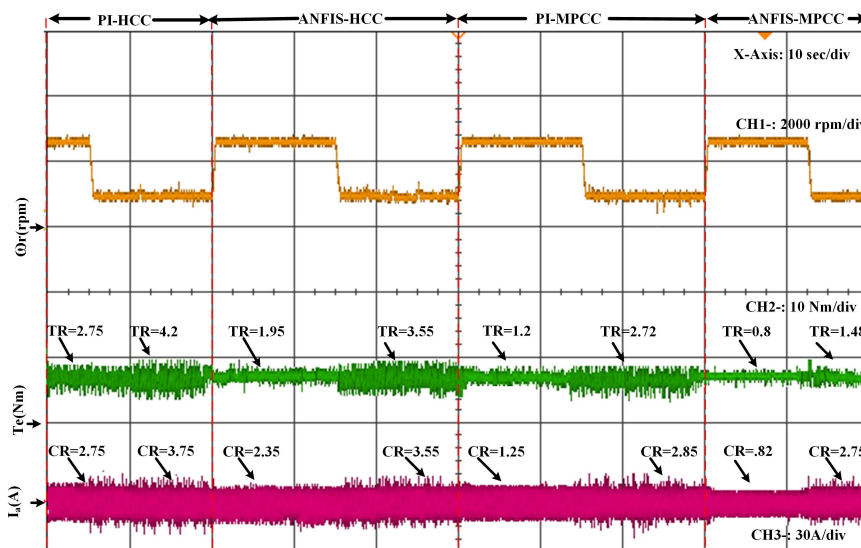


FIGURE 6.5: Dynamic response for step speed change from 2250 to 500rpm at 8Nm load

Chapter 6. Ripple and Current Minimization in PMSM Drives Using ANFIS-MPCC for EV Applications

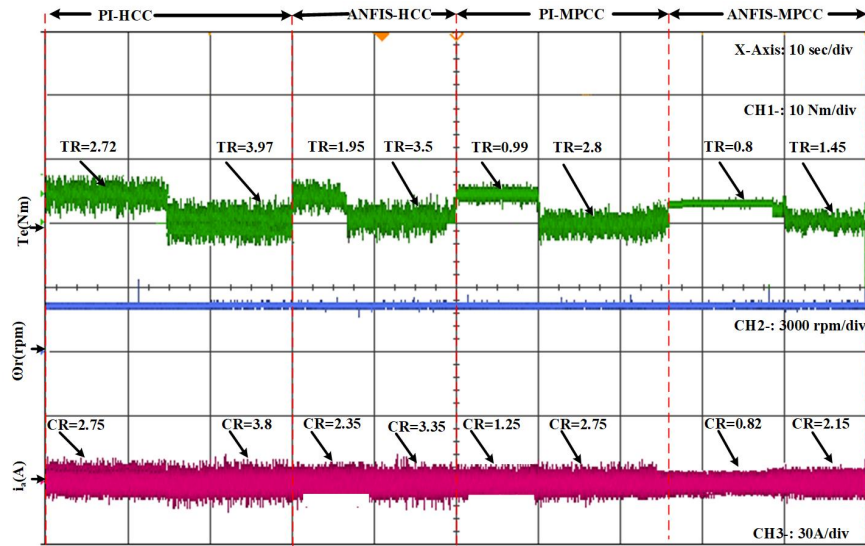


FIGURE 6.6: Dynamic response for step load change from 8Nm to 2Nm at 2250rpm

TABLE 6.2: Comparative Experimental Results of Torque Ripples

| Control Scheme | PI-HCC | ANFIS-HCC | PI-MPCC | ANFIS-MPCC |
|-------------------|--------|-----------|---------|------------|
| 2250rpm, 8Nm (Nm) | 2.75 | 1.95 | 1.20 | 0.80 |
| 500rpm, 8Nm (Nm) | 4.20 | 3.55 | 2.72 | 1.48 |
| 2250rpm, 2Nm (Nm) | 3.97 | 3.50 | 2.80 | 1.45 |

TABLE 6.3: Comparative Experimental Results of Current Ripples

| Control Scheme | PI-HCC | ANFIS-HCC | PI-MPCC | ANFIS-MPCC |
|--------------------|--------|-----------|---------|------------|
| 2250rpm, 8Nm (Nm) | 2.75 | 2.35 | 1.25 | 0.82 |
| 500rpm, 8Nm (Nm), | 3.75 | 3.55 | 2.85 | 2.75 |
| 2250rpm, 2Nm (Nm), | 3.8 | 3.35 | 2.75 | 2.15 |

Similarly, in the case of an abrupt decrease in load torque from 8 Nm to 2 Nm, the speed controller sustains at steady-state speed at 2250 rpm with a temporary dip in speed as shown in Figure. 6.6. Furthermore, under conditions of full load (100%), it is observed that ANFIS-MPCC exhibits a reduced current ripples as compared to alternative control algorithms, as delineated in Table. 6.3. Comparative Analysis of Normalised Torque and Current Ripples are presented in Figures. 6.7 and 6.8 where TR and CR of proposed ANFIS-MPCC method are taken as reference '1'. Figure. 6.9 shows the fast fourier analysis of phase current

6.6. Experimental Results and Analysis

91

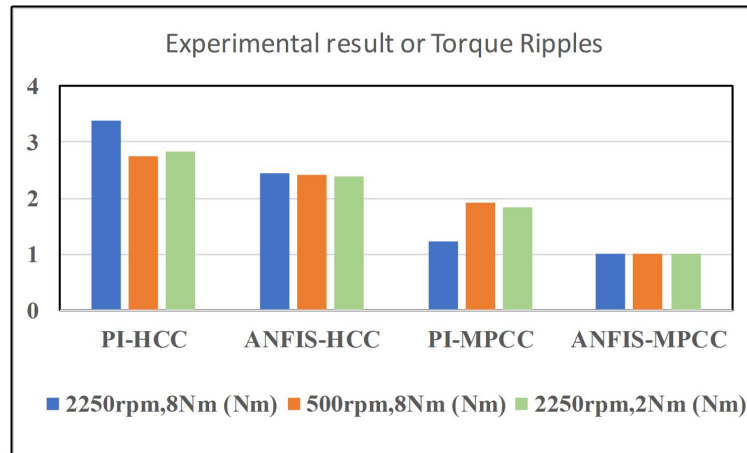


FIGURE 6.7: Comparative Analysis of Normalised Torque Ripple

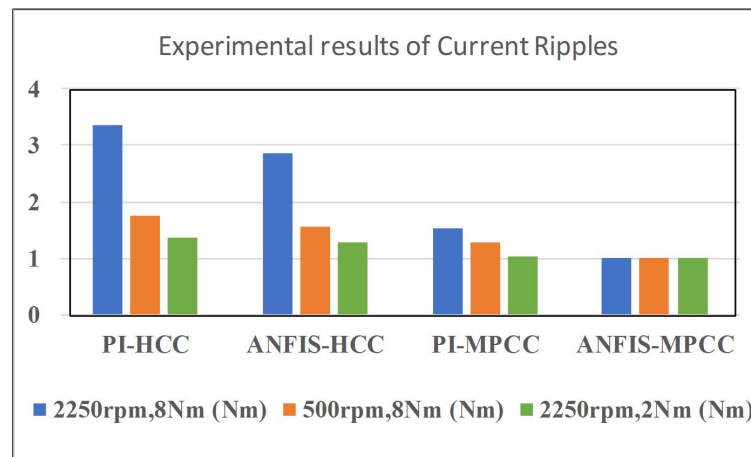


FIGURE 6.8: Comparative Analysis of Normalised Current Ripple

at 2250rpm with mechanical load of 8 Nm. The proposed method shows 52.48%, 45.05%, and 3.3% reduction in harmonics as compared to PI-HCC, ANFIS-HCC, and PI-MPCC, respectively.

The proposed ANFIS-MPCC controller significantly reduces current ripple. At 2250 rpm, it achieves a reduction of 70.2%, 65.1%, and 36% compared to PI-HCC, ANFIS-HCC, and PI-MPCC, respectively. Similarly, at 500 rpm, the current ripple is reduced by 26.6%, 22.5%, and 3.1% when compared with the same control strategies, as tabulated in Table. 6.3..

The proposed ANFIS-MPCC demonstrates diminished Current Ripple (CR) of 70.2%, 65.1%, and 36% as compared to PI-HCC, ANFIS-HCC, and PI-MPCC,

respectively, at 2250 rpm. Similarly, at 500 rpm, there is a reduction in current ripple by 26.6%, 22.5%, and 3.1% in comparison to the respective a fore mentioned control strategies as shown in Table. 6.3.

6.6.2 Performance validation using vehicular condition

The performance, reliability, and safety of PMSM drive systems for EV are validated through comprehensive testing to ensure efficient and dependable propulsion. The validation process encompasses Dynamic Performance Evaluation, Load Simulation, and Efficiency and Range Assessment. Dynamic Performance Evaluation assesses the motor's torque output, speed responsiveness, and current draw under diverse driving scenarios, including acceleration, deceleration, and constant-speed operations, to evaluate operational efficiency. Load Simulation tests the motor under varied vehicle loads and road conditions, such as uphill driving or heavy payloads, to gauge performance under stress. Efficiency and Range Assessment measures energy consumption across different speeds and driving modes to optimize motor functionality for maximum vehicle range and minimal energy use.

A standard automotive drive cycle test is employed to validate the viability and robustness of the proposed ANFIS-MPCC technique for vehicular condition. The Modified Indian Drive Cycle (MIDC) is the modified form of NEDC (New European Drive Cycle) [126] designed for Indian traffic condition. The MIDC accounts for wider speed profiles is used to assess the performance of the proposed ANFIS-MPCC across a broad spectrum of speed changes. Such speed changes are very common in urban drive cycle and this drive cycle test is conducted at a constant load of 4 Nm and zero inclination. The dynamic performance of laboratory prototype with the suggested ANFIS-MPCC is tested with the MIDC. The Motor speed (ω_r), Electromagnetic torque (T_e), Power (P) and current (I_a) are illustrated in Figure. 6.10

Comparative analysis of the energy consumption is also carried out for the traditional (PI-HCC, ANFIS-HCC and PI-MPCC) and proposed (ANFIS-MPCC) algorithms with MIDC and is shown in Figure. 6.11 It is observed that the proposed ANFIS-MPCC resulted in less energy consumption as compared to the

6.6. Experimental Results and Analysis

93

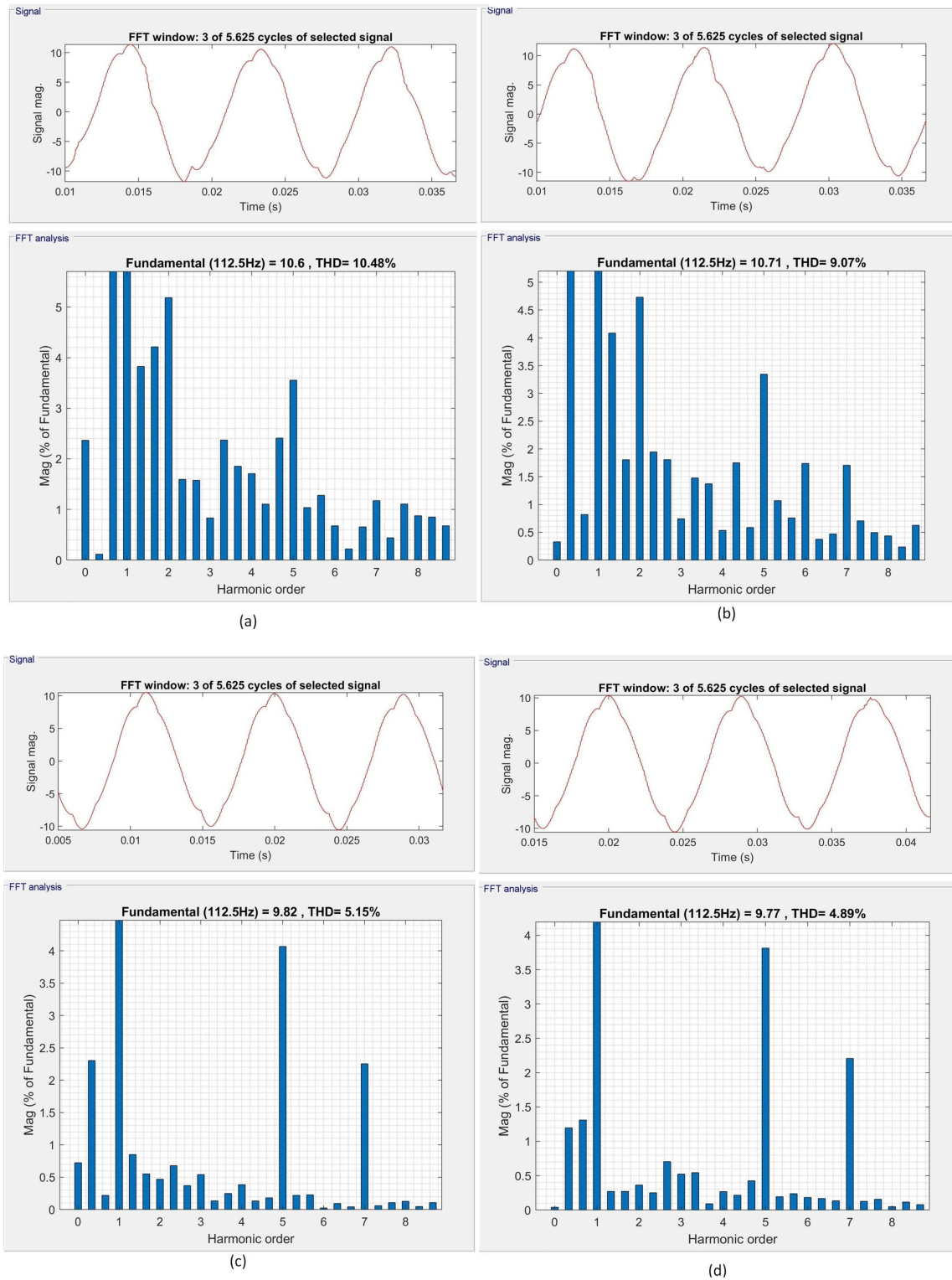


FIGURE 6.9: Phase current harmonic analysis at 2250rpm at 8Nm load. (a)PI-HCC(b)ANFIS-HCC(c)PI-MPCC(d)ANFIS-MPCC

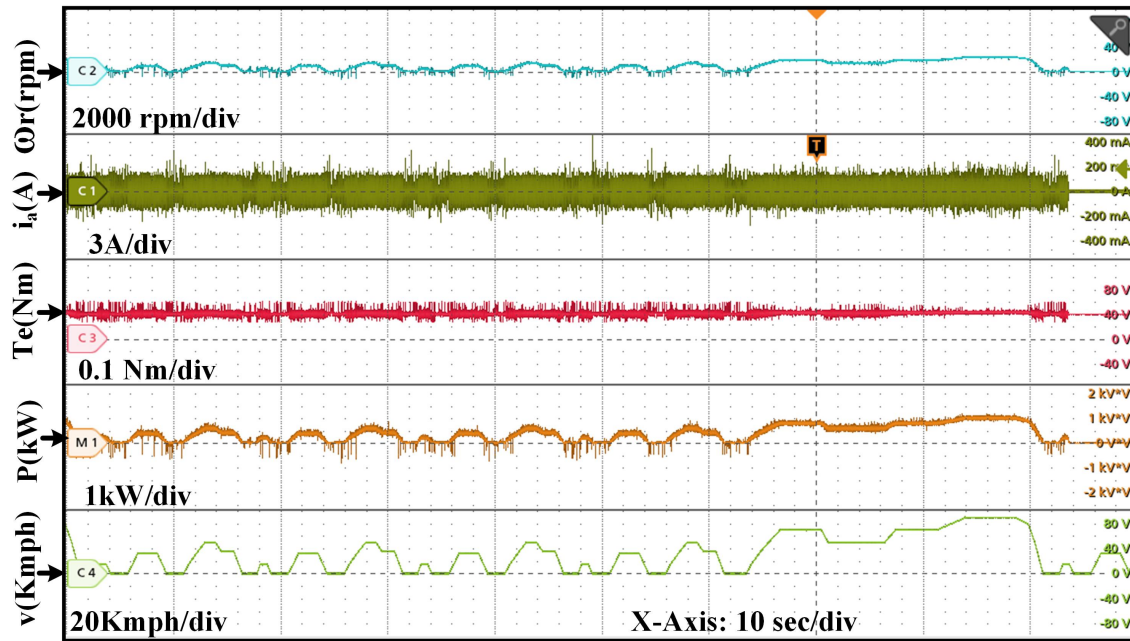


FIGURE 6.10: Dynamic Response of MIDC Drive Cycle

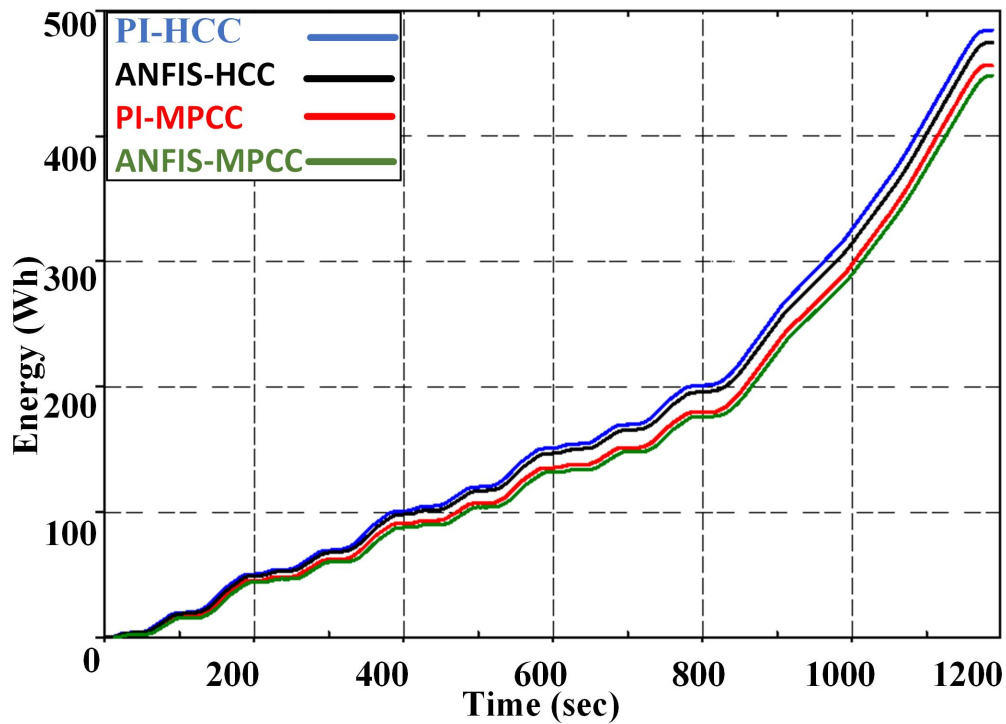


FIGURE 6.11: Comparative Analysis of energy consumption for MIDC Cycle

other methods, thus validating that the proposed ANFIS-MPCC is best suited for EV applications.

6.7 Conclusion

This chapter introduces an innovative ANFIS-MPCC approach for speed control of PMSM drives. By leveraging predictive optimization and precise current tracking, the proposed method minimizes torque ripples through a model-based cost function, suppresses current harmonics, and adapts dynamically to varying speeds and loads. Compared to traditional PI-HCC, ANFIS-HCC, and PI-MPCC strategies, it significantly reduces torque and current ripples, as validated through simulation and hardware implementation. Experimental results using the MIDC drive cycle demonstrate a notable reduction in energy consumption by 10.2%, 6.7%, and 2.6% compared to PI-HCC, ANFIS-HCC, and PI-MPCC, respectively. The ANFIS-MPCC controller offers the following advantages:

1. Under steady-state conditions, torque ripples are reduced by up to 70.9% at high speed and 64.7% at low speed compared to PI-HCC, with similar improvements over ANFIS-HCC and PI-MPCC.
2. Smoother dynamic response to speed changes and lower current ripples at both low and high speeds.
3. Enhanced power quality with harmonic reductions of 52.48%, 45.05%, and 3.3% compared to PI-HCC, ANFIS-HCC, and PI-MPCC, respectively.

These results confirm the superiority of the ANFIS-MPCC method in achieving enhanced steady-state and dynamic performance, making it a promising solution for PMSM drives in electric vehicle applications.

Chapter 7

Intelligent control of PMSM Drive using ANFIS-SMCC for EVs

7.1 Introduction

PMSMs are widely used in EVs due to their efficiency and high torque density, but they present control challenges such as nonlinearities, parameter sensitivity, and load variations [127]. Conventional methods like FOC and DTC suffer from ripple and poor adaptability under dynamic conditions [128, 129].

Sliding Mode Control (SMC) offers strong robustness, finite-time convergence, and disturbance rejection, but classical forms face chattering and limited adaptability. Enhanced variants such as adaptive, recursive, fixed time, and event triggered SMC have improved flexibility and precision. Hybrid approaches like ANFIS-SMC further boost adaptability by combining SMC robustness with ANFIS learning, although real-time implementation remains challenging.

To address these limitations, the ANFIS-SMC integrates sliding mode's robustness with ANFIS-based adaptive tuning. It ensures accurate d-q axis current regulation under parameter variations and load disturbances, while mitigating chattering via smooth switching functions. This makes it a scalable, intelligent solution for resilient EV motor control.

7.2 Adaptive Neuro-Fuzzy Inference System (ANFIS)

Chapter 5 discusses ANFIS, which blends Takagi–Sugeno fuzzy logic with neural networks to address PMSM nonlinearities. Its five-layer structure handles fuzzy rule inference and output aggregation using triangular membership functions for minimal error. ANFIS is trained with a hybrid method (least squares and backpropagation) on data from dSPACE tools, achieving high accuracy within 50 epochs.

In this chapter, ANFIS is incorporated into Sliding Mode Current Control (ANFIS-SMCC) to improve PMSM performance under parameter variations in EV applications.

7.3 Sliding Mode Current Control (SMCC)

Sliding Mode Current Control (SMCC) is used to make sure the motor currents follow their desired values closely, even if there are disturbances or changes in the system.

First, we define the current tracking errors, also called sliding surfaces.

$$s_d = i_{sd,ref} - i_{sd}, \quad (7.1)$$

$$s_q = i_{sq,ref} - i_{sq}, \quad (7.2)$$

where $i_{sd,ref} = 0$ (for maximum torque per ampere) and $i_{sq,ref}$ is calculated from the reference torque.

The control voltages for the d- and q-axes each have two parts: an “equivalent” part and a “switching” part:

$$u_{sd} = u_{sd,eq} + u_{sd,sw}, \quad (7.3)$$

$$u_{sq} = u_{sq,eq} + u_{sq,sw}, \quad (7.4)$$

The equivalent control terms are:

$$u_{sd,eq} = R_s i_{sd} - \omega_r L i_{sq} + L \frac{di_{sd,ref}}{dt}, \quad (7.5)$$

7.3. Sliding Mode Current Control (SMCC)

99

$$u_{sq,eq} = R_s i_{sq} + \omega_r L i_{sd} + \omega_r \psi_f + L \frac{di_{sq,ref}}{dt}, \quad (7.6)$$

The switching control terms help the system quickly correct errors and handle disturbances:

$$u_{sd,sw} = k_d \text{sat} \left(\frac{s_d}{\phi_d} \right), \quad (7.7)$$

$$u_{sq,sw} = k_q \text{sat} \left(\frac{s_q}{\phi_q} \right), \quad (7.8)$$

where k_d and k_q are control gains, and $\phi_d = \phi_q = 0.1$ are small values that define the “boundary layer” to reduce unwanted high-frequency switching (chattering).

The saturation function $\text{sat}(\cdot)$ is defined as:

$$\text{sat} \left(\frac{s}{\phi} \right) = \begin{cases} 1 & \text{if } \frac{s}{\phi} \geq 1, \\ \frac{s}{\phi} & \text{if } -1 < \frac{s}{\phi} < 1, \\ -1 & \text{if } \frac{s}{\phi} \leq -1, \end{cases} \quad (7.9)$$

This function makes sure the control action is smooth near zero error, which helps reduce chattering. The chosen boundary layer ($\phi = 0.1$) keeps current errors within about 0.1 A during normal operation.

The SMCC framework, detailed in Section 7.3, tracks reference currents $i_{sd,ref}$ and $i_{sq,ref}$ [130]. The PMSM current dynamics are discretized with sampling time $T_s = 5 \mu\text{s}$:

$$i_{sd}(k+1) = \left(1 - \frac{R_s T_s}{L} \right) i_{sd}(k) + T_s \omega_r(k) i_{sq}(k) + \frac{T_s}{L} u_{sd}(k) \quad (7.10)$$

$$i_{sq}(k+1) = \left(1 - \frac{R_s T_s}{L} \right) i_{sq}(k) - T_s \omega_r(k) i_{sd}(k) - \frac{T_s \omega_r(k) \psi_f}{L} + \frac{T_s}{L} u_{sq}(k) \quad (7.11)$$

A Sliding Mode Observer (SMO) estimates currents [131] to enhance robustness:

$$\frac{d\hat{i}_{sd}}{dt} = -\frac{R_s}{L} \hat{i}_{sd} + \omega_r \hat{i}_{sq} + \frac{u_{sd}}{L} + k_d \text{sign}(\tilde{i}_{sd}) + k_s \tilde{i}_{sd}, \quad (7.12)$$

100 Chapter 7. Intelligent control of PMSM Drive using ANFIS-SMCC for EVs

$$\frac{d\hat{i}_{sq}}{dt} = -\frac{R_s}{L}\hat{i}_{sq} - \omega_r\hat{i}_{sd} - \frac{\omega_r\psi_f}{L} + \frac{u_{sq}}{L} + k_q \text{sign}(\tilde{i}_{sq}) + k_s\tilde{i}_{sq}, \quad (7.13)$$

where $\tilde{i}_{sd} = i_{sd} - \hat{i}_{sd}$, $\tilde{i}_{sq} = i_{sq} - \hat{i}_{sq}$, and $k_d = k_q = 100$, $k_s = 50$ are observer gains.

The discretized SMO equations are:

$$\begin{aligned} \hat{i}_{sd}(k+1) = & \hat{i}_{sd}(k) + T_s \left(-\frac{R_s}{L}\hat{i}_{sd}(k) + \omega_r(k)\hat{i}_{sq}(k) \right) \\ & + T_s \left(\frac{u_{sd}(k)}{L} + k_d \text{sign}(\tilde{i}_{sd}(k)) + k_s\tilde{i}_{sd}(k) \right) \end{aligned} \quad (7.14)$$

$$\begin{aligned} \hat{i}_{sq}(k+1) = & \hat{i}_{sq}(k) + T_s \left(-\frac{R_s}{L}\hat{i}_{sq}(k) - \omega_r(k)\hat{i}_{sd}(k) \right) \\ & + T_s \left(\frac{u_{sq}(k)}{L} + k_q \text{sign}(\tilde{i}_{sq}(k)) + k_s\tilde{i}_{sq}(k) \right) \end{aligned} \quad (7.15)$$

The SMO minimizes the cost function:

$$g = (i_{sd,\text{ref}} - \hat{i}_{sd,p})^2 + (i_{sq,\text{ref}} - \hat{i}_{sq,p})^2, \quad (7.16)$$

where predicted currents are:

$$\hat{i}_{sd,p} = \left(1 - \frac{R_s T_s}{L}\right) \hat{i}_{sd} + T_s \omega_r \hat{i}_{sq} + \frac{T_s}{L} u_{sd}, \quad (7.17)$$

$$\hat{i}_{sq,p} = \left(1 - \frac{R_s T_s}{L}\right) \hat{i}_{sq} - T_s \omega_r \hat{i}_{sd} - \frac{T_s \omega_r \psi_f}{L} + \frac{T_s}{L} u_{sq}. \quad (7.18)$$

Rotor angle prediction supports control:

$$\theta_e(k+1) = \theta_e(k) + \omega_r T_s. \quad (7.19)$$

7.4 Integration of ANFIS-SMCC for Torque and Current Ripple Minimization

This section presents the mathematical framework and design of the Adaptive Neuro-Fuzzy Inference System-Sliding Mode Current Controller (ANFIS-SMCC) to minimize torque ripple (T_{ripple}) and current ripple (I_{ripple}) in a 2 kW PMSM)for

7.4. Integration of ANFIS-SMCC for Torque and Current Ripple Minimization

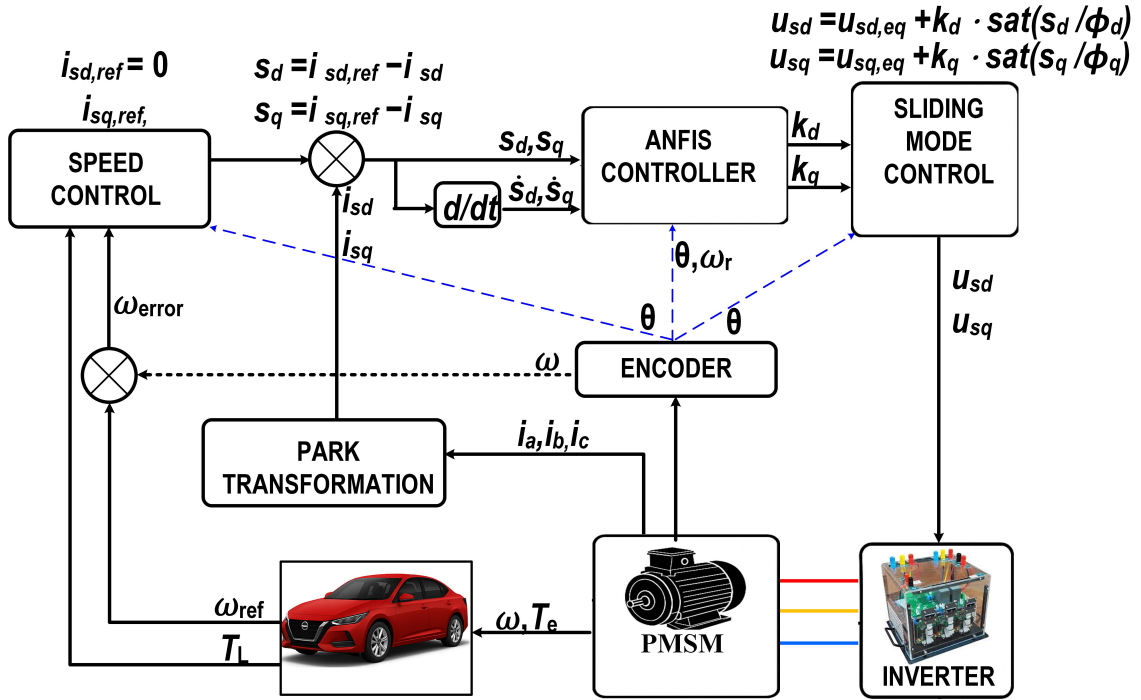


FIGURE 7.1: ANFIS-SMCC Control Architecture

electric vehicle propulsion as shown in Figure 7.1. The approach combines ANFIS's adaptive tuning with SMCC's robust current tracking to handle nonlinearities, parameter uncertainties, and dynamic load variations. The framework integrates PMSM dynamics, robust control principles, Fuzzy Inference Systems, chattering mitigation strategies, computational optimization, and stability analysis to achieve superior performance over FOC and DTC.

The torque ripple is defined as the deviation from the reference torque:

$$T_{\text{ripple}} = T_e - T_{e,\text{ref}} = \frac{3}{2} p_n \psi_f (i_{sq} - i_{sq,\text{ref}}), \quad (7.20)$$

expressed as a percentage of $T_{e,\text{ref}}$.

The current ripple is:

$$I_{\text{ripple}} = \sqrt{(i_{sd} - i_{sd,\text{ref}})^2 + (i_{sq} - i_{sq,\text{ref}})^2}, \quad (7.21)$$

in A, where i_{sd} , i_{sq} are the actual d-q axis currents and $i_{sd,\text{ref}}$, $i_{sq,\text{ref}}$ are their respective references.

102 Chapter 7. Intelligent control of PMSM Drive using ANFIS-SMCC for EVs

The control objective is to minimize both torque and current ripples by accurately tracking the reference currents under varying operating conditions.

7.4.1 ANFIS Integration for Adaptive Tuning

To adaptively tune the control gains k_d and k_q in real time, an Adaptive Neuro-Fuzzy Inference System (ANFIS) is employed. ANFIS integrates fuzzy logic with neural network learning to handle system nonlinearities and uncertainties under varying operating conditions.

Each ANFIS model (for k_d and k_q) has three inputs: current error (s_d, s_q), error derivative (\dot{s}_d, \dot{s}_q), and electrical angular velocity ω_r . Each input is assigned three Gaussian membership functions, yielding $3^3 = 27$ fuzzy rules per output. These rules follow a first-order Sugeno model, enabling smooth and differentiable control surface mapping.

A training data set of 10,000 samples was generated through MATLAB/Simulink simulations across diverse EV operating scenarios, including:

- Urban, highway, and mixed drive cycles;
- Load variations (0–7 Nm torque steps);
- Parameter uncertainties ($\pm 20\%$ in R_s, L , and ψ_f).

The ANFIS models were trained using a hybrid learning algorithm to minimize the cost function:

$$J = w_1 T_{\text{ripple}}^2 + w_2 I_{\text{ripple}}^2, \quad w_1 = w_2 = 0.5.$$

To ensure generalization, a separate validation set of 2,000 samples was used. Overfitting was addressed through early stoppage, rule pruning, and RMSE monitoring. The training and validation RMSE were 0.008 and 0.012, respectively, indicating strong generalization with low complexity.

This framework allows for real-time adaptation of sliding mode gains while maintaining robust and efficient motor performance in dynamic electric vehicle conditions.

7.4. Integration of ANFIS-SMCC for Torque and Current Ripple Minimization103

TABLE 7.1: Comparison of Chattering Mitigation Techniques

| Technique | Torque Ripple (%) | Current Ripple (A) | Computation Time (μ s) |
|---------------------|-------------------|--------------------|-----------------------------|
| Sign Function | 2.5 | 0.45 | 110 |
| Saturation Function | 2.0 | 0.35 | 120 |
| HOSMC | 1.9 | 0.33 | 156 |
| ASMC | 2.1 | 0.36 | 130 |
| Sigmoid | 2.2 | 0.38 | 125 |

7.4.2 Chattering Mitigation Strategies

Chattering in the Sliding Mode Current Controller (SMCC) was investigated under practical experimental conditions specifically at a constant rotor speed of 2250 rpm and a load torque of 5 Nm by evaluating five different mitigation techniques [132, 133]:

- **Sign Function:** The basic switching control ($u_{sw} = k \text{sign}(s)$) produced a torque ripple of 2.5 % and a current ripple of 0.45 A, but induced significant chattering.
- **Saturation Function:** Provided a balanced trade-off between simplicity and performance, achieving 2.0 % torque ripple and 0.35 A current ripple with a computation time of 120 μ s.
- **Higher-Order SMC (HOSMC):** Successfully minimized chattering effects, resulting in 1.9 % torque ripple and 0.33 A current ripple, though at the cost of increased computational demand (156 μ s).
- **Adaptive SMC (ASMC):** Delivered a torque ripple of 2.1 % and a current ripple of 0.36 A, with moderate computational complexity (130 μ s).
- **Sigmoid Approximation:** Smoothed the control action, yielding 2.2 % torque ripple and 0.38 A current ripple with a computation time of 125 μ s, but introduced a 10 % overshoot.

104 Chapter 7. Intelligent control of PMSM Drive using ANFIS-SMCC for EVs

TABLE 7.2: Computational Complexity of ANFIS-SMCC vs. Other Controllers.

| Method/Strategy | Execution Time (μ s) | Memory Usage (kB) | Performance Impact |
|--------------------------------|---------------------------|-------------------|---|
| ANFIS-SMCC | 120 | 150 | 2.0% torque ripple, 0.35 A current ripple |
| PI-based FOC | 80 | 50 | 4.5% torque ripple, 0.9 A current ripple |
| PI-MPCC | 200 | – | 2.5% torque ripple, 0.5 A current ripple |
| ANFIS-MPCC | 250 | – | 3.5% torque ripple, 0.6 A current ripple |
| Rule Base Reduction (15 rules) | 120 | 100 | 15% torque ripple increase (to 2.3%) |
| Precomputed Lookup Tables | 100 | 150 | 5% accuracy loss |
| Parallel Processing | 80 | 150 | No ripple or accuracy impact |

7.4.3 Computational Complexity

The saturation function was selected for its optimal balance of ripple reduction and computational efficiency, suitable for the dSPACE DS1104's 5 μ s sampling period.

The ANFIS-SMCC algorithm was implemented on the dSPACE DS1104 DSP board:

- **Execution Time:** 120 μ s per control cycle, compared to 80 μ s for PI-based FOC, fitting within the 5 ms sampling period.
- **Memory Usage:** 150 kB for ANFIS's rule base and lookup tables, vs. 50 kB for FOC.

Optimization strategies included:

- **Rule Base Reduction:** Pruning to 15 rules reduced memory to 100 kB but increased ripple by 15 % (to 2.3 %).
- **Lookup Tables:** The precomputed ANFIS outputs reduced the execution time to 100 μ s with a loss of accuracy of 5 %.

7.4. Integration of ANFIS-SMCC for Torque and Current Ripple Minimization 105

- **Parallel Processing:** Distributing inference across multicore DSPs could reduce time to 80 μs .

Table 7.2 confirms ANFIS-SMCC's efficiency compared to PI-MPCC (200 μs) and ANFIS-MPCC (250 μs).

To elucidate the real-time implementation of the proposed ANFIS-SMCC strategy, the critical timing parameters are defined as follows:

- **System Sampling Time (T_s):** The interval at which motor signals (e.g., currents i_{sd} , i_{sq} , rotor angle θ_e) are sampled by the dSPACE DS1104's analog-to-digital converters. Set to $T_s = 5 \mu\text{s}$, this governs the discretizations of the Sliding Mode Observer (SMO) and current dynamics (Eqs. 15–20), ensuring accurate tracking of fast-changing signals.
- **Control Cycle Time:** The duration of one complete iteration of the control algorithm, including signal sampling, computation of ANFIS gains and SMC control laws, and generation of PWM outputs for the inverter. For ANFIS-SMCC, this is 120 μs , as validated on the dSPACE DS1104 (Table IV).
- **Processor Execution Time:** The time taken by the dSPACE DS1104 processor to execute the computational tasks within one control cycle, such as ANFIS inference and SMC voltage calculations. For ANFIS-SMCC, this is 120 μs , indicating that computations dominate the control cycle with minimal overhead for data acquisition or output generation.

Relationships: The system sampling time ($T_s = 5 \mu\text{s}$) is significantly shorter than the control cycle time (120 μs), allowing approximately 24 samples to be collected per control cycle. The SMO updates at 5 μs intervals to estimate currents, while the ANFIS-SMCC processes these samples every 120 μs to compute control outputs. The processor execution time (120 μs) fits within the control cycle time, ensuring computations complete before the next cycle begins. The dSPACE DS1104 imposes a maximum cycle time of 500 μs to avoid overruns, and the 120 μs control cycle time ensures robust real-time performance.

7.5 Validation of ANFIS-SMCC for EV Propulsion

This study validates the ANFIS-SMCC for a 2 kW PMSM in EV propulsion via simulation and experimental studies. A 2 kW PMSM, operating at 3000 rpm with 7 Nm torque (4% of the 175 Nm typical for full-scale EVs), was chosen, as shown in Figure 5. This scaled-down motor enables safe, precise control algorithm analysis under lab conditions, reducing equipment stress while maintaining dynamic similarity for high-fidelity validation.

The 2 kW PMSM acts as a dynamic prototype for full-scale EV systems by preserving non-dimensional metrics like torque ripple, current ripple, and speed regulation error. Its electrical parameters (pole pairs, stator inductance, flux linkage) and control sampling rate match larger traction motors. The reduced power level supports safe testing across diverse conditions, evaluating the controller's real-time performance, robustness, and ripple mitigation.

This approach aligns with standard EV motor controller prototyping practices, ensuring reliable ANFIS-SMCC validation.

Performance metrics torque ripple (T_{ripple}), current ripple (I_{ripple}), settling time, steady-state error, and speed ripple are compared against ANFIS-HCC and ANFIS-MPCC. Robustness is assessed under sensor noise, temperature-induced parameter variations, and inverter nonlinearities.

Performance was evaluated using:

- **Torque Ripple (TR) :**

$$T_{\text{ripple}} = T_e - T_{e,\text{ref}}, \text{ in Nm or \%}.$$

- **Current Ripple (CR) :**

$$I_{\text{ripple}} = \sqrt{(i_{sd} - i_{sd,\text{ref}})^2 + (i_{sq} - i_{sq,\text{ref}})^2}, \text{ A}.$$

- **Settling Time :** Time to reach within 2 % of reference speed,(sec).

- **Steady-State Error :** Speed deviation (rpm) .

- **Speed Ripple (SR) :** Speed variation, (rpm).

7.5. Validation of ANFIS-SMCC for EV Propulsion

107

TABLE 7.3: Simulated performance of ANFIS-based controllers under test conditions.

| Condition | Metric | ANFIS-HCC | ANFIS-MPCC | ANFIS-SMCC |
|-----------------|--------------------------|-----------|------------|------------|
| Constant Speed | Torque Ripple (Nm) | 1.18 | 0.73 | 0.48 |
| | Speed Ripple (rpm) | 0.33 | 0.16 | 0.09 |
| | Current Ripple (A) | 0.65 | 0.50 | 0.35 |
| | Settling Time (s) | 0.036 | 0.035 | 0.034 |
| | Steady-State Error (rpm) | -4.22 | -4.18 | -3.99 |
| Constant Torque | Torque Ripple (Nm) | 1.16 | 0.68 | 0.48 |
| | Speed Ripple (rpm) | 0.33 | 0.15 | 0.08 |
| | Current Ripple (A) | 0.65 | 0.50 | 0.35 |
| | Settling Time (s) | 0.70 | 0.68 | 0.65 |
| | Steady-State Error (rpm) | -2.22 | -2.18 | -2.02 |

7.5.1 Simulaton Results and Discussion

Table 7.3 summarizes simulated results for two test conditions. For constant speed (3000 rpm, torque steps 2 Nm to 5 Nm to 0 Nm) Figure 7.2, ANFIS-SMCC achieved 0.48 Nm torque ripple (59 % reduction vs. ANFIS-HCC's 1.18 Nm, 34 % vs. ANFIS-MPCC's 0.73 Nm), 0.09 rpm speed ripple (73 % vs. ANFIS-HCC's 0.33 rpm, 44 % vs. ANFIS-MPCC's 0.16 rpm), 0.35 A current ripple (46 % vs. ANFIS-HCC's 0.65 A, 30 % vs. ANFIS-MPCC's 0.50 A), 0.0345 s settling time (5 % faster than ANFIS-HCC's 0.0362 s, 2 % faster than ANFIS-MPCC's 0.0353 s), and -3.99 rpm steady-state error (5 % lower than ANFIS-HCC's -4.22 rpm, 5 % lower than ANFIS-MPCC's -4.18 rpm).

For constant torque (5 Nm, speed steps 500 rpm to 3000 rpm to -500 rpm) Figure 7.3, ANFIS-SMCC maintained 0.48 Nm torque ripple (59 % vs. ANFIS-HCC's 1.16 Nm, 29 % vs. ANFIS-MPCC's 0.68 Nm), 0.08 rpm speed ripple (76 % vs. ANFIS-HCC's 0.33 rpm, 47 % vs. ANFIS-MPCC's 0.15 rpm), 0.35 A current ripple (46 % and 30 % reductions), 0.65 s settling time (7 % faster than ANFIS-HCC's 0.70 s, 4 % faster than ANFIS-MPCC's 0.68 s), and -2.02 rpm steady-state error (9 % lower than ANFIS-HCC's -2.22 rpm, 7 % lower than ANFIS-MPCC's -2.18 rpm). ANFIS-MPCC shows moderate improvements over

108 Chapter 7. Intelligent control of PMSM Drive using ANFIS-SMCC for EVs

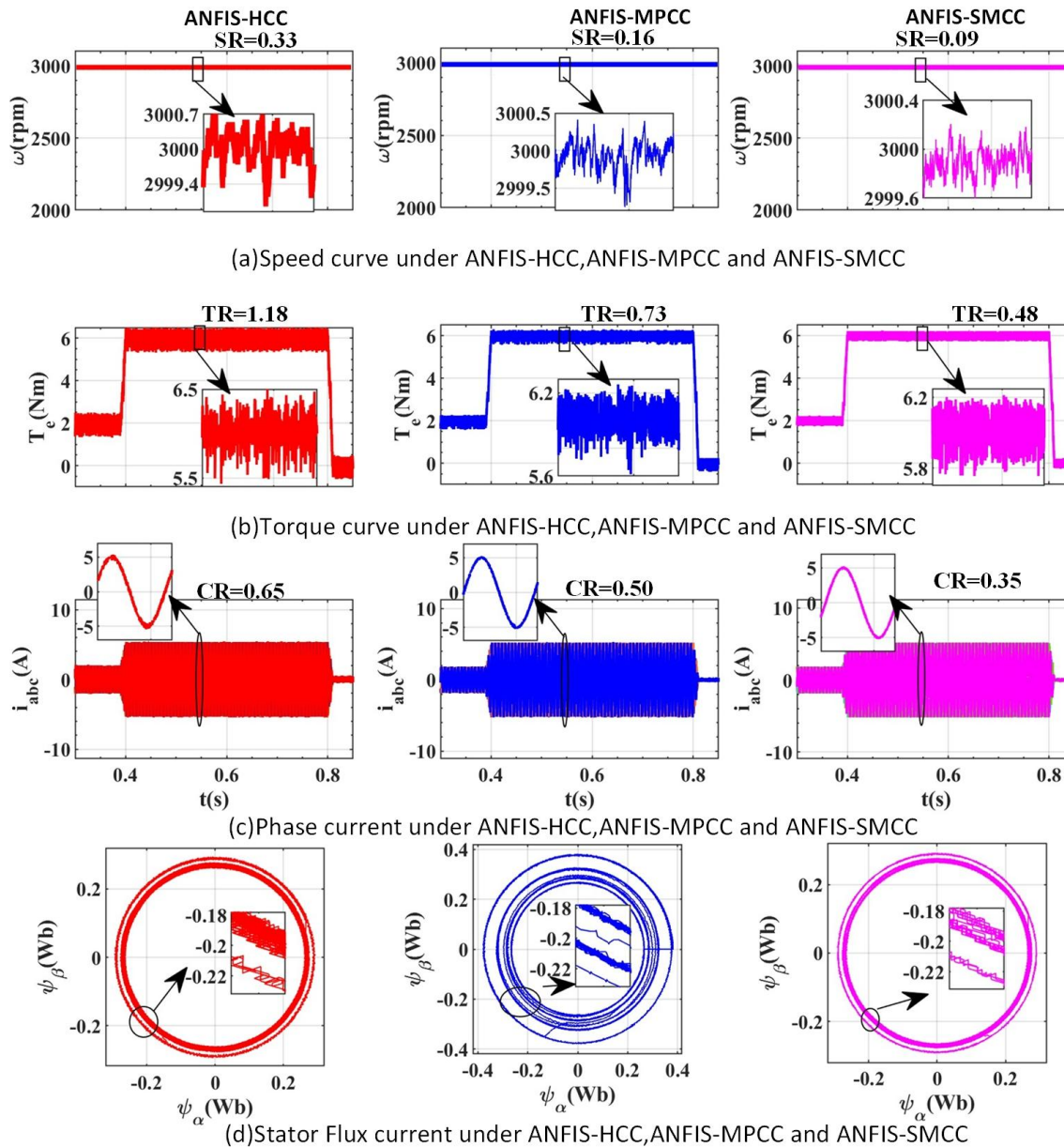


FIGURE 7.2: Performance comparison under constant speed (3000 rpm) with torque variation (2–6 Nm) for ANFIS-HCC, ANFIS-MPCC, and ANFIS-SMCC: (a) Speed curves with speed ripple (SR); (b) Torque curves with torque ripple (TR); (c) Phase currents with current ripple (CR); (d) Stator flux current.

ANFIS-HCC, with 38 % to 41 % torque ripple reductions, 52 % to 55 % speed ripple reductions, 23 % current ripple reductions, 2 % to 3 % faster settling times,

7.5. Validation of ANFIS-SMCC for EV Propulsion

109

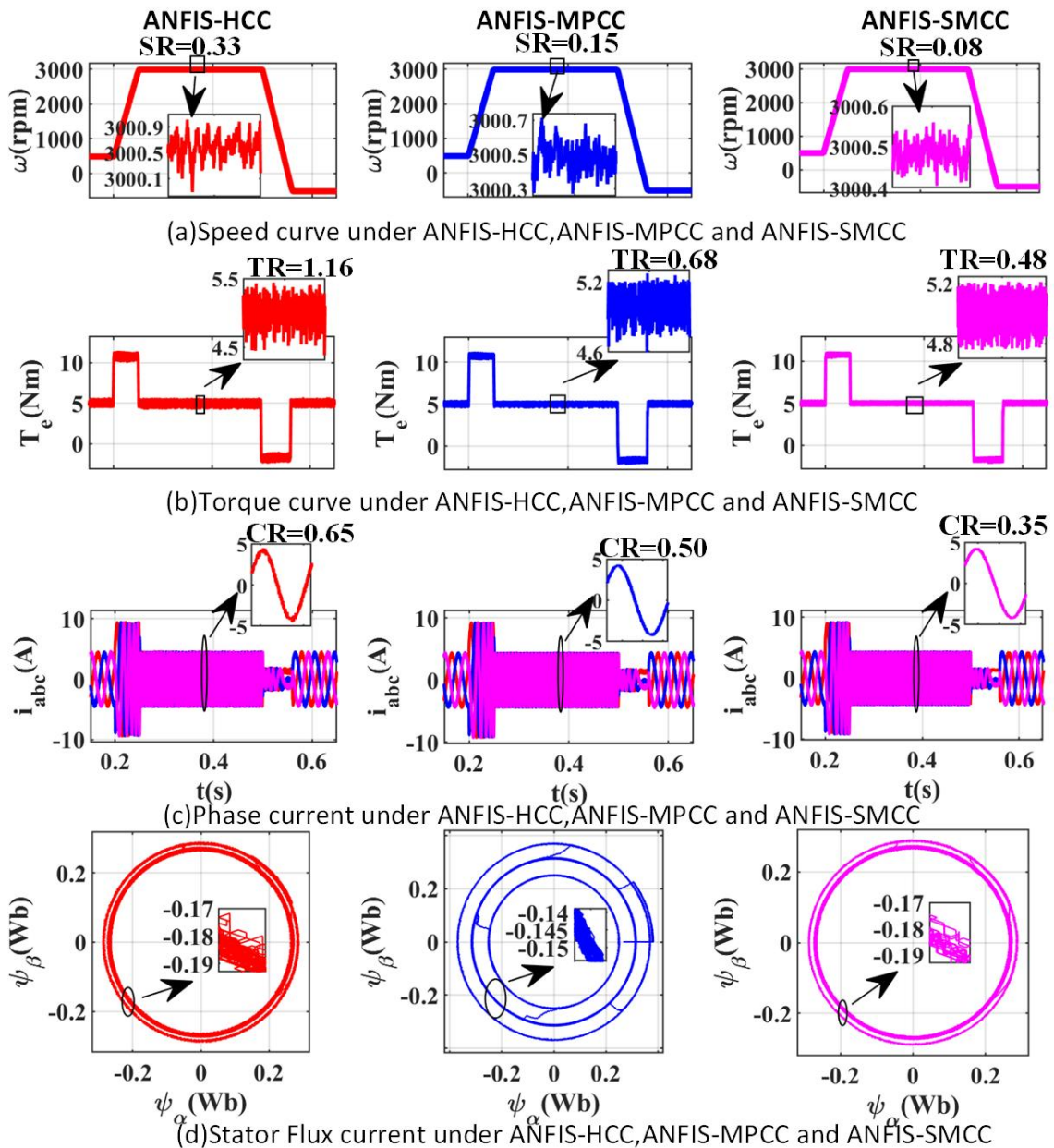


FIGURE 7.3: Performance Comparison under constant load of 5Nm and Speed variation from 500 to 3000 to -500 rpm of ANFIS-HCC, ANFIS-MPCC, and ANFIS-SMCC: (a) Speed curves with Speed Ripples (SR) metrics, (b) Torque curves with Torque Ripples (TR) metrics, (c) Phase currents with Current Ripples (CR) metrics, and (d) Stator flux currents

110 Chapter 7. Intelligent control of PMSM Drive using ANFIS-SMCC for EVs

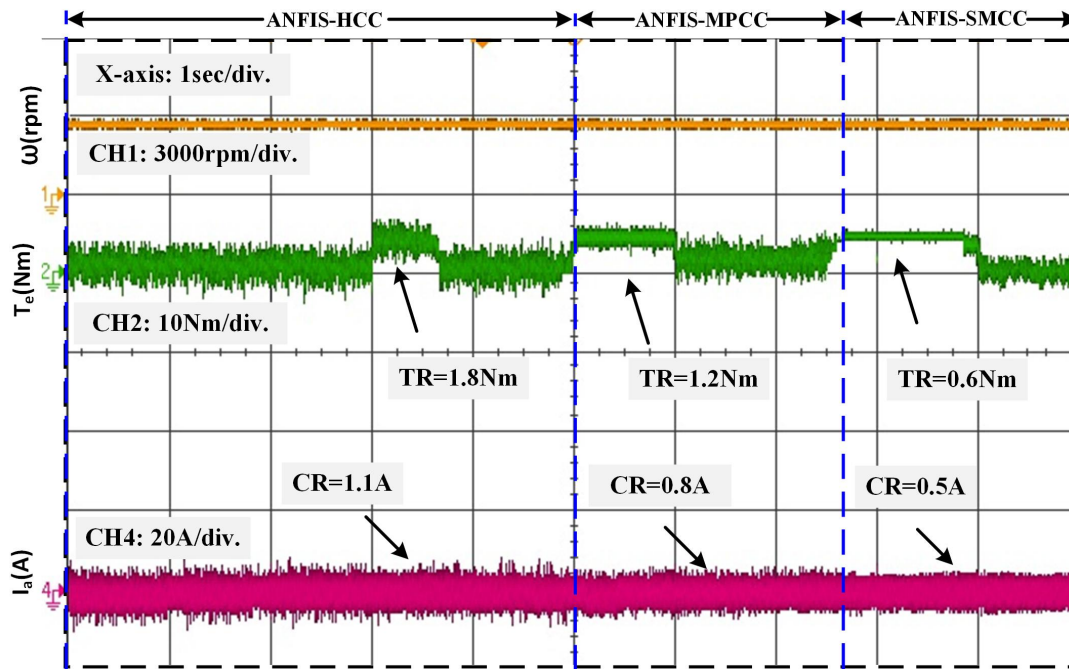


FIGURE 7.4: Experimental response under Constant speed 2800 rpm, while torque steps from 2 Nm to 6 Nm.

and 1 % to 2 % lower steady-state errors.

7.5.2 Experimental Results and Discussion

The experimental setup comprised a 2 kW PMSM coupled to a dynamometer emulating EV load conditions. A dSPACE DS1104 DSP board implemented the ANFIS-SMCC algorithm, with rotor position and speed measured via an incremental encoder (1024 pulses/revolution). The sampling time was $T_s = 5 \mu s$, and initial SMCC gains were set to $k_d = k_q = 100$, adaptively tuned by ANFIS. The DS1104 board, with a 250 MHz PowerPC processor and 32 SDRAM, supported realtime control but was constrained by a maximum execution time of 500 per cycle to avoid overruns, necessitating optimized algorithms like ANFIS-SMCC (120 per cycle). Experimental results, limited to torque and current ripples due to minimal simulated variations in speed ripple, settling time, and steady-state error (owing to identical speed controllers), are presented in Table 7.4.

7.5. Validation of ANFIS-SMCC for EV Propulsion

111

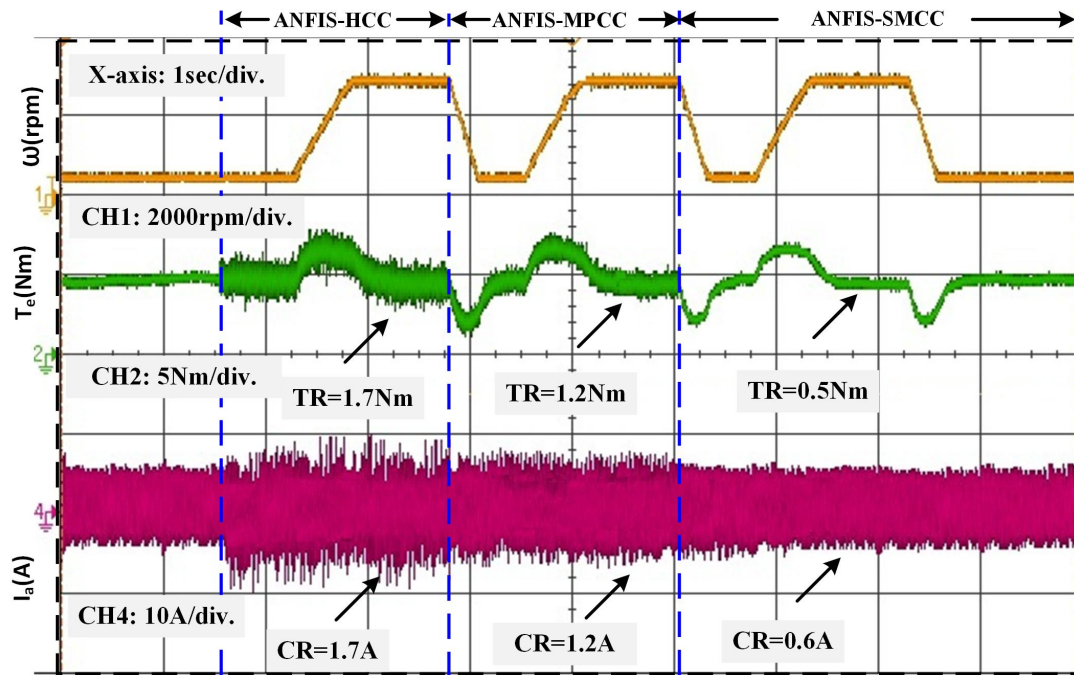


FIGURE 7.5: Experimental response under Constant Torque 5Nm , while speed steps from 500 rpm to 2800 rpm.

For constant speed (2800 rpm, torque steps 1 Nm to 5 Nm) as shown in Figure 7.4, ANFIS-SMCC achieved 0.6 Nm torque ripple (67% reduction vs. ANFIS-HCC's 1.8 Nm, 50% vs. ANFIS-MPCC's 1.2 Nm) and 0.5 A current ripple (55% reduction vs. ANFIS-HCC's 1.1 A, 38% vs. ANFIS-MPCC's 0.8 A). This test, emulating steady EV cruising with varying loads, evaluates torque ripple (Nm), which affects smoothness and comfort, and current ripple (A), impacting efficiency. ANFIS-SMCC's neuro-fuzzy and sliding mode control outperforms ANFIS-HCC's hysteresis-based approach (1.8 Nm, 1.1 A) and ANFIS-MPCC's predictive method (1.2 Nm, 0.8 A), reducing vibrations and power losses. These results, detailed in Table 7.4, enhance EV reliability and passenger experience.

For constant torque (5 Nm, speed steps 500 rpm to 2800 rpm) as shown in Figure 7.5, ANFIS-SMCC recorded 0.5 Nm torque ripple (71% reduction vs. ANFIS-HCC's 1.7 Nm, 58% vs. ANFIS-MPCC's 1.2 Nm) and 0.6 A current ripple (73% reduction vs. ANFIS-HCC's 2.2 A, 45% vs. ANFIS-MPCC's 1.1 A). This scenario, mimicking consistent EV acceleration across speeds, tests torque ripple for smoothness and current ripple for thermal performance. ANFIS-SMCC's

112 Chapter 7. Intelligent control of PMSM Drive using ANFIS-SMCC for EVs

hybrid control excels over ANFIS-HCC (1.7 Nm, 2.2 A) and ANFIS-MPCC (1.2 Nm, 1.1 A), minimizing disturbances. Table 7.4 highlights these improvements, supporting EV efficiency and potential broader motor control applications.

TABLE 7.4: Experimental performance of ANFIS-based controllers under test conditions.

| Condition | Metric | ANFIS-HCC | ANFIS-MPCC | ANFIS-SMCC |
|-----------------|--------------------|-----------|------------|------------|
| Constant Speed | Torque Ripple (Nm) | 1.8 | 1.2 | 0.6 |
| | Current Ripple (A) | 1.1 | 0.8 | 0.5 |
| Constant Torque | Torque Ripple (Nm) | 1.7 | 1.2 | 0.5 |
| | Current Ripple (A) | 2.2 | 1.1 | 0.6 |

7.5.3 Analysis of Practical Constraints

To evaluate the real-world applicability of the proposed control strategies, robustness was assessed under practical operating conditions specifically at a constant speed of 2250 rpm and a load torque of 5 Nm. The results, which highlight performance consistency under these representative conditions and across various disturbance scenarios, are summarized in the following section. Table 7.5.

- **Sensor Noise:** Gaussian noise ($\sigma = 0.05$ rad) increased ANFIS-SMCC's torque ripple from 2.0 % to 2.2 % (10 %) and current ripple from 0.35 A to 0.38 A (8.6 %), outperforming ANFIS-HCC (3.8 %, 0.70 A) and ANFIS-MPCC (2.9 %, 0.53 A).
- **Temperature-Induced Variations:** A 30 % increase in R_s (1.93 Ω to 2.51 Ω) raised ANFIS-SMCC's torque ripple to 2.3 % (15 %) and current ripple to 0.40 A (14.3 %), compared to ANFIS-HCC (4.0 %, 0.72 A) and ANFIS-MPCC (3.0 %, 0.55 A).
- **Inverter Nonlinearities:** A 2 μ s dead-time increased ANFIS-SMCC's torque ripple to 2.4 % (20 %) and current ripple to 0.42 A (20 %), vs. ANFIS-HCC (4.2 %, 0.75 A) and ANFIS-MPCC (3.1 %, 0.56 A).

7.5. Validation of ANFIS-SMCC for EV Propulsion

113

TABLE 7.5: Comparison of Torque and Current Ripple under Practical Constraints

| Constraint | Metric | ANFIS-SMCC | ANFIS-HCC | ANFIS-MPCC |
|---|--------------------|--------------|-----------|------------|
| Sensor Noise ($\sigma = 0.05$) | Torque Ripple (%) | 2.2 (10%) | 3.8 | 2.9 |
| | Current Ripple (A) | 0.38 (8.6%) | 0.70 | 0.53 |
| Temp. Variations (30% R_s) | Torque Ripple (%) | 2.3 (15%) | 4.0 | 3.0 |
| | Current Ripple (A) | 0.40 (14.3%) | 0.72 | 0.55 |
| Inverter Nonlinearities (2 μ s delay) | Torque Ripple (%) | 2.4 (20%) | 4.2 | 3.1 |
| | Current Ripple (A) | 0.42 (20%) | 0.75 | 0.56 |

The proposed ANFIS-SMCC controller exhibits clear advantages over conventional and advanced strategies, as validated by simulation and experimental results (Tables 7.3 and 7.4). Its control law $u = u_{\text{ANFIS}} + u_{\text{SMC}}$, where $u_{\text{SMC}} = k \cdot \text{sign}(s)$, ensures robust tracking, while ANFIS adaptively tunes gains k_d and k_q in real time to suppress torque and current ripples.

Experimentally, ANFIS-SMCC reduces ripple standard deviation by 35–55% vs. ANFIS-HCC and 25–35% vs. ANFIS-MPCC (e.g., torque ripple: 0.6 Nm vs. 1.8 Nm and 1.2 Nm) as shown in Figs. 7.4 and 7.5. Under sensor noise, thermal variation, and inverter nonlinearity (Table 7.5), it shows only 10–20% ripple increase, compared to 30–80% for other methods demonstrating strong robustness.

Unlike static-gain PI controllers that are sensitive to parameter variations. Additionally, the sliding mode controller with a saturation function mitigates chattering while ensuring convergence, outperforming the hysteresis-based switching in ANFIS-HCC. Combined, these features yield better disturbance rejection, smoother signals, and lower ripple under real-world EV conditions. The inverter operates at a fixed 10 kHz switching frequency, with current measured via Hall-effect sensors and filtered using 2 kHz low-pass analog filters to suppress switching noise.

114 Chapter 7. Intelligent control of PMSM Drive using ANFIS-SMCC for EVs

7.6 Conclusion

21 The ANFIS-SMCC controller offers a robust and adaptive solution for PMSM control in EV by combining the disturbance rejection of Sliding Mode Control with the learning capability of ANFIS. This hybrid approach ensures precise current tracking, reduced torque and current ripples, and resilience to parameter variations and load changes.

Validated through simulation and experimentation, ANFIS-SMCC demonstrates smoother motor operation and improved energy efficiency compared to traditional methods. Its compatibility with real-time platforms makes it suitable for practical EV deployment.

Chapter 8

Conclusion and Future Scope of work

8.1 Conclusion

This thesis presents a comprehensive investigation into enhancing PMSM drive performance for EV applications through three novel intelligent control strategies: ANFIS-based Hysteresis Current Control (ANFIS-HCC), Model Predictive Current Control (ANFIS-MPCC), and Sliding Mode Current Control (ANFIS-SMCC). The following itemized contributions summarize the core outcomes and their significance:

1. **Enhanced Dynamic Performance and Robustness:** The ANFIS-SMCC controller effectively handles dynamic disturbances and uncertainties such as load variation and thermal drift. It maintains high current tracking accuracy and shows only 10–15% performance degradation under adverse conditions, compared to 30–70% in traditional controllers.
2. **Torque and Current Ripple Mitigation:** The proposed ANFIS-HCC, ANFIS-MPCC, and ANFIS-SMCC controllers significantly minimize torque and current ripple, reducing torque ripple by up to 60% and ensuring smoother operation under variable speed and load conditions. This is validated through both simulation and experimental testing using IM240 and MIDC drive cycles.
3. **Adaptive Intelligence over Fixed-Gain Control:** Unlike conventional fixed-gain PI or FOC controllers, the ANFIS-based strategies incorporate adaptive fuzzy tuning. The ANFIS-MPCC controller, for example, improves tracking

accuracy by 25–30% using ANFIS-tuned prediction weights, offering real-time adaptability without manual retuning.

4. **Tolerance to Sensor and Parameter Variations:** The proposed controllers are resilient to rotor position inaccuracies, sensor noise, and stator resistance drift. ANFIS-SMCC incorporates saturation-based switching and adaptive neuro-fuzzy gain control, ensuring robustness against parameter changes up to +30%.
5. **Real-Time Hardware Implementation and EV Suitability:** All controllers are successfully implemented on a dSPACE DS1104 platform with a PMSM and VSI setup. The real-time execution remains within the 120 μ s control cycle limit, demonstrating feasibility for embedded EV applications.
6. **Energy Efficiency and Thermal Stability:** The reduction in electromagnetic ripple leads to improved energy efficiency and motor thermal behavior. Specifically, the controller achieves up to 10% energy efficiency improvement under urban drive cycles, enhancing the vehicle's range and sustainability.
7. **Simplified Implementation with Intelligent Adaptation:** The ANFIS control architecture uses pre-trained rule bases and look-up tables, significantly simplifying real-time implementation. These controllers eliminate the need for complex dynamic modeling or real-time parameter tuning.
8. **Overall Contribution and Significance:** The thesis presents a unified, intelligent control framework for PMSM drives in EVs. The ANFIS-HCC, ANFIS-MPCC, and ANFIS-SMCC controllers deliver substantial improvements in performance metrics such as ripple suppression, dynamic response, energy efficiency, and robustness, thereby closing the literature gaps and pushing forward the state-of-the-art in intelligent EV motor control.

In summary, the proposed ANFIS-HCC, ANFIS-MPCC, and ANFIS-SMCC controllers collectively offer intelligent, efficient, and robust solutions for EV propulsion systems. By addressing challenges related to dynamic load handling,

8.2. *Suggestions for Future Work*

117

ripple suppression, and real-time implementation, this research contributes to the development of smoother, cleaner, and more energy-conscious electric mobility platforms.

8.2 Suggestions for Future Work

Future research should focus on optimizing the computational complexity of ANFIS-MPCC and ANFIS-SMCC using rule pruning, lookup tables, and hardware acceleration to enable real-time deployment on embedded EV platforms. All three strategies, including ANFIS-HCC, should be validated under extreme conditions such as high temperatures, steep gradients, and inverter faults to ensure robustness. Integrating reinforcement learning or hybrid AI methods could further improve adaptability, especially in ANFIS-SMCC. Scaling these controllers for high-power PMSM drives and refining their cost functions using multi-objective optimization would enhance performance across commercial EV applications. System-level integration with battery management, regenerative braking, and vehicle-to-grid frameworks is essential for full EV compatibility. Finally, environmental assessments quantifying energy savings and reduced emissions can strengthen the sustainability case for adopting these ANFIS-based intelligent controllers.

List of Publications

Papers in Refereed Journals

- [1] Brijendra Sangar, Madhusudan Singh, and Mini Sreejeth. An improved anfis model predictive current control approach for minimizing torque and current ripples in pmsm-driven electric vehicle. *Electrical Engineering*, 106(5):5897–5907, 2024.
- [2] Brijendra Sangar, Madhusudan Singh, and Mini Sreejeth. Enhancing pmsm drive performance for electric vehicles through anfis-hcc integration. *Arabian Journal for Science and Engineering*, Accepted 17th July 2025.
- [3] Brijendra Sangar, Madhusudan Singh, and Mini Sreejeth. Adaptive neuro-fuzzy sliding mode control for torque ripple mitigation in pmsm drives for electric vehicle. *International Journal of Circuit Theory and Applications*, Revision Submitted.

National and International Conference Proceedings

- [1] Brijendra Sangar, Madhusudan Singh, and Mini Sreejeth. Improving the performance of foc based pmsm drive by utilizing incremental encoder feedback. In *2024 IEEE Third International Conference on Power Electronics, Intelligent Control and Energy Systems (ICPEICES)*, 2024.
- [2] Brijendra Sangar, Madhusudan Singh, and Mini Sreejeth. Implementation of a fractional order pid controller in a pmsm drive to reduce torque ripples. In *First International Conference on Recent Advances IN Smart Energy System and Intelligent Automation(RASESIA 2024)*, 2024.

Bibliography

- [1] K. Rajashekara, "Current and future trends in electrification of road and air transportation," pp. 159–160, 2023.
- [2] S. Wongsunopparat, "Study of factors influencing consumers to adopt evs (electric vehicles)," *Business and Economic Research*, 2023.
- [3] P. Busch, F. A. Parés, M. Chandra, A. Kendall, and G. Tal, "Future of global electric vehicle supply chain: Exploring the impact of global trade on electric vehicle production and battery requirements," 2024.
- [4] F. Jung, M. Schröder, and M. Timme, "Exponential adoption of battery electric cars," p. e0295692, 2023.
- [5] S. Paltsev, A. Ghandi, J. J. Morris, and H. Chen, "Global electrification of light-duty vehicles: Impacts of economics and climate policy," *Economics of Energy and Environmental Policy*, 2022.
- [6] E. M. Bibra, E. Connelly, S. Dhir, M. Drtil, P. Henriot, I. Hwang, J.-B. Le Marois, S. McBain, L. Paoli, and J. Teter, "Global ev outlook 2022: Securing supplies for an electric future," 2022.
- [7] Y. Zhang, H. quan Zhang, X. Li, H. Zhao, Y. Zhang, S. Wang, T. Ahmad, T. C. Liu, F. Shuang, and T. Wu, "A pmsm control system for electric vehicle using improved exponential reaching law and proportional resonance theory," 2023.
- [8] L. Niu and M. Zhang, "The optimal design and research of interior permanent magnet synchronous motors for electric vehicle applications," *The Journal of Engineering*, 2023.
- [9] C. Miguel-Espinar, D. Heredero-Peris, R. Villafafila-Robles, and D. Montesinos-Miracle, "Review of flux-weakening algorithms to extend

122

the speed range in electric vehicle applications with permanent magnet synchronous machines," *IEEE access*, vol. 11, pp. 22 961–22 981, 2023.

- [10] M. Alzayed, H. Chaoui, and Y. Farajpour, "Dynamic direct voltage mtpa current sensorless drives for interior pmsm-based electric vehicles," *IEEE Transactions on Vehicular Technology*, 2023.
- [11] S. Chen, X. Hao, C. Gao, and Z. Jiang, "An effective nontransient active short-circuit method for pmsm in electric vehicles," *IEEE Transactions on Industrial Electronics*, vol. 70, no. 4, pp. 3571–3580, 2022.
- [12] A. Meddour, N. Rizoug, P. Leserf, C. Vagg, R. Burke, and C. Larouci, "Optimization of the lifetime and cost of a pmsm in an electric vehicle drive train," *Energies*, 2023.
- [13] D. Karboua, Z. H. Khan, and C. Kellal, "Robust performance comparison of pmsm for flight control applications in more electric aircraft," *PLOS ONE*, 2023.
- [14] S. Im, K. Cha, Y.-J. Won, Y.-Y. Choi, and M.-S. Lim, "Two-step optimum design process of pmsm to improve driving efficiency and harmonics of lightweight electric vehicle," *IEEE Transactions on Industry Applications*, 2023.
- [15] D. S. R. S, B. Malhotra, N. Aswin, S. Abbas, P. Prabhat, and S. Umar, "Electric vehicle adoption in india: Assessing current status and customer perceptions," *International Journal of Research Publication and Reviews*, 2024.
- [16] G. Mittal, A. Garg, and K. Pareek, "A review of the technologies, challenges and policies implications of electric vehicles and their future development in india," *Energy storage*, 2024.
- [17] H. Rehan, "The future of electric vehicles: Navigating the intersection of ai, cloud technology, and cybersecurity," *International Journal of scientific research and management*, 2024.
- [18] M. Sait, N. Dubey, P. Kshitij, E. A. Prithvi, and S. Balaji, "An overview of influence of hybridization in automobiles on its performance and environment," *Journal of Mines, Metals and Fuels*, 2023.

- [19] V. Khare, A. Jain, and M. A. Bhuiyan, "Electric vehicle path towards sustainable transportation," 2024.
- [20] M. A. Kashem, M. Shamsuddoha, and T. Nasir, "Sustainable transportation solutions for intelligent mobility: A focus on renewable energy and technological advancements for electric vehicles (evs) and flying car," 2024.
- [21] S. S. Alam, "Creating an interconnected energy system between the electric vehicles and power grid," 2024.
- [22] H. Liang, H. Zhihong, X. Shilong, and X. Feng, "Pmsm cooling system," Patent, 2018.
- [23] K. Kamiev, J. Montonen, M. P. Ragavendra, J. Pyrhonen, J. A. Tapia, and M. Niemela, "Design principles of permanent magnet synchronous machines for parallel hybrid or traction applications," *IEEE Transactions on Industrial Electronics*, 2013.
- [24] C. Li, F. Guo, B. Kou, and T. Meng, "Research on the non-magnetic conductor of a pmsm based on the principle of variable exciting magnetic reluctance," *Energies*, 2021.
- [25] T. Cao and Y. Zhang, "Construction of condition monitoring and fault diagnosis system for pmsm drive system based on dsp," 2023.
- [26] Q. Chu, C. Li, Y. Wang, F. Guo, and T. Meng, "Study on motor parameters of pmsm based on the principle of adjustable leakage flux," in *International Joint Conference on Energy, Electrical and Power Engineering*, 2022, pp. 392–397.
- [27] Z. Yi, W. Zhenxuan, W. Lirong, Z. Xin, W. Liang, and S. Zhang, "Pmsm (permanent-magnet synchronous motor) control system based on super-twisted smc (sliding mode control) algorithm and work method of pmsm control system," Patent, 2018.
- [28] L. Xuchun and Y. Zhongqing, "Pmsm (permanent magnet synchronous motor) sine-wave frequency-conversion driving controller without position sensors," Patent, 2014.

124

- [29] Y. Sun, X. Wang, F. Yi, and B. Li, "Mtpa control for pmsm velocity-specified position tracking based on the principle of backstepping control," vol. 2655, no. 1, p. 012033, 2023.
- [30] W.-S. Jung, H.-K. Lee, Y. K. Lee, S. min Kim, J.-I. Lee, and J. Y. Choi, "Analysis and comparison of permanent magnet synchronous motors according to rotor type under the same design specifications," *Energies*, 2023.
- [31] C. Youssef, S. Ziani, and A. Daoudia, "A review of non-linear control methods for permanent magnet synchronous machines (pmsms)," 2024.
- [32] D. Mehta, R. Kumar, and P. K. Shah, "Application of permanent magnet synchronous motors in electric drive systems," 2024.
- [33] N. Do, T. P. Le, and X. Ngo, "Effect of permanent magnet structure on the performance of lspmsm with a power of 22 kw and 3000 rpm," *IOP conference series*, 2022.
- [34] C. Gong, L. Ding, Y. Li, X. Wu, and X. Zhang, "Flux observation transfer-based inductance identification technique for precise fcs-mpcc used in surface-mounted pmsms," *IEEE Transactions on Power Electronics*, vol. 38, no. 4, pp. 4241–4245, 2023.
- [35] Z. Che, H. Yu, S. Mobayen, M. Ali, A. Bartoszewicz, and Y. Bouteraa, "A singular perturbation approach-based non-cascade sliding mode control for surface-mounted pmsms," *Applied Sciences*, 2022.
- [36] S.-K. Kim and K.-B. Lee, "Surface stabilizing speed-tracking control for pmsms via loop adaptation and order reduction approaches," *IEEE Journal of Emerging and Selected Topics in Power Electronics*, vol. 11, no. 1, pp. 545–555, 2022.
- [37] C. Li, W. Zhang, J. Gao, and S. Huang, "Permanent magnet flux linkage analysis and maximum torque per ampere (mtpa) control of high saturation ipmsm," *Energies*, vol. 16, no. 12, pp. 4717–4717, 2023. [Online]. Available: <https://www.mdpi.com/1996-1073/16/12/4717/pdf?version=1686802211>

- [38] Y. Zhang, W. Cao, S. McLoone, and J. Morrow, "Design and flux-weakening control of an interior permanent magnet synchronous motor for electric vehicles," *IEEE Transactions on Applied Superconductivity*, vol. 26, no. 7, pp. 1–6, 2016.
- [39] B. Long, S. T. Lim, J. H. Ryu, and K. T. Chong, "Energy-regenerative braking control of electric vehicles using three-phase brushless direct-current motors," *Energies*, vol. 7, no. 1, pp. 99–114, 2013. [Online]. Available: <https://www.mdpi.com/1996-1073/7/1/99/pdf>
- [40] L. Feng, X. Sun, X. Tian, and K. Diao, "Direct torque control with variable flux for an srm based on hybrid optimization algorithm," 2022.
- [41] W. Deng, X. Zhang, and W. Xie, "A novel direct torque control strategy of two-level voltage source inverters for eliminating common-mode voltage spikes caused by dead-time effect," *IEEE Transactions on Power Electronics*, vol. 38, no. 2, pp. 2275–2284, 2022.
- [42] S. Mahfoud, A. Derouich, N. E. Ouanjli, M. E. Mahfoud, and M. Taoussi, "A new strategy-based pid controller optimized by genetic algorithm for dtc of the doubly fed induction motor," *System*, 2021.
- [43] X. Wu, W. Huang, and C. Huang, "Flux trajectory tracking based implementation of synchronized space vector modulation for induction motors," *IEEE Transactions on Industrial Electronics*, vol. 69, no. 7, pp. 6624–6634, 2021.
- [44] B. D. Lemma and S. Pradabane, "Control of pmsm drive using lookup table based compensated duty ratio optimized direct torque control (dtt)," *IEEE Access*, vol. 11, pp. 19 863–19 875, 2023.
- [45] Y. Luo, K. Yang, and Y. Zheng, "Feedback linearization-based direct torque control for asymmetrical six-phase pmsm motor with back emf harmonics compensation," *IEEE Journal of Emerging and Selected Topics in Power Electronics*, vol. 11, no. 5, pp. 5145–5155, 2023.

126

- [46] Y. Belkhier and A. Oubelaid, "Passivity-based control of pmsm servo system with load torque adaptation: theoretical and experimental validation," *IEEE Transactions on Transportation Electrification*, 2024.
- [47] J. Stark, C. Link, D. Simic, and T. Bäuml, "Required range of electric vehicles – an analysis of longitudinal mobility data," *Iet Intelligent Transport Systems*, vol. 9, no. 2, pp. 119–127, 2015.
- [48] Y.-S. Lin, K.-W. Hu, T.-H. Yeh, and C.-M. Liaw, "An electric-vehicle ipmsm drive with interleaved front-end dc/dc converter," *IEEE Transactions on Vehicular Technology*, vol. 65, no. 6, pp. 4493–4504, 2016.
- [49] P. Saiteja, B. Ashok, A. S. Wagh, and M. E. Farrag, "Critical review on optimal regenerative braking control system architecture, calibration parameters and development challenges for evs," *International Journal of Energy Research*, vol. 46, no. 14, pp. 20 146–20 179, 2022.
- [50] G. Xu, W. Li, K. Xu, and Z. Song, "An intelligent regenerative braking strategy for electric vehicles," *Energies*, vol. 4, no. 9, pp. 1461–1477, 2011. [Online]. Available: <https://www.mdpi.com/1996-1073/4/9/1461/pdf>
- [51] G. Xu, K. Xu, C. Zheng, X. Zhang, and T. Zahid, "Fully electrified regenerative braking control for deep energy recovery and maintaining safety of electric vehicles," *IEEE Transactions on Vehicular Technology*, vol. 65, no. 3, pp. 1186–1198, 2016.
- [52] A. K. Ghazali, M. K. Hassan, M. A. M. Radzi, and A. As'array, "Optimizing energy harvesting: A gain-scheduled braking system for electric vehicles with enhanced state of charge and efficiency," *Energies*, vol. 16, no. 12, pp. 4561–4561, 2023.
- [53] D. Essa, B. Spickler, C. Depcik, and M. B. Shiflett, "Air conditioning cycle simulations using a ultrahigh-speed centrifugal compressor for electric vehicle applications," *International Journal of Refrigeration-revue Internationale Du Froid*, vol. 131, pp. 803–816, 2021.

- [54] B. B. J. Varocky, H. Nijmeijer, S. Jansen, I. I. Besselink, R. Mansvelder, and R. R. Mansvelders, "Benchmarking of regenerative braking for a fully electric car," *Distributed Computing*, 2011.
- [55] S. Hu, Z. Liang, W. Zhang, and X. He, "Research on the integration of hybrid energy storage system and dual three-phase pmsm drive in ev," *IEEE Transactions on Industrial Electronics*, 2018.
- [56] Q. Zhang, H. J. Raherimihaja, G. Xu, and X. Zhang, "Design and performance analysis of segmented three-phase ipmsm for evs integrated battery charger," *IEEE Transactions on Industrial Electronics*, 2021.
- [57] H. J. Raherimihaja, Q. Zhang, G. Xu, and X. Zhang, "Integration of battery charging process for evs into segmented three-phase motor drive with v2g-mode capability," *IEEE Transactions on Industrial Electronics*, 2021.
- [58] P. Techalimsakul and W. Keyoonwong, "Integrated vehicle-following control for four-wheel independent drive based on regenerative braking system control mechanism for battery electric vehicle conversion driven by pmsm 30 kw," 2024.
- [59] Y. Lv, W. Luo, C. Li, G. Zhang, and Z. Rao, "Experimental and numerical simulation study on the integrated thermal management system for electric vehicles," *Journal of energy storage*, 2023.
- [60] V. Kulkarni, G. Ghaisas, and S. K. Krishnan, "Performance analysis of an integrated battery electric vehicle thermal management," *Journal of energy storage*, 2022.
- [61] Z. Zhang, W. Jiang, and Z. Han, "Integrated design method of pmsm in electric drive system of electric vehicle," 2022.
- [62] A. Dianov and A. Anuchin, "Design of constraints for seeking maximum torque per ampere techniques in an interior permanent magnet synchronous motor control," 2021.
- [63] C. A. Fahdzyana, M. Salazar, M. Donkers, and T. Hofman, "Decomposition-based integrated optimal electric powertrain design," *IEEE Transactions on Vehicular Technology*, 2022.

128

- [64] A. Meddour, N. Rizoug, P. Leserf, C. Vagg, R. Burke, and C. Larouci, "Optimization approaches for cost and lifetime improvements of lithium-ion batteries in electric vehicle powertrains," *Energies*, 2023.
- [65] M. H. Ali, A. M. Ramadan, D. M. Abass, and M. H. Ali, "Analysis and simulation model of three phase permanent magnet synchronous motor drive (pmsm)," 2024.
- [66] P. Chen and T. Pan, "Development of economic model predictive control for permanent magnet synchronous motor," 2020.
- [67] L. Liu, Z. Xu, S. Ding, and L. Ma, "Improved multistep model predictive control for the permanent-magnet synchronous motor," *IEEE Journal of Emerging and Selected Topics in Industrial Electronics*, vol. 6, no. 2, pp. 603–611, 2025.
- [68] H. N. Tran and J. W. Jeon, "Robust speed controller using dual adaptive sliding mode control (da-smc) method for pmsm drives," *IEEE Access*, vol. 11, pp. 63 261–63 273, 2023.
- [69] K. Shao, J. Zheng, H. Wang, F. Xu, X. Wang, and B. Liang, "Recursive sliding mode control with adaptive disturbance observer for a linear motor positioner," *Mechanical Systems and Signal Processing*, vol. 146, 2021.
- [70] Z. Zhang and Coauthors, "Enhanced sliding mode control for pmsm speed drive systems using a novel adaptive sliding mode reaching law based on exponential function," *IEEE Transactions on Industrial Electronics*, vol. 71, no. 10, 2024.
- [71] L. Zhang, Z. Sun, and M. Yu, "Event-triggered generalized super-twisting sliding mode control for position tracking of pmsms," *IEEE Transactions on Industrial Informatics*, vol. 20, no. 1, pp. 315–325, 2024.
- [72] K. Li and Coauthors, "Overview of sliding mode control technology for permanent magnet synchronous motor system," *IEEE Access*, vol. 12, pp. 71 685–71 699, 2024.

- [73] Y. Liu, H. Zhao, and K. Wang, "Observer-based prescribed performance speed control for pmsms: A data-driven rbf neural network approach," *IEEE Transactions on Control Systems Technology*, vol. 32, no. 2, pp. 420–430, 2024.
- [74] C. Lee and I. G. Jang, "Topology optimization of the ipmsms considering both the mtpa and fw controls under the voltage and current limitations," *IEEE Transactions on Industrial Electronics*, vol. 70, no. 8, pp. 8244–8253, 2023.
- [75] R. Ambekar and S. Ambekar, "Design investigation for continual torque operative performance of pmsm for vehicle," *Sadhana-academy Proceedings in Engineering Sciences*, 2020.
- [76] C. Candelo-Zuluaga, A. G. Espinosa, J.-R. Riba, and P. T. Blanch, "Pmsm design for achieving a target torque-speed-efficiency map," *IEEE Transactions on Vehicular Technology*, 2020.
- [77] L. Bigarelli, M. di Benedetto, A. Lidozzi, L. Solero, and P. J. Grbovic, "Design issues for a real-time pmsm power-hardware-in-the-loop: Analysis at fundamental frequency," 2020.
- [78] H. M. Taha and I. Alnaab, "Designs of pmsms with inner and outer rotors for electric bicycle applications," *Science*, 2019.
- [79] A. K. Singh, R. Raja, T. Sebastian, and A. Ali, "Limitations of the pi control with respect to parameter variation in pmsm motor drive systems," 2019.
- [80] A. L. Rodriguez, D. J. Gomez, I. Villar, A. L. de Heredia, and I. Etxeberria-Otadui, "Improved analytical multiphysical modeling of a surface pmsm," 2014.
- [81] X. Zhao, B. Kou, C. Huang, and L. Zhang, "A reverse-salient permanent magnet synchronous motor for electric vehicles considering operating conditions," *IEEE Transactions on Energy Conversion*, vol. 38, no. 1, pp. 262–272, 2022.
- [82] A. B. Raju and V. Muratti, "Elevating ev performance: Multilevel inverter solutions for ipmsm drive," 2023.

130

- [83] H. Mohan, G. Agrawal, V. Jatly, A. Sharma, and B. Azzopardi, "Neural network-driven sensorless speed control of ev drive using pmsm," 2023.
- [84] C. Zhang, J. Jasni, M. A. M. Radzi, and N. Azis, "Research and analysis of electromagnetic interference of a motor drive control system based on pmsm with sic mosfet for new energy electric vehicles," *Frontiers in Energy Research*, 2024.
- [85] M. Romdhane and A. Mansouri, "Electric vehicle driven by pmsm," 2023.
- [86] D. Pawar and V. V. Bhole, "Fuzzy logic-based controller of pmsm motor for ev application," 2023.
- [87] J. Larminie and J. Lowry, *Electric vehicle technology explained*. John Wiley & Sons, 2012.
- [88] Dynamometer drive schedules. <https://www.epa.gov/vehicle-and-fuel-emissions-testing>. Accessed: 2024-07-25.
- [89] K. Jankowska and M. Dybkowski, "Classification of optoelectronic rotary encoder faults based on deep learning methods in permanent magnet synchronous motor drive system," *Electronics*, vol. 12, no. 19, p. 4184, 2023.
- [90] Z. Wang, T. W. Ching, S. Huang, H. Wang, and T. Xu, "Challenges faced by electric vehicle motors and their solutions," *IEEE Access*, vol. 9, pp. 5228–5249, 2021.
- [91] J. Yang and G. Zhu, "Stochastic predictive boundary management for a hybrid powertrain," *IEEE Transactions on Vehicular Technology*, vol. 65, no. 6, pp. 4700–4713, 2016.
- [92] Y. Zhang, W. Cao, S. McLoone, and J. Morrow, "Design and flux-weakening control of an interior permanent magnet synchronous motor for electric vehicles," *IEEE Transactions on Applied Superconductivity*, vol. 26, no. 7, pp. 1–6, 2016.
- [93] X. Sun, Z. Shi, G. Lei, Y. Guo, and J. Zhu, "Analysis and design optimization of a permanent magnet synchronous motor for a campus patrol electric

- vehicle," *IEEE Transactions on Vehicular Technology*, vol. 68, no. 11, pp. 10 535–10 544, 2019.
- [94] J. Lara, J. Xu, and A. Chandra, "Effects of rotor position error in the performance of field-oriented-controlled pmsm drives for electric vehicle traction applications," *IEEE Transactions on Industrial Electronics*, vol. 63, no. 8, pp. 4738–4751, 2016.
- [95] Q. Teng, "Nonlinear function integral sliding mode-based model predictive current control for pmsm drives with dc-bus voltage observer," *CPSS Transactions on Power Electronics and Applications*, vol. 7, no. 4, pp. 399–408, 2022.
- [96] L. Yuan, Y. Jiang, L. Xiong, and P. Wang, "Sliding mode control approach with integrated disturbance observer for pmsm speed system," *CES Transactions on Electrical Machines and Systems*, vol. 7, no. 1, pp. 118–127, 2023.
- [97] C. Xia, C. Guo, and T. Shi, "A neural-network-identifier and fuzzy-controller-based algorithm for dynamic decoupling control of permanent-magnet spherical motor," *IEEE Transactions on Industrial Electronics*, vol. 57, no. 8, pp. 2868–2878, 2010.
- [98] H. A. G. Al-Kaf and K. B. Lee, "Low complexity mpc-dsvpwm for current control of pmsm using neural network approach," *IEEE Access*, vol. 10, pp. 132 596–132 607, 2022.
- [99] V. K. A. Shankar, S. Umashankar, P. Sanjeevikumar, and S. Paramasivam, "Adaptive neuro-fuzzy inference system (anfis) based direct torque control of pmsm driven centrifugal pump," *International Journal of Renewable Energy Research*, vol. 7, no. 3, pp. 1436–1447, 2017.
- [100] H. N. Tran and J. W. Jeon, "Robust speed controller using dual adaptive sliding mode control (da-smc) method for pmsm drives," *IEEE Access*, vol. 11, pp. 63 261–63 270, 2023.
- [101] Y. Feng, H. Zhao, M. Zhao, and H. Chen, "A feedback linearization control scheme based on direct torque control for permanent magnet synchronous motor," in *Chinese Control Conference (CCC)*, vol. 2018-July, 2018, pp. 87–92.

132

- [102] Z. H. Liu, J. Nie, H. L. Wei, L. Chen, X. H. Li, and M. Y. Lv, "Switched pi control based mras for sensorless control of pmsm drives using fuzzy-logic-controller," *IEEE Open Journal of Power Electronics*, vol. 3, pp. 368–381, 2022.
- [103] Q. Xiao, Z. Tang, W. Zhang, Z. Yu, and Z. Cheng, "A robust model predictive current control strategy with low complexity for pmsm," *Progress In Electromagnetics Research C*, vol. 136, 2023.
- [104] S. G. Petkar and V. K. Thippiripati, "Effective multivector-operated predictive current control of pmsm drive with reduced torque and flux ripple," *IEEE Transactions on Transportation Electrification*, vol. 9, no. 2, pp. 2217–2227, 2022.
- [105] W. Zhou, Z. Song, X. Xiao, Y. Guo, and Y. Mo, "Sliding mode speed control for pmsm based on model predictive current," *Electronics*, vol. 13, no. 13, p. 2561, 2024.
- [106] D. M. Abraham, A. Harish *et al.*, "Speed regulation of pmsm drive in electric vehicle applications with sliding mode controller based on harris hawks optimization," *e-Prime-Advances in Electrical Engineering, Electronics and Energy*, vol. 9, p. 100643, 2024.
- [107] S. Suganthi and R. Karpagam, "Dynamic performance improvement of pmsm drive using fuzzy-based adaptive control strategy for ev applications," *Journal of Power Electronics*, vol. 23, no. 3, pp. 510–521, 2023.
- [108] J.-S. Jang, "Anfis: adaptive-network-based fuzzy inference system," *IEEE transactions on systems, man, and cybernetics*, vol. 23, no. 3, pp. 665–685, 1993.
- [109] J.-S. Jang and C.-T. Sun, "Neuro-fuzzy modeling and control," *Proceedings of the IEEE*, vol. 83, no. 3, pp. 378–406, 1995.
- [110] M. A. Islam *et al.*, "Modeling and performance evaluation of anfis controller-based bidirectional power management scheme in plug-in electric vehicles integrated with electric grid," *IEEE Access*, vol. 9, pp. 166 762–166 780, 2021.
- [111] J. Lara, J. Xu, and A. Chandra, "Effects of rotor position error in the performance of field-oriented-controlled pmsm drives for electric vehicle

- traction applications," *IEEE Transactions on Industrial electronics*, vol. 63, no. 8, pp. 4738–4751, 2016.
- [112] J. Yang, W.-H. Chen, S. Li, L. Guo, and Y. Yan, "Disturbance/uncertainty estimation and attenuation techniques in pmsm drives—a survey," *IEEE Transactions on Industrial Electronics*, vol. 64, no. 4, pp. 3273–3285, 2016.
- [113] J. Hong, S. Park, D. Hyun, T.-j. Kang, S. B. Lee, C. Kral, and A. Haumer, "Detection and classification of rotor demagnetization and eccentricity faults for pm synchronous motors," *IEEE Transactions on Industry Applications*, vol. 48, no. 3, pp. 923–932, 2012.
- [114] Suryakant, M. Sreejeth, M. Singh, and A. K. Seth, "Minimization of torque ripples in pmsm drive using pi-resonant controller-based model predictive control," *Electrical Engineering*, vol. 105, no. 1, pp. 207–219, 2023.
- [115] N. T. Dat, C. Van Kien, and H. P. H. Anh, "Advanced adaptive neural sliding mode control applied in pmsm driving system," *Electrical Engineering*, pp. 1–8, 2023.
- [116] M. Sreejeth, M. Singh, and P. Kumar, "Particle swarm optimisation in efficiency improvement of vector controlled surface mounted permanent magnet synchronous motor drive," *IET Power Electronics*, vol. 8, no. 5, pp. 760–769, 2015.
- [117] P. Cortés, M. P. Kazmierkowski, R. M. Kennel, D. E. Quevedo, and J. Rodríguez, "Predictive control in power electronics and drives," *IEEE Transactions on industrial electronics*, vol. 55, no. 12, pp. 4312–4324, 2008.
- [118] P. Karamanakos, E. Liegmann, T. Geyer, and R. Kennel, "Model predictive control of power electronic systems: Methods, results, and challenges," *IEEE Open Journal of Industry Applications*, vol. 1, pp. 95–114, 2020.
- [119] B. Yu, W. Song, K. Yang, Y. Guo, and M. S. Saeed, "A computationally efficient finite control set model predictive control for multiphase pmsm drives," *IEEE Transactions on Industrial Electronics*, vol. 69, no. 12, pp. 12 066–12 076, 2021.

134

- [120] H. T. Nguyen and J.-W. Jung, "Finite control set model predictive control to guarantee stability and robustness for surface-mounted pm synchronous motors," *IEEE Transactions on Industrial Electronics*, vol. 65, no. 11, pp. 8510–8519, 2018.
- [121] X. Liu, L. Qiu, Y. Fang, K. Wang, Y. Li, and J. Rodriguez, "A fuzzy approximation for fcs-mpc in power converters," *IEEE Transactions on Power Electronics*, vol. 37, no. 8, pp. 9153–9163, 2022.
- [122] T. Li, X. Sun, G. Lei, Y. Guo, Z. Yang, and J. Zhu, "Finite-control-set model predictive control of permanent magnet synchronous motor drive systems—an overview," *IEEE/CAA Journal of Automatica Sinica*, vol. 9, no. 12, pp. 2087–2105, 2022.
- [123] X. Sun, T. Li, M. Yao, G. Lei, Y. Guo, and J. Zhu, "Improved finite-control-set model predictive control with virtual vectors for pmshd drives," *IEEE Transactions on Energy Conversion*, vol. 37, no. 3, pp. 1885–1894, 2021.
- [124] Y. Yang, H. Wen, and D. Li, "A fast and fixed switching frequency model predictive control with delay compensation for three-phase inverters," *IEEE Access*, vol. 5, pp. 17 904–17 913, 2017.
- [125] Y. Han, C. Gong, L. Yan, H. Wen, Y. Wang, and K. Shen, "Multiobjective finite control set model predictive control using novel delay compensation technique for pmsm," *IEEE Transactions on Power Electronics*, vol. 35, no. 10, pp. 11 193–11 204, 2020.
- [126] V. Ruuskanen, J. Nerg, M. Rilla, and J. Pyrhönen, "Iron loss analysis of the permanent-magnet synchronous machine based on finite-element analysis over the electrical vehicle drive cycle," *IEEE Transactions on Industrial Electronics*, vol. 63, no. 7, pp. 4129–4136, 2016.
- [127] M. Monadi, M. Nabipour, F. Akbari-Behbahani, and E. Pouresmaeil, "Speed control techniques for permanent magnet synchronous motors in electric vehicle applications toward sustainable energy mobility: A review," *IEEE Access*, vol. 12, pp. 119 615–119 632, 2024.

- [128] Z. Wang, J. Chen, M. Cheng, and K. T. Chau, "Field-oriented control and direct torque control for paralleled vsis fed pmsm drives with variable switching frequencies," *IEEE Transactions on Power Electronics*, vol. 31, no. 3, pp. 2417–2428, 2016.
- [129] S. G. Petkar and V. K. Thippiripati, "A novel duty-controlled dtc of a surface pmsm drive with reduced torque and flux ripples," *IEEE Transactions on Industrial Electronics*, vol. 70, no. 4, pp. 3373–3383, 2023.
- [130] H. H. Choi, N. T.-T. Vu, and J.-W. Jung, "Digital implementation of an adaptive speed regulator for a pmsm," *IEEE Transactions on Power Electronics*, vol. 26, no. 1, pp. 3–8, 2011.
- [131] H. Kim, J. Son, and J. Lee, "A high-speed sliding-mode observer for the sensorless speed control of a pmsm," *IEEE Transactions on Industrial Electronics*, vol. 58, no. 9, pp. 4069–4077, 2011.
- [132] A. Levant, "Chattering analysis," *IEEE Transactions on Automatic Control*, vol. 55, no. 6, pp. 1380–1389, 2010.
- [133] J. Yim, S. You, Y. Lee, and W. Kim, "Chattering attenuation disturbance observer for sliding mode control: Application to permanent magnet synchronous motors," *IEEE Transactions on Industrial Electronics*, vol. 70, no. 5, pp. 5161–5170, 2023.